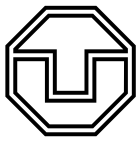

TECHNISCHE UNIVERSITÄT DRESDEN

INSTITUTE OF NUCLEAR AND PARTICLE PHYSICS

The Influence of Varying Pulse Shapes on the Energy Reconstruction of ATLAS Liquid Argon Calorimeter Signals using Convolutional Neural Networks

A thesis submitted for the degree
Master of Science

submitted by

Christian Gutsche
born June 23 1998 in Zittau

Institute for Nuclear and Particle Physics
Faculty of Physics
School of Science
Technische Universität Dresden
2022

Submitted October 6 2022

1. Gutachter: Prof. Dr. Arno Straessner
2. Gutachter: Dr. Frank Siegert

Abstract

From 2026 to 2028 the large particle accelerator LHC at CERN will get an upgrade. The number of simultaneous proton-proton-collisions will be increased to make rare processes or even new physics discoverable.

Increasing the amount of simultaneous collisions will be a big challenge for the signal processing and triggers. The so called Optimal Filter, which is currently used at the ATLAS Liquid Argon calorimeter for the energy reconstruction, will reach its limits. For a reliable energy reconstruction alternative algorithms are needed. A possible alternative is the usage of artificial neural networks.

In this thesis the energy reconstruction using convolutional neural networks is investigated. Especially approaches of resource-saving optimizations of previously developed networks are presented. It is being studied how time shifted pulses influence the energy reconstruction and how these negative influences can be reduced. Additionally, convolutional neural networks which reconstruct the hit times are presented.

Kurzfassung

Von 2026 bis 2028 soll der große Teilchenbeschleuniger LHC am CERN ein Upgrade erhalten. Die Zahl gleichzeitiger Proton-Proton-Kollisionen soll gesteigert werden, um seltene Prozesse oder sogar neue Physik entdeckbar zu machen.

Das Erhöhen der Anzahl simultaner Kollisionen, stellt eine große Herausforderung für die Signalverarbeitung und Trigger dar. Der sogenannte Optimal Filter, der momentan am Liquid Argon Kalorimeter des ATLAS Detektors zur Energierekonstruktion genutzt wird, wird nach dem LHC-Upgrade an seine Grenzen kommen. Für eine zuverlässige Energierekonstruktion sind alternative Algorithmen notwenig. Eine solche Alternative können künstliche Neuronale Netze darstellen. In dieser Arbeit wird die Energierekonstruktion unter Nutzung von sogennanten Convolutional Neural Networks untersucht. Insbesondere verschiedene Ansätze für eine ressourcenschonende Optimierung bisherig untersuchter Netze werden vorgestellt. Des Weiteren wird betrachtet, wie zeitlich verschobene Pulse die Energierekonstruktionsalgorithmen beeinflussen und wie diese negativen Auswirkungen reduziert werden können. Außerdem werden neuronale Netze vorgestellt, die die Zeit der Energiedeposition rekonstruieren können.

Contents

Acronyms

ADC Analog-to-Digital Converter

AI Artificial Intelligence

ALICE A Large Ion Collider Experiment

ANN Artificial Neural Network

AREUS ATLAS Readout Electronics Upgrade Simulation

ASIC Application-Specific Integrated Circuit

ATLAS A Toroidal LHC ApparatuS

BC Bunch Crossing

BCE Binary Cross Entropy

CERN Conseil européen pour la recherche nucléaire, European Organization for Nuclear Research

CMS Compact Muon Solenoid

CNN Convoluational Neural Network

COReLU Cut Off Rectified Linear Unit

EMB Electromagnetic Barrel

EMEC Electromagnetic End-Caps

FCAL Forward Calorimeter

FEB Front End Board

FEB2 Front End Board 2

FPGA Field Programmable Gate Array

GETP Global Event Trigger Processor

HEC Hadronic End-Caps

HL-LHC High Luminosity Large Hadron Collider

IP Interaction Point

LAr Liquid Argon, Liquid Argon Calorimeter

LASP Liquid Argon Signal Processor

LEP Large Electron-Positron Collider

LHC Large Hadron Collider

LHCb Large Hadron Collider beauty

LLP Long Living Particle

LS3 Long Shutdown 3

MAE Mean Absolute Error

MET Missing Transverse Energy

MRAE Mean Root Absolute Error

MSE Mean Squared Error

OF Optimal Filter

OFMax Optimal Filter with Maximum finder

ReLU Rectified Linear Unit

SM Standard Model of particle physics

THL Tangens Hyperbolicus Linear loss function

1 Introduction

1.1 Motivation

The desire for a better understanding of the universe and the nature of particles leads humanity to more and more complex, extreme and technically challenging experiments. In the context of particle physics the Large Hadron Collider (LHC) at CERN is definitely a peak of physics and engineering performances so far. Driven by the will to validate the predictions of the Standard Model of particle physics (SM) [16] the LHC achieved major accomplishments having an outstanding highlight with proving the existence of the Higgs Boson in 2012 [10] [22].

But even after finding this last main component of the SM and validating many other predictions with an impressive precision, the search for new physics is still going on at the LHC. Physics beyond the Standard Model do not only exist in theory, but they are necessary for explaining some of the unsolved problems of modern science. The existence of dark matter, the hierarchy problem or the neutrino masses are such phenomena to name some of the most famous ones. Many of these problems could be explained with theories in which additional particles occur [38].

However, the physics community was not able to find indications for the existence of such particles at LHC experiments like ATLAS or CMS, yet. This does not necessarily mean, that those particles do not exist, but better techniques might be needed to find them [38].

Additionally, there are still some SM parameters with large uncertainties and unobserved SM processes. This is why it is worth thinking about possibilities of improving the performance of the LHC and its particle detectors even further [38].

1.2 The Large Hadron Collider

The LHC [24] at CERN is the largest particle accelerator ever build and also the one with the highest invariant mass. It accelerates two proton beams in opposite direction with 6.8 GeV for each beam resulting in an invariant mass of 13.6 GeV in the ongoing Run 3. Expressed in velocity this means that the protons travel with 99.9999991% of the speed of light [17] in the circular collider with an circumference of 27 km which takes just about 90 µs.
The beams are not continuously filled with protons but they consist of so-called bunches. These are gaussian distributed packages of protons with around 10^{11} protons per bunch. The spatial extend differs between the beam direction z and radial direction. The standard deviation of the z-distribution is in the order of cm while in radial direction it is only in the order of µm.
The LHC was built in the tunnel of the Large Electron-Positron Collider (LEP), which was the predecessor of the LHC. Since the amount of synchrotron radiation caps the reachable centre of mass energy for circular electron colliders massively, a proton collider was chosen to reach higher energies. To reach 13.6 GeV of invariant mass, also some pre-accelerators are needed, which are shown in figure 1.1.
One bunch is injected every 25 ns with some larger gaps following a specific pattern. This difference between two injections also defines the frequency of crossings at the interaction points (IP). This time difference also defines the commonly used time unit for LHC experiments: the bunch crossing (BC) which is correspondingly 25 ns.
The combination of the very dense proton packages and the high number of protons per bunch results in about 20 proton-proton-collisions at a single bunch crossing at an interaction point fore the design LHC luminosity of $1 \times 10^{-34}\,\mathrm{cm}^{-2}\mathrm{s}^{-1}$. This and the extremely high frequency of 40 MHz lead to a total integrated luminosity of $190\,\mathrm{fb}^{-1}$ at the end of run 2 and it is expected to reach $390\,\mathrm{fb}^{-1}$ at the end of run 3 in 2025.
The two beams cross each other at four different IPs where the main experiments of the LHC are located: ALICE [7], ATLAS [9], CMS [21] and LHCb [15] with their big detector systems placed centered around the IPs. While ALICE and LHCb are detectors specialized for specific events, ATLAS and CMS are so-called general-purpose detectors.

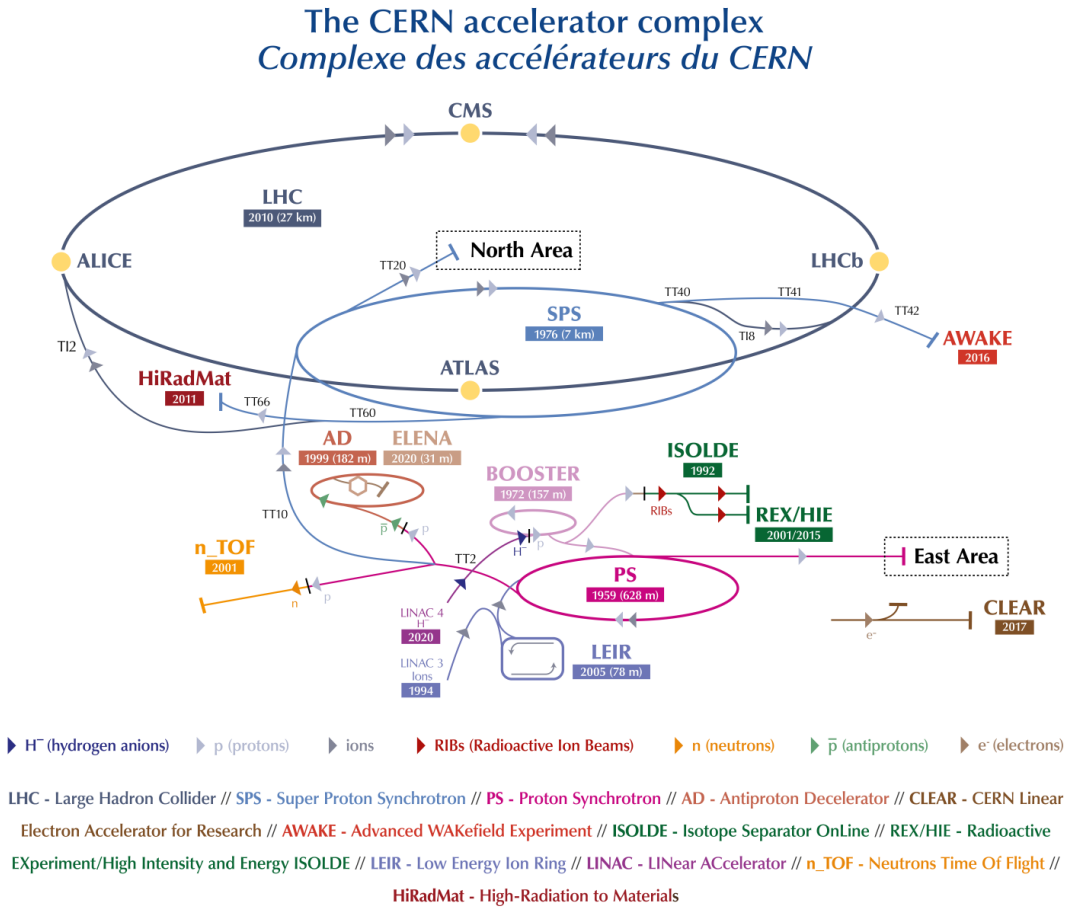

Figure 1.1: Scheme of the LHC including all the pre-accelerators and other accelerators located at CERN. Also the positions of the four main experiments at the LHC, ALICE, ATLAS, CMS and LHCb, are marked. [33]

1.3 The ATLAS Experiment

The ATLAS detector [9], an acronym for *A Toroidal LHC ApparatuS*, is currently the largest particle detector ever built. Like most modern particle detectors, ATLAS consists of multiple subsystems aligned in layers around the beam pipe. Every subdetector is specialized for its specific purpose and also their positions in ATLAS is optimized for these tasks. Since the LHC is a proton-proton-collider, the detector is mirror symmetrical with respect to the xy-plane and radial symmetrical around the beam line. Normally instead of z or the angle to the z-axis Θ, the so-called pseudorapidity η is used to define the position of detector parts. This pseudorapidity is defined as $\eta = -\ln\left(\tan\frac{\Theta}{2}\right)$ which means that $\eta = \infty$ along the positive z-axis, $\eta = -\infty$ for the negative z-axis and $\eta = 0$ in the xy-plane.

The most inner detector part is a tracking detector which again consists of different detector types. Silicon and straw tube detectors measure the trajectory of charged particles. Due to a strong magnetic field created by large solenoid and toroid electromagnets, charged particles will have curved tracks. This will not only give information on the charge of particles but also allows to calculate the momentum by measuring the radii of the tracks.

After the measurement of the direction of flight and the momentum is finished, the energy of the particles should be determined. ATLAS has two different calorimeter systems. The one closer to the center is the Liquid Argon Calorimeter (LAr) which will be described further in the next section. The LAr calorimeter also consists of different detector regions. It is mainly an electromagnetic calorimeter measuring the energy of electromagnetically interacting particles, focusing on electrons and photons, while the LAr calorimeter end-caps are also part of the hadronic calorimeter of ATLAS.

The rest of the hadronic calorimeter is the so-called Tile calorimeter. It uses scintillators and steel absorbers to measure the energy of hadronically interacting particles such as baryons and mesons. Because of the proton-proton-collision, hadronic processes are quite dominant in ATLAS. Measuring the energy of these particles is therefore very important and so-called jet reconstruction is an important task for the data analysis.

The Tile calorimeter should stop all remaining particles besides muons and neutrinos. To measure the muon momenta, so-called muon spectrometers are placed

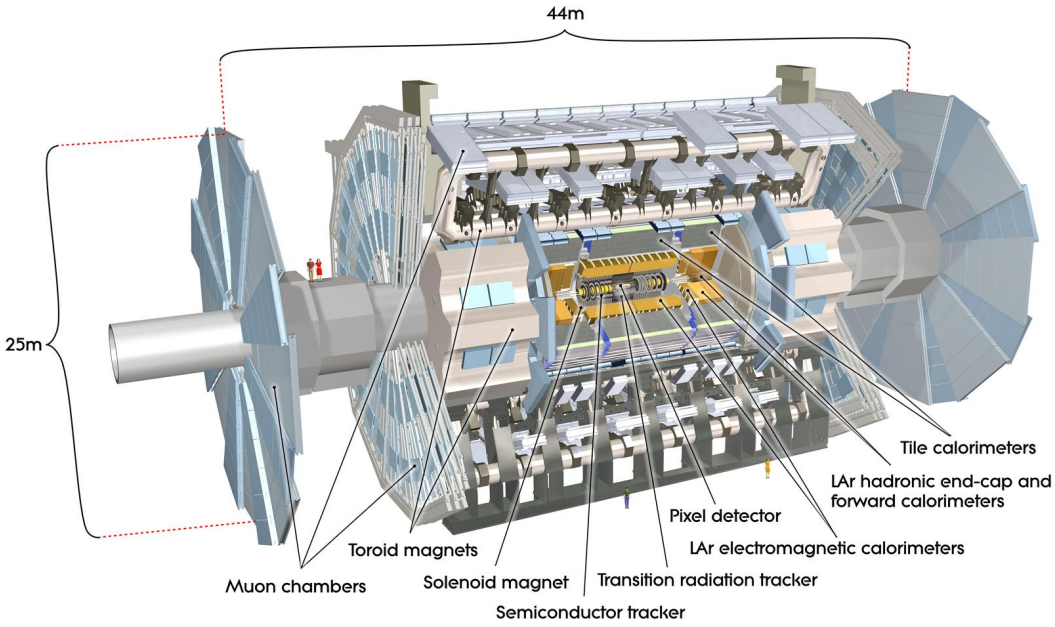

Figure 1.2: Scheme of the ATLAS detector with its different subdetectors. [34]

at the outer part of ATLAS. In the forward regions this subdetector has the iconic wheel shape which can be seen in figure 1.2

The remaining particles, the neutrinos, can not be measured directly. However it is still important to observe the neutrinos and determine their energy. To make this possible, ATLAS is constructed as a nearly hermetic detector which means that particles besides neutrinos can not escape ATLAS without being measured. Knowing the initial properties of the protons and using the information of the observable particles, it is possible to calculate the missing transverse energy (MET) induced by the neutrinos which is a key part of LHC and ATLAS physics. Therefore, the energy of every final state should be determined as exactly as possible.

1.4 The ATLAS Liquid Argon Calorimeter

Although the LHC collides protons and hadronic processes are dominant, electrons and photons are important for the data analysis for multiple reasons. Interesting events often include electromagnetic and weak interactions. For example Higgs

Bosons or $W^{\pm}$ Bosons often decay to electrons or to particles which will decay to electrons later [28]. The Higgs Boson for example was even discovered in 2012 with the $H \to \gamma\gamma$ and $H \to ZZ \to 4l$ processes [10]. Also, hadronic particles like pions and kaons will decay into electrons, photons and muons [28]. Therefore an excellent working electromagnetic calorimeter is extremely important. The Liquid Argon Calorimeter [8] of ATLAS was developed to fulfill this task.

The main parameter which characterizes the performance of the calorimeter is the energy resolution which is given by:

$$\frac{\Delta E}{E} = \frac{a}{\sqrt{\frac{E}{[GeV]}}} \oplus \frac{b}{\frac{E}{[GeV]}} \oplus c \tag{1.1}$$

where $x \oplus y = \sqrt{x^2 + y^2}$. The first term is called sampling term caused by Poisson statistics of the number of free charges in the calorimeter cell. The second term is caused by noise and the third term is a constant defined by the calorimeter's architecture. The parameters a, b and c can be measured. Sometimes the resolution is only handled with the sampling term since especially for higher energies it dominates the noise term and the constant term is relativly small. For the LAr a is about 10 % for the electromagnetic parts and 20 % for the hadronic parts.

The electromagnetic and hadronic parts have different architectural features to meet the requirements for reaching the desired resolutions. Additionally, the particles resulting from the proton-proton-collisions have a specific η-direction distribution, so different detector regions with specific requirements are needed.

The main parts are the electromagnetic barrel (EMB), the electromagnetic end-cap (EMEC), hadronic end-cap (HEC) and the forward calorimeter (FCAL), which has electromagnetic and hadronic parts. The different regions are shown in figure 1.3. All of them have in common that they are using liquid argon as the active material. Charged particles will traverse the liquid argon and produce free charge due to ionization which can then be collected by electrodes. Afterwards the electronic signal is proportional to the energy deposit. The liquid Argon is used because of its well fitting properties on the one hand and its relatively low costs on the other hand. Especially the costs are a big advantage over alternative gases like Krypton.

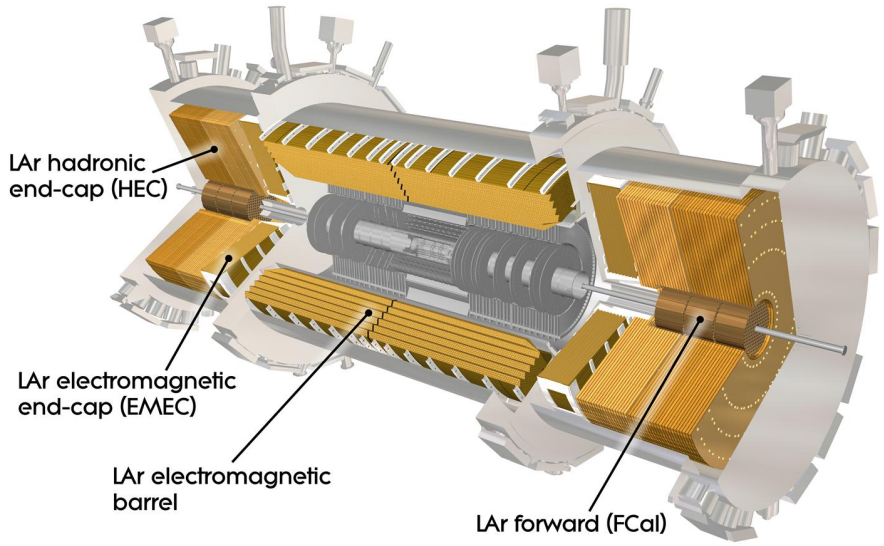

Figure 1.3: Scheme of the LAr calorimeter with its different detector regions. [8]

The whole LAr calorimeter is embedded in multiple cryostats, since the detector has to be cooled down to 89.3 K to reach the liquid state of Argon and optimal conditions.

The electromagnetic calorimeter includes the pseudorapidity range of $|\eta| < 3.2$ and $3.0 < |\eta| < 4.9$ for the electromagnetic part of the FCAL. The EMB and EMEC have a characteristical accordion structure to minimize the appearance of gaps without active material in azimuth direction. This is important to make sure that the MET is indeed treatable as equivalent with the neutrino energy. A scheme of the EMB with its different layers and accordion structure is shown in figure 1.4 and the accordion structure can be viewed in detail in 1.5.

To shorten the radiation length, absorption material is placed between the LAr layers. Electrons, positrons and photons will interact with the atoms of this material and produce electromagnetic showers. Electrons and positrons will emit photons due to bremsstrahlung while high energetic photons, also those produced by bremsstrahlung, will produce electron-positron pairs. These processes are repeated until the photon energy is too small for pair production. For the EMB

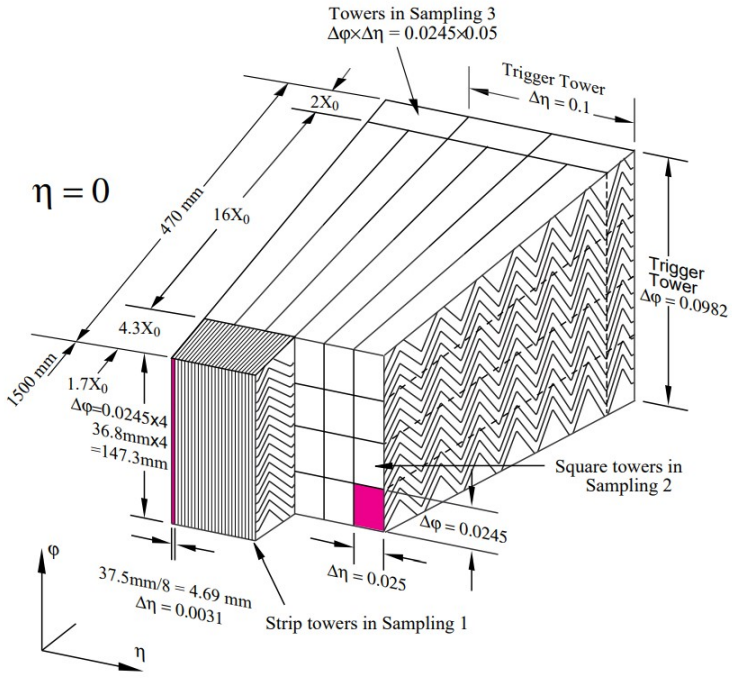

Figure 1.4: Scheme of a section of the EMB with the typical accordion structure of the LAr calorimeter. The three sampling layers with different granularities are displayed. [8]

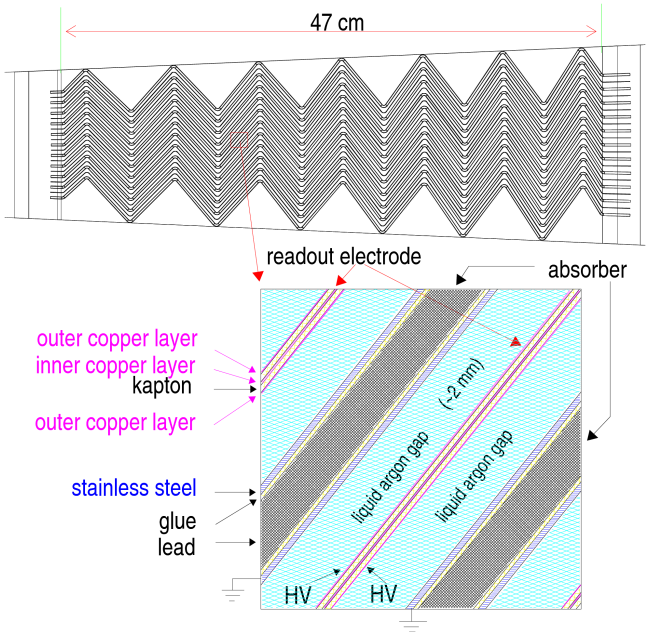

Figure 1.5: Scheme of the accordion strcture of the LAr calorimeter with the readout electrodes, absorber and active material. [8]

and EMEC, lead is used as the absorber material and steel is used to stabilize the detector but also works like an absorber material. The electromagnetic module of the FCAL is using copper as the absorber. The electrodes for the readout are made of copper-kapton board. The structure and the used materials are shown in 1.5.
The EMB and its cryostat is 6.8 m long with an outer radius of 2.25 m and an inner radius of 1.15 m. It consists of different layers. The first layer called presampler is used to correct the energy loss of particles which is created by interactions before reaching the LAr calorimeter.
The presampler is followed by three sampling layers with different properties. The first layer has a very fine granularity in η direction as shown in 1.4. This results in a good spatial and temporal resolution. To limit the number of readout channels the granularity in the following layers is less fine. The second sampling layer is the longest one in radial direction so the biggest part of the energy is deposited here. The last sampling layer got an even coarser granularity and covers less radiation length than the first two sampling layers.
The hadronic end-caps cover the pseudorapidity range of $1.5 < |\eta| < 3.2$ and the FCAL reaches up to $|\eta| = 4.9$. The absorber material of the HEC is copper which is also used in specific parts of the FCAL. However the main parts of the hadronic modules of FCAL are using tungsten for the absorber material which was a quite new technique for calorimeters when the LAr calorimeter was constructed.
All the different detector regions have a total count of 182,468 cells with one readout channel each [12].

1.5 The ATLAS Liquid Argon Calorimeter Readout Electronics and Signal Processing

The extreme conditions of the LHC do not only set high requirements for the detector itself but also for the readout electronics [11]. The high event rate of 40 MHz with up to 20 proton-proton-collisions per BC results in a enormous amount of data which is produced at ATLAS. Since the data which can be collected and saved are limited, very fast data processing and decision making is needed.
The readout electronics need to handle a lot of tasks like pulse shaping, digitiza-

tion, gain selection, noise reduction and trigger decisions. The schematic block diagram of the currently installed readout electronics for Run 3 is shown in figure 1.6. The electronics can be divided into two categories: Front-end and Back-end electronics. The Front-end electronics with the Front-end Boards (FEB) are located directly at the calorimeter's cryostats and perform first necessary operations before the preprocessed data can be sent to the Back-end electronics. There the signal processing, which is important for the global trigger system, is performed. The signals have the shape of a triangular pulse, what is a consequence of the homogeneous magnetic fields with parallel field lines in the detector cells. Since the exact arrival time of particles in each detector cell is unknown, the triangular pulse shapes are not suited well for the signal processing, the pulses are reshaped to bipolar pulses as shown in 1.7. Therefore a so-called $CR - RC^2$ filter is used. Afterwards an analog-to-digital converter (ADC) converts the continuous cell output to a discrete signal which can be used for digital calculations. The sampling rate of 40 MHz is chosen to match exactly to the times of the bunch crossings.
The amplitude of the pulses is proportional to the deposited energy and the value at the peak could be used as the reconstructed energy if there were no noise and pileup effects. However there is noise, especially electronic noise and pileup, which has to be reduced before the actual energy reconstruction.
Therefore a digital filter called Optimal Filter (OF) [6] is used, which is a rather simple but efficient algorithm to minimize the signal-to-noise ratio using linear combinations of values of the data sequence. Let $x(t)$ be the value of the ADC output at the BC t and n is the filter depth. The output of the OF at the BC t is defined by

$$OF(t) = \sum_{i=0}^{n-1} a_i \cdot x(t-i) \tag{1.2}$$

with the filter coefficients $a_0, ..., a_{n-1}$. In theory the number of these coefficients is infinite for a perfect signal-to-noise ratio. At the LAr calorimeter data taking is done with 4 samples since Run 2 due to limited on-detector buffering capabilities. But $n = 5$ is a better value for noise suppression [11]. The coefficients can be calculated mathematically as described in [6] knowing the noise pattern and ideal pulse shape $g(t)$ which is digitized to discrete values g_i. The thermal noise and pile-up noise define the noise autocorrelation matrix R. With g_i, the derivative of

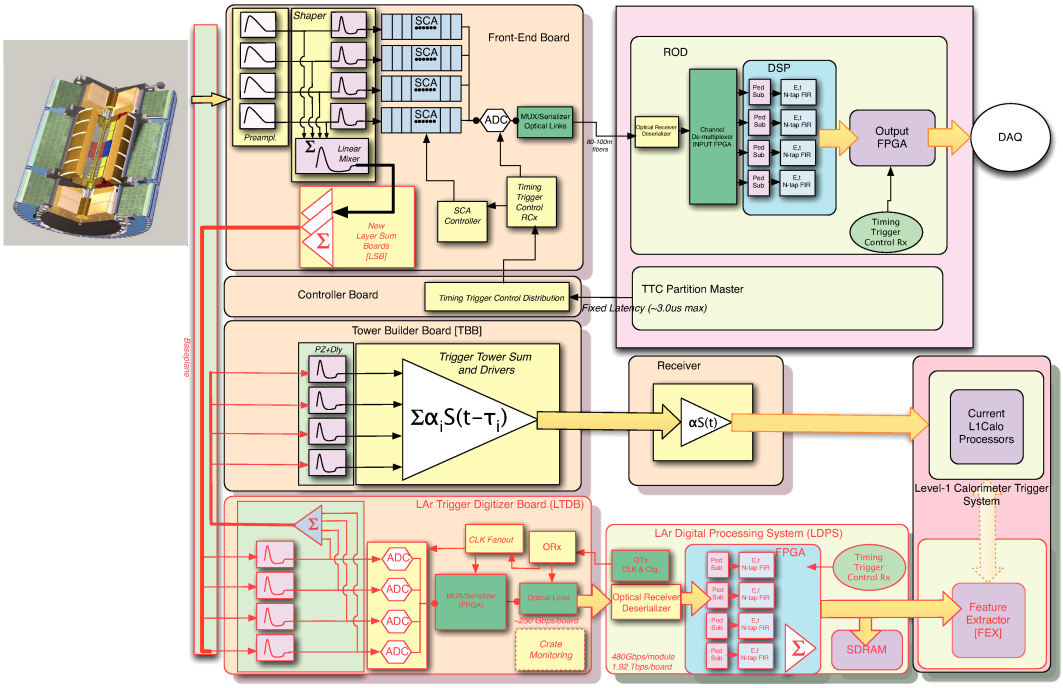

Figure 1.6: Schematic block diagram of the Phase I upgrade readout electronics for Run 3. [11]

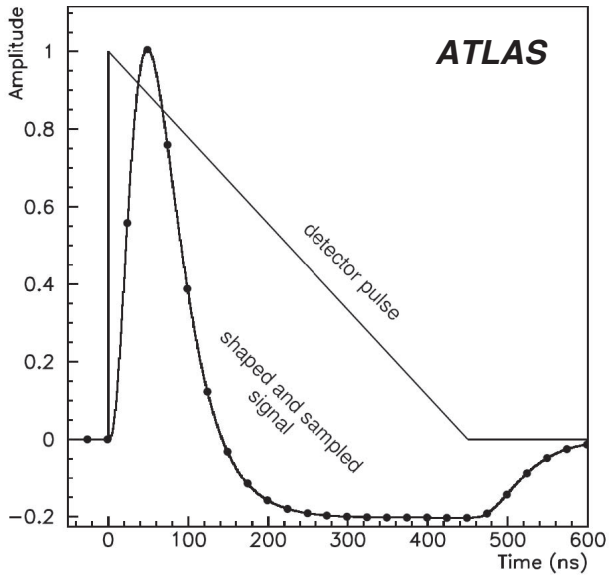

Figure 1.7: Triangular pulse shape as obtained from the detector, the reshaped bipolar pulse and discrete data points after digitization. [8]

the pulse shape g'_i and the inverse of the noise autocorrelation matrix $V = R^{-1}$, the following parameters can be defined:

$$\begin{aligned} &Q_1 = \sum_{ij} g_i V_{ij} g_j \,, \qquad Q_2 = \sum_{ij} g'_i V_{ij} g'_j \,, \qquad Q_3 = \sum_{ij} g'_i V_{ij} g_j \,, \\ &\Delta = Q_1 Q_2 - Q_3^2 \,, \quad \lambda = \frac{Q_2}{\Delta} \,, \quad \kappa = -\frac{Q_3}{\Delta} \,, \quad \mu = \frac{Q_3}{\Delta} \,, \quad \rho = -\frac{Q_1}{\Delta} \,. \end{aligned} \tag{1.3}$$

With these parameters the coefficients a_i can be calculated:

$$a_i = \lambda \sum_j V_{ij} g_j + \kappa \sum_j V_{ij} g'_j. \tag{1.4}$$

Additionally there is another optimal filter OF_τ [6] which reconstructs the product of deposited energy and hit time $E\tau$:

$$OF_\tau(t) = \sum_{i=0}^{n-1} b_i \cdot x(t-i). \tag{1.5}$$

The hit timing can then be used for a correction of the reconstructed energy. The coefficients b_i can be also calculated with the defined parameters:

$$b_i = \mu \sum_j V_{ij} g_j + \rho \sum_j V_{ij} g'_j. \tag{1.6}$$

1.6 The High Luminosity Large Hadron Collider

At the moment the data analysis groups working at ATLAS are using the run 2 data with 13 TeV invariant mass and a total amount of $139\,\mathrm{fb}^{-1}$ of integrated luminosity which is usable for physics analysis while the LHC produced $158\,\mathrm{fb}^{-1}$ at ATLAS and $147\,\mathrm{fb}^{-1}$ were measured [13]. The current LHC is expected to reach an additional integrated luminosity of $160\,\mathrm{fb}^{-1}$ at the end of run 3 in 2024 having $350\,\mathrm{fb}^{-1}$ in total for all runs. While this is an extremely large amount of data, the physics community is convinced that even much more data is needed to find exciting new physics and very rare processes [36].
To reach this goal an upgrade of the LHC is planned. The upgraded LHC will be called High Luminosity Large Hadron Collider (HL-LHC) [22] then and is expected to to reach $250\,\mathrm{fb}^{-1}$ to $300\,\mathrm{fb}^{-1}$ per year, which is more data than the

LHC produced during the whole run 3 in three years.
To reach this high luminosity, many beam properties of the LHC will be optimized to enlarge the number of proton-proton collisions per BC noted as μ, which has to be interpreted as expected value of collisions, the real number can be higher or smaller. The number of protons per bunch will be increased from 115 billion to 220 billion protons and the emittance, the area of a bunch in phase space, will get smaller. Also newly developed so-called crab cavities, shown in figure 1.8, will be installed. These will maximize the overlap volume of two bunches at a bunch crossing leading to more possible proton-proton collisions. Due to these changes, the number proton-proton collisions will get approximately seven times larger from $\mu = 20$ at the LHC to $\mu = 140$ at HL-LHC.
While this is a great improvement for the possibilities in data analysis, it is also an enormous challenge for the detectors since they will face up to seven times higher signal rates and these signals have to be detected and processed.
The upgrade schedule of the LHC and its detectors is shown in figure 1.9.

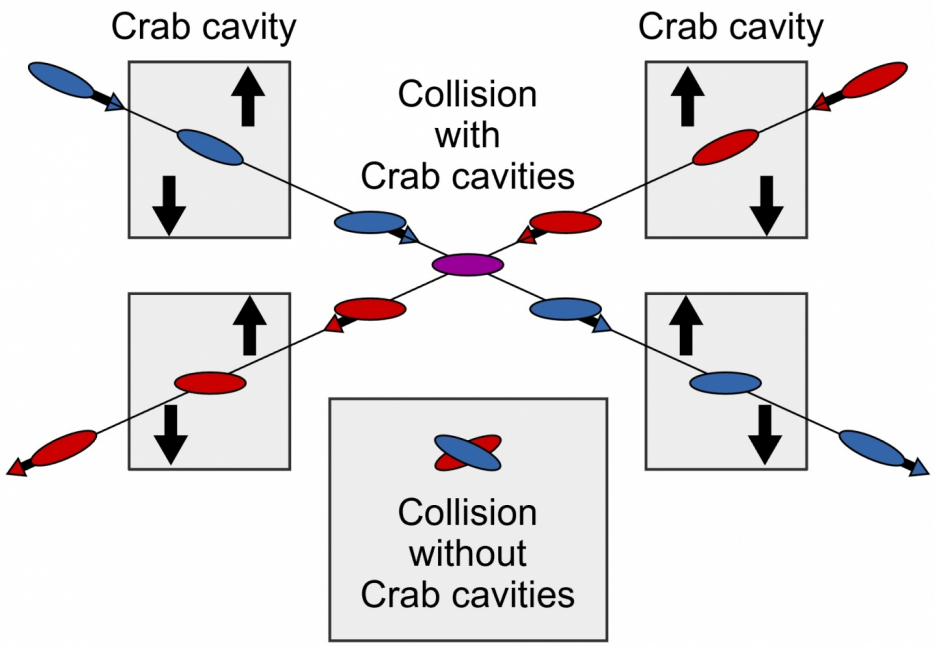

Figure 1.8: Scheme of the functionality of the newly developed crab cavities. The bunches will be rotated just before the bunch crossing so that the overlapping volume is increased compared to the non-rotated bunches like they are used at the LHC. [35]

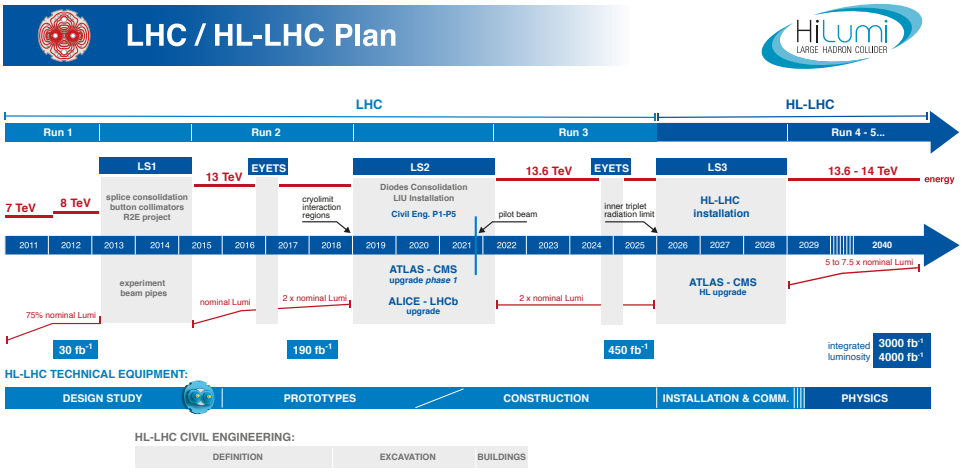

Figure 1.9: Upgrade schedule of the LHC. The long shutdown 3 is planned for 2026. Then the HL-LHC will be installed and the detectors get their upgrades to be ready for the high luminosity. [1]

1.7 Pileup at the High Luminosity Large Hadron Collider

Having 140 *pp*-collisions per BC does not only increase the number of interesting events. Most of the collisions will just increase the number of less interesting hadronic events for the majority of the cells. These particles, mainly pions, result in many small energy deposits per cell and BC which is called called in-time pileup [36].

More events per BC will also increase the chance of observing two events in the same cell with a short temporal distance. Since one pulse has a total length of about 25 BC, smaller temporal gaps between two events will result in an overlap of both pulses which is shown in figure 1.10. This so-called out-of-time pileup is a challenging problem for the signal processing because the OF is correcting out-of-time pile-up on average, but not for each individual BC. If the height of the OF output is taken as the reconstructed energy without more complex algorithms, this will lead to underestimated energies for short gaps as shown in figure 1.10 [27].

The high amount of pileup will impact the energy resolution if no advanced signal processing technique will be used. The figures 1.11 and 1.12 show that the energy resolution for photons and electrons will decrease with an increasing number of collisions per bunch crossing μ [12].

Additionally to the requirement of an improved signal reconstruction, the limited radiation tolerance of the current front-end electronics and the need of larger data buffers for the desired higher trigger rate of 1 MHz, lead to the decision to replace the readout electronics [12].

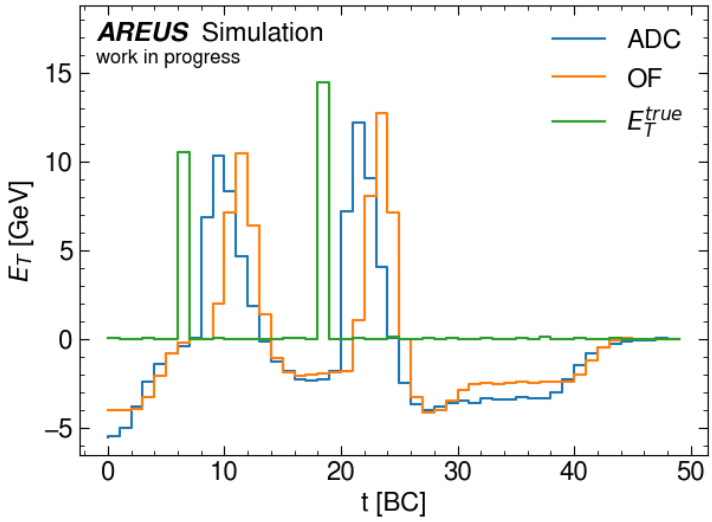

Figure 1.10: Example of a sequence with out-of-time pileup before filtering (ADC) and afterwards (OF). Also the actual energy deposit is shown. The second energy deposit follows very quickly after the first one so both pulses overlay each other.

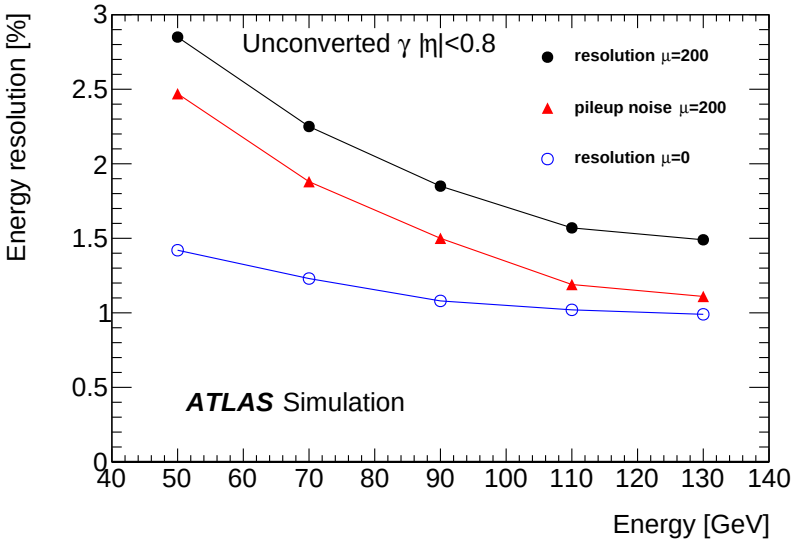

Figure 1.11: Resolution of energy measurement for photons depending on their energy for different mean number of collisions per BC. The blue data points show the resolution for a photon without pile-up. The black data points are the photon's energy at $\mu = 200$ and the red data shows the influence of pileup noise at $\mu = 200$. [12]

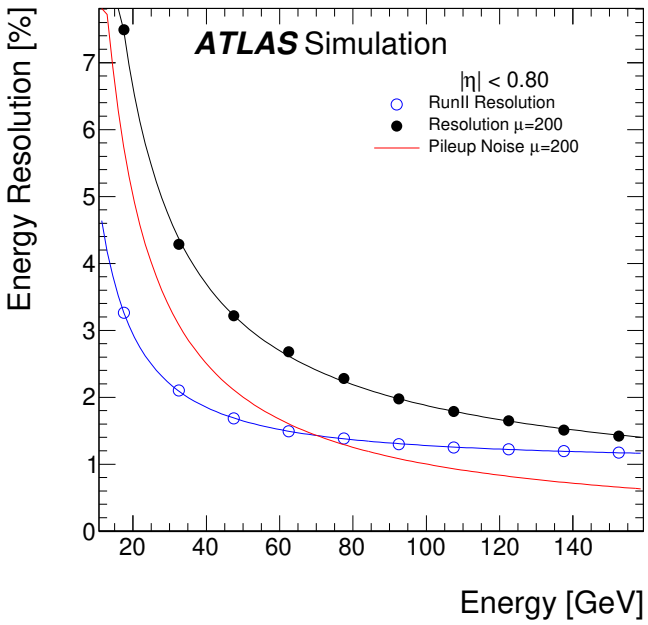

Figure 1.12: Resolution of energy measurement for electrons depending on their energy for different mean number of collisions per BC. The blue data points are showing data from Run 2 while the black curve shows simulated data for $\mu = 200$ and red line is the influence of pileup at $\mu = 200$. [12]

1.8 The ATLAS Liquid Argon Calorimeter Phase-II Upgrade

The actual calorimeter cells will not get upgraded for the HL-LHC because they should be able to work properly under the high luminosity conditions. However due to the mentioned increased radiation and pileup and ATLAS new trigger scheme it is necessary to upgrade the electronics of the LAr calorimeter. This so-called Phase-II upgrade [12] will take place during the third long shutdown (LS3) of the LHC when the LHC will be upgraded to the HL-LHC. The new layout is shown in figure 1.13.
The increased radiation dose led to the decision to replace the FEBs with new Front-end electronics boards (FEB2) while they will perform the same operations as in the Phase-I design [11]. New application-specific integrated circuits (ASIC) containing the preamplifiers and shapers are developed. Also the ADC will be replaced. The new electronics are designed to be more resistant to radiation. Every FEB2 will have two connectors with 64 channels each resulting in 128 total inputs. One input is needed per cell so 1524 FEB2s will be needed to read out the whole calorimeter. Additionally a clock and several other chips used for sending data to other boards are integrated on the FEB2.
Another big change will be the new LAr Signal Processor (LASP) with its field-programmable gate array (FPGA) [37]. Every LASP FPGA will get the data from three FEB2s via optical links to minimize the delay of signals. This results in a total number of 384 calorimeter cells one LASP FPGA has to process. The FPGA have to perform several algorithms. The most important one is the algorithm for the reconstruction of the energy and optionally the hit time. Aan OF as described in section 1.5 could be used or an advanced algorithm. Since the FPGA will have to process the output of 384 detector cells, the hardware resources for these algorithms are limited.
LASP data will be sent to the Global Event Trigger Processors (GETP) which is responsible to decide if the ATLAS detector should read out the data of an event or not. This shows how important the performance of the LAr and its signal processing is.

Also the trigger scheme will be changed. With the new scheme the ability to perform measurements of events in consecutive bunch crossings is desired. Not only the hardware has to be renewed for that, also the signal processing algorithms are challenged by this trigger scheme. Here, alternative solutions should be discussed to exploit the full potential of the HL-LHC.

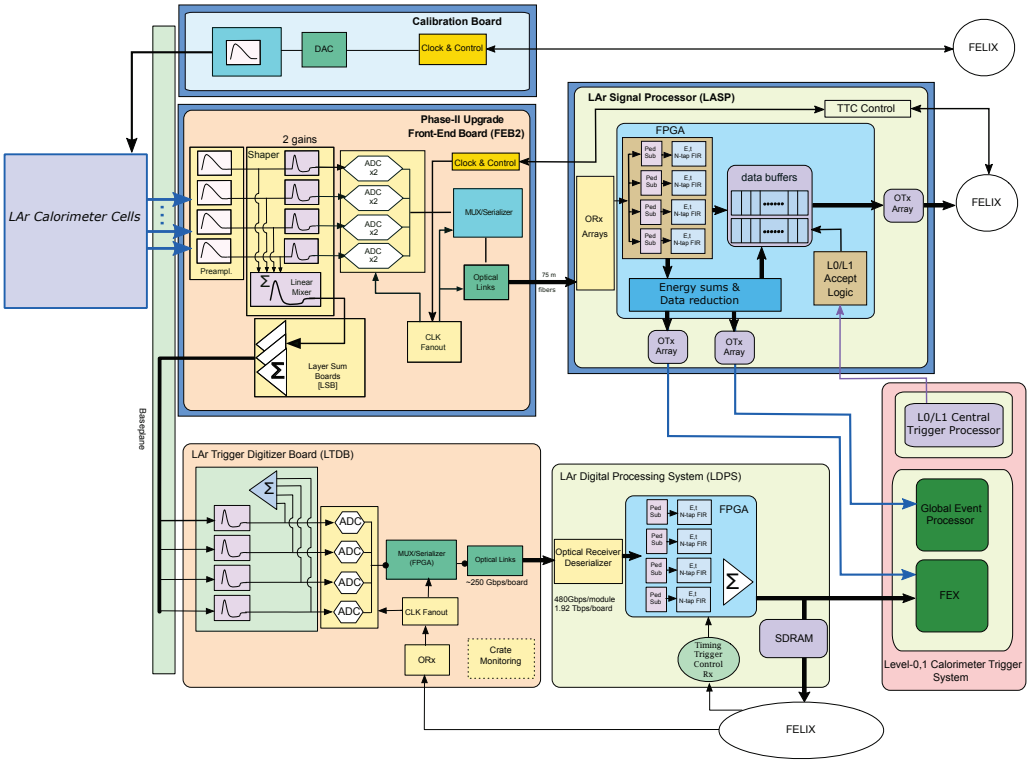

Figure 1.13: Schematic block diagram of the Phase II upgrade readout electronics for Run 3. [12]

1.9 The ATLAS Readout Electronics Upgrade Simulation

To test the influence of increasing event rates, new trigger schemes and other new effects on the readout electronics, a simulation software called "ATLAS Readout Electronics Upgrade Simulation" (AREUS) [32] is used. AREUS simulates how particles resulting from proton-proton collisions hit single cells of the LAr calorimeter and how these hits produce pulses. These pulses are then shaped and digitized exactly the same way, the electronics at the detector would do. Afterwards there is the possibility to activate filters like the mentioned OF. The calculation of the coefficients of the OF follows the principle described in [6]. Also, multiple evaluation methods for the performance of filters are included. The output of the resulting data and intermediate steps is given in ROOT files. These files can then be used for advanced analysis.
Using a simulation software is not only necessary for checking future changes. The possibility of knowing the true energy leading to specific pulses is a big advantage which is not possible to achieve if actual data from the detector would be used.

1.10 Machine Learning and Artificial Neural Networks

Computer algorithms are able to solve problems very easily, which are extremely hard to solve for humans. Simulating complex physical processes, finding the best possible play in chess or calculating the prime factors of a number: if there is a way to formulate a task in logical and mathematical expressions, computers are able to outperform humans. However, some tasks that are very simple for humans are hard to formalize for a computer program. For example the recognition of animals, faces or even shapes is rather complicated for algorithms [30, Chapter 1]. To solve this issue, humanity tried for a long time to find ways to make computers think intelligently. In the last couple of years, the development of artificial intelligence (AI) made a big step and today AI is used in many fields of science and every-day life. Most of these AI technologies are using artificial neural networks (ANN) with machine learning algorithms [30, Chapter 1].

1.10.1 Convolutional Neural Networks

Mathematically an ANN is a graph with vertices, called neurons, and edges which define how the neurons are connected to each other. Data are passed through the network from neuron to neuron while every neuron performs a calculation $g_i(x)$ on the data. In most cases, many of these neurons are arranged in layers. Neurons in the same layer are not connected to each other but only to neurons in the previous and following layer so that the output of a layer can be interpreted as a function $f_j(x) = f_j(g_{j1}(x), ..., g_{jN}(x))$. The network output is the sequential calculation of these functions so basically their composition[30, Chapter 6]:

$$\text{output} = f_N(f_{N-1}(...f_1(\text{input})...)). \tag{1.7}$$

A scheme of a simple ANN is shown in figure 1.14. Arrows denote connection between neurons, shown as circles. The output of a neuron will be given as an input to the neurons connected to it.
A special case of ANNs are Convolutional Neural Networks (CNN) [23][30, Chapter 9]. These networks consist of at least one layer which performs a mathematical convolution. Let x be the input of the layer and may y be the output. There will be a set of parameters w, called kernel, and a set of parameters b, called bias, such that:

$$y = w \otimes x + b. \tag{1.8}$$

Since both x and y are multidimensional tensors in general, this product has to be understood as a tensor product.
The total size of the kernel is defined by the number of input data points used in one convolution, also-called kernel size, the number of input dimensions and the number of output dimensions, which are called filters. The name filter is chosen because the different weight sets can accentuate specific properties of the data. The bias can shift the whole output by a constant.

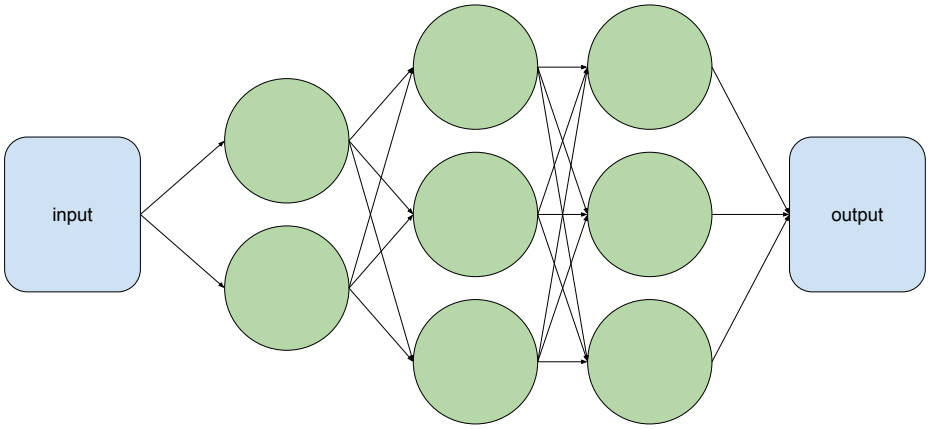

Figure 1.14: Scheme of an ANN with 3 layers, 2 neurons in the first layer followed by 2 layers consisting of 3 neurons each.

In the following, an example with a CNN consisting of two layers, where input and output are 1D-vectors is presented. The first layer has a kernel size of $k_{s,1}$ and n filters. The second layer has a kernel size of $k_{s,2}$. The output of the CNN is then calculated as the composition of two tensor products:

$$y_i = w' \otimes (w \otimes x + b) + b'. \tag{1.9}$$

Or written with the tensors components:

$$y_i = \sum_{k=1}^{k_{s,2}} \sum_{j=1}^{n} w'_{jk} \left(\sum_{m=0}^{k_{s,1}} w_{mj} x_{i+m} + b_j \right) + b'. \tag{1.10}$$

Visualized as a graph, this CNN would look like the one shown in figure 1.15, where $k_{s,1} = 3$, $k_{s,2} = 2$ and $n = 2$.

When the convolution performed by a layer as described in equation 1.8 is applied many times like described in equation 1.7, the composition of all these convolutions allows to apply complex operations. Nowadays, such CNNs are an important tool for object recognition in images [30, Chapter 9].

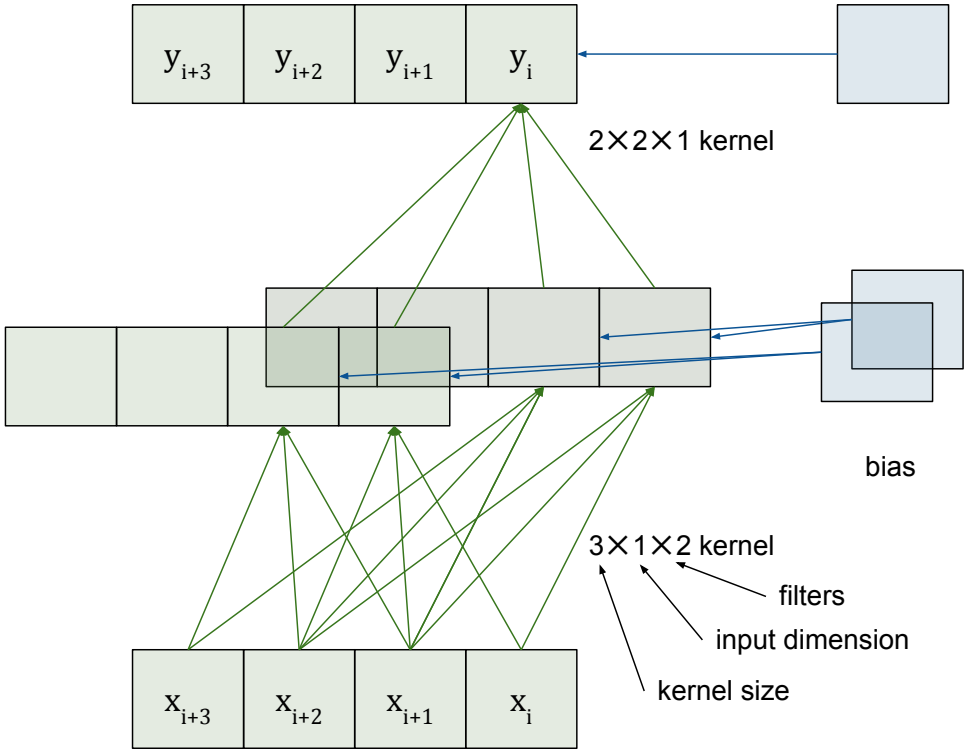

Figure 1.15: Example for a relatively small CNN with one dimensional input and output and a two-dimensional output of the first layer. The green arrows symbolize the multiplication of weights and the addition of these products. The blue squares symbolize the bias and the blue arrows symbolize the addition of them. To calculate the output y_{i+1} the CNN would be applied to the input values x_{i+1} to x_{i+4}

1.10.2 Machine Learning Algorithms

A machine learning algorithm is a program that uses data sets to learn properties of this data. There are different categories of machine learning such as unsupervised and supervised learning. Unsupervised learning uses training data and learns specific features of this data set. A supervised learning algorithm uses training data and target data to learn a specific context between input data and the desired output. In this thesis the supervised learning method was used [30, Chapter 5].

For the application with ANNs a common way to implement machine learning is the gradual adjustment of the weights and bias [30, Chapter 6]. Therefore

at the beginning of the training an initial set of the parameters will be chosen randomly, often with a normal or uniform distribution. Then the algorithm needs information about which parameters are leading to good results. For that reason, so-called cost or loss functions [30, Chapter 6], named Λ here, are used. The loss function uses the target data y_{true} and the output predicted by the ANN y_{pred} to calculate how good the prediction is. For a given ANN architecture the prediction is a function of the input data x and the set of parameters Θ:

$$\Lambda = \Lambda\left(y_{\text{true}}, y_{\text{pred}}\right) = \Lambda\left(y_{\text{true}}, x, \Theta\right). \tag{1.11}$$

The goal of machine learning is to minimize this loss by finding an optimal choice of Θ. Since an analytical calculation of this minima is not possible in many cases, a gradual adjustment of the parameters is performed.
Therefore, the gradient $\nabla_{\Theta}\Lambda$ of the loss function is calculated. This gradient can be used to determine the direction and the strength of change of every parameter Θ_i. For a better search for the minima it is convenient to adjust the strength of change with the so-called learning rate r_l. The adjustment of the parameter Θ_i is then:

$$\Delta\Theta_i = \frac{\partial}{\partial\Theta_i}\Lambda \cdot r_l. \tag{1.12}$$

Every trainable parameter gets adjusted this way. This procedure is repeated for a specified number of epochs and in the best case a local minimum was found then. This is called training in machine learning. A simplified scheme of a training is shown in figure 1.16. It also shows that the initial guess of the parameters influences the success of a training.

1.10.3 Loss Functions

The success of a training in machine learning highly depends on the loss function which is used. On the one hand, the loss function defines which value is minimized in the training, so if a loss, which does not fit to the data and the desired output, is used, the training will not lead to the desired results. For example there are different loss functions suitable for classification problems and for regression problems. On the other hand, the loss function defines the geometry of the loss plane

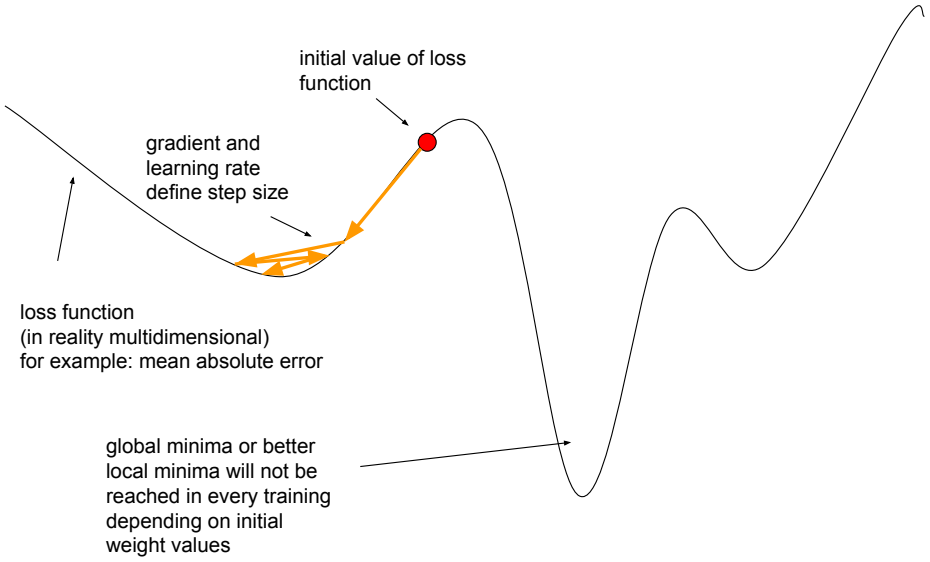

Figure 1.16: Scheme of a training process where the parameters are adjusted gradually to reach a minima in the loss function. The Influence of the initial parameters can be seen.

where the learning algorithm searches for a minima. Too complex loss functions may cause minima which are hard to reach.
Two commonly used loss functions are the mean absolute error (MAE) [5] and the mean squared error (MSE) [5]:

$$MAE = \frac{1}{N}\sum_{i=0}^{N}\left|y_{\text{true},i} - y_{\text{pred},i}\right|, \tag{1.13}$$

$$MSE = \frac{1}{N}\sum_{i=0}^{N}\left(y_{\text{true},i} - y_{\text{pred},i}\right)^2. \tag{1.14}$$

In the following, the influence of the chosen loss function will be clarified by these two examples. Since the MAE only takes the absolute difference of every data point into account, every data point influences the loss almost in the same way. Outliers in the data will not disturb the training's success since reducing the loss of the many regularly looking data points will lead to the same result. This may result in many well fitting outputs while some few outputs have high deviations. The MSE increases more for outliers than for regular data points. Those outliers will be handled better when the ANN is trained with the MSE instead of the MAE but the ANN may perform slightly worse on regular data points.
An example for a loss function suitable for classification problems is the binary cross entropy (BCE) which is used for binary classification where $y_{\text{true},i} = 1$ or $y_{\text{true},i} = 0$ and $0 \leq y_{\text{pred},i} \leq 1$:

$$BCE = \frac{1}{N}\sum_{i=0}^{N} y_{\text{true},i}\log\left(y_{\text{pred},i}\right) + \left(1 - y_{\text{true},i}\right)\log\left(1 - y_{\text{pred},i}\right). \tag{1.15}$$

1.10.4 Activation Functions

To increase the performance of ANNs, so-called activation functions can be implemented. An activation function α is applied to the output of a layer, so that in case of a CNN the layer output is [19]:

$$y = \alpha\left(w \otimes x + b\right). \tag{1.16}$$

Activation functions can add non-linearities which may increase the performance [19]. Also, the geometry of the activation can help the ANN to find the distribution

of the target data or to make sure to comply with the restrictions needed for the output. In the second case, the output layer of the ANN needs the corresponding activation function. If the output should have only none negative values, a rectified linear unit (ReLU) [31] could be used. For desired output values between 0 and 1, for example if the output should be a probability, the so-called sigmoid function could be a reasonable choice [19]. The graphs of those two often used activation functions are shown in figure 1.17.

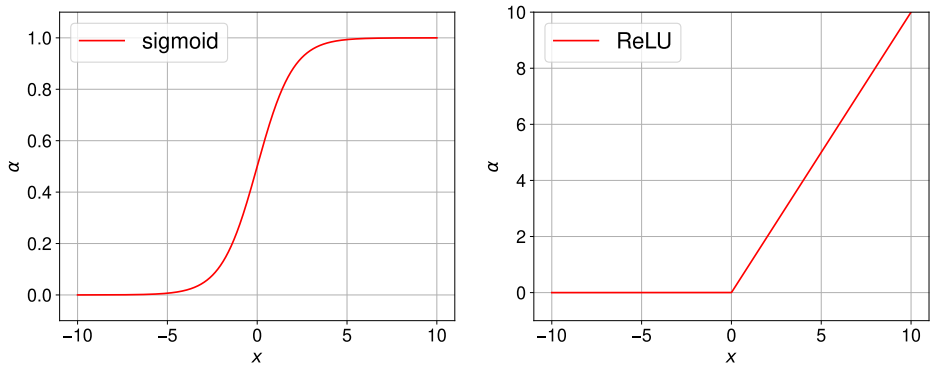

Figure 1.17: Graphs of the sigmoid activation function (left) and ReLU activation function (right).

The sigmoid function:

$$S(x) = \frac{1}{1 + e^{-x}} \tag{1.17}$$

has the advantageous property that its derivative can be calculated easily:

$$S'(x) = S(x)(1 - S(x)). \tag{1.18}$$

The ReLU function is defined as:

$$\mathrm{ReLU}(x) = \max(0, x)\,. \tag{1.19}$$

2 Energy Reconstruction of LAr Signals using CNNs

2.1 3-layer and 4-layer Convolutional Neural Networks

The Optimal Filter described in section 1.5 will reach its limits at the amount of signals and pileup expected at the HL-LHC. The OF does not handle the pileup individually and especially a signal following a high energy deposit will not be detected properly by the OF. If such signals are not detected, the trigger system of ATLAS will not start the data readout. Interesting events could get lost. Therefore, alternative algorithms, which handle the pileup better, are searched for. ANNs as described in reference [27] could be such an alternative. Different ANN types are studied at the moment and seem to be promising candidates for this challenge.

In reference [27] two different CNN architectures were explored which will be presented here. Both of them consist of two parts, so called sub-networks. The first part is called tagging part, consisting of two convolutional layers with sigmoid functions as activation. The first layer has 5 filters with a kernel size of 3, the second has a kernel size of 6 and one filter to match the one dimensional output. The input of the first layer is the ADC output of the LAr cell. The output of the tagging part is concatenated with the ADC output and passed to the second sub-network which is called energy reconstruction part. There are two different architectures of the energy reconstruction part. For the so called 3Conv CNN the energy reconstruction part consists of one layer with one filter and a kernel size of 21. The so called 4Conv CNN has two convolutional layers in its energy reconstruction part, the first with 3 filters and a kernel size of 4 and a second

layer with 1 filter and a kernel size of 3. Both versions have ReLU functions as activation in the energy reconstruction layers. This ensures that the reconstructed energies have non-negative values. A scheme of the 4Conv network is shown in figure 2.1.
Every layer gets a bias and the initial parameter values are normal distributed random numbers with a mean of 0 and a standard deviation of 0.001. A causal padding is chosen so that the kernel only uses data points that came in before the evaluated data point.
The training is executed in two stages [27]. At first the tagging part is trained, for which AREUS samples are used. The target output is 0 when a energy deposit is smaller than 3σ of the total noise and 1 for higher energies. For the here investigated detector cell of the EMB middle layer with $(\eta, \phi) = (0.5125, 0.0125)$, this 3σ threshold is 240 MeV. The sigmoid activation forces the CNN's output to be between 0 and 1. The training is done with the BCE loss function.
Pre-training this CNN part causes a higher chance for a successive training for the second part, the energy reconstruction sub-network. This effect is often used in machine learning, for example in [18].
Afterwards, the whole CNN is trained to perform the energy reconstruction. Again the data are generated with AREUS. During this training also the tagging part gets retrained as well. The property that the tagging parts should return 1 if there was a significant energy deposit is lost and the tagging layers take over parts of the energy reconstruction.
To build and train the CNNs the Python framework Tensorflow [3] and especially Keras [2] were used.

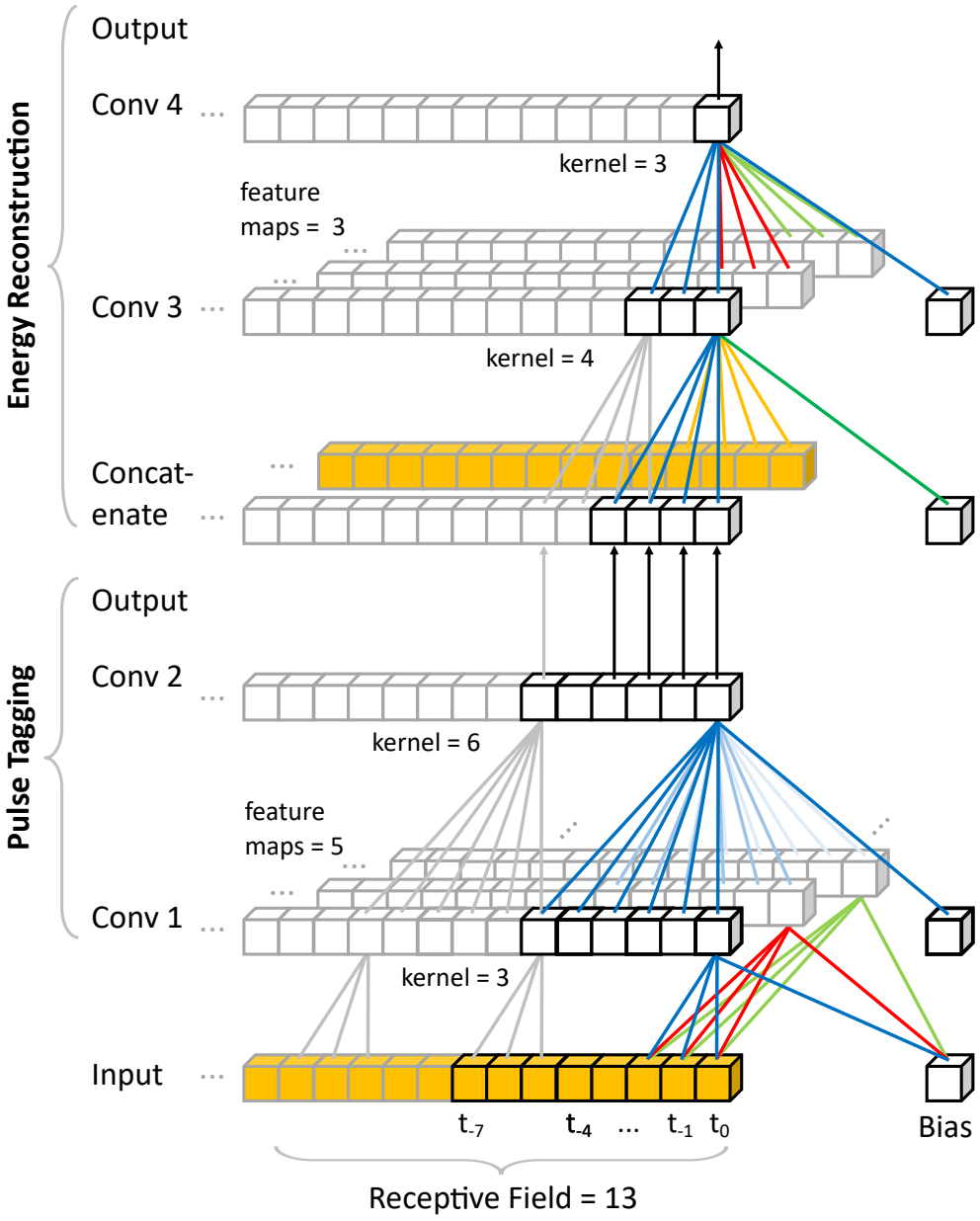

Figure 2.1: Schematic architecture of the 4Conv CNN. [27]

2.2 The Performance of 3Conv and 4Conv Networks

To validate the performance of the ANNs multiple indicators are used. The energy resolution of the ANNs should be as good as possible, but at least it should be better than the OF. Also, it is important that they reconstruct as many energy deposits as possible while achieving a reliable background rejection. Since the OF's biggest problem is the out-of-time pileup, special attention is given to the performance for small temporal gaps between two high-amplitude pulses. To make the ANN's output more comparable to the OF, a simple maximum finder is used, which returns reconstructed energies. The output of the OF with a maximum finder is called OFMax.

To analyze the signal efficiency and background rejection, in [27] so called ROC-curves [25] were analyzed. These show, how the background rejection depends on the signal efficiency, which is set by selecting a signal threshold. The ROC-curves for the OFMax, 3Conv and 4Conv CNN are shown in figure 2.2. It can be seen that the ANNs perform better since, for equal background rejection, they have higher signal efficiencies than the OFMax.

However, the energy reconstruction is no classification task but a regression. Therefore an energy threshold which defines signal and background has to be chosen manually and was chosen to be 3σ of total noise. In this work, a better way to analyze the signal detection and background rejection, was aimed for. A good classifier for well working background rejection, which was found, is the rate of fake energies where $E_T^{\text{true}} = 0\,\text{GeV}$ and $E_T^{\text{pred}} > 0\,\text{GeV}$. This method is independent of a manually chosen threshold and differentiates between smaller and higher fake energies. This information is useful, because reconstructing many high fake energies could lead to overestimated missing transverse energy. A histogram of these fake energies is shown in figure 2.3. In this work, these fake energies instead of ROC-curves will be used to classify the background rejection.

The 3Conv network performs very similar to the OFMax while the 4Conv network reconstructs fewer fake energies lower than 0.5 GeV but has up to 100 times more entries with $E_T^{\text{fake}} < 0.3\,\text{GeV}$ compared to the OFMax. While this effect can be observed for many trainings of the 4Conv, it does not occur for the 3Conv networks. It seems to be inherent in the architecture of the 4Conv CNNs.

The resolution of the energy reconstruction is improved by the CNNs, especially

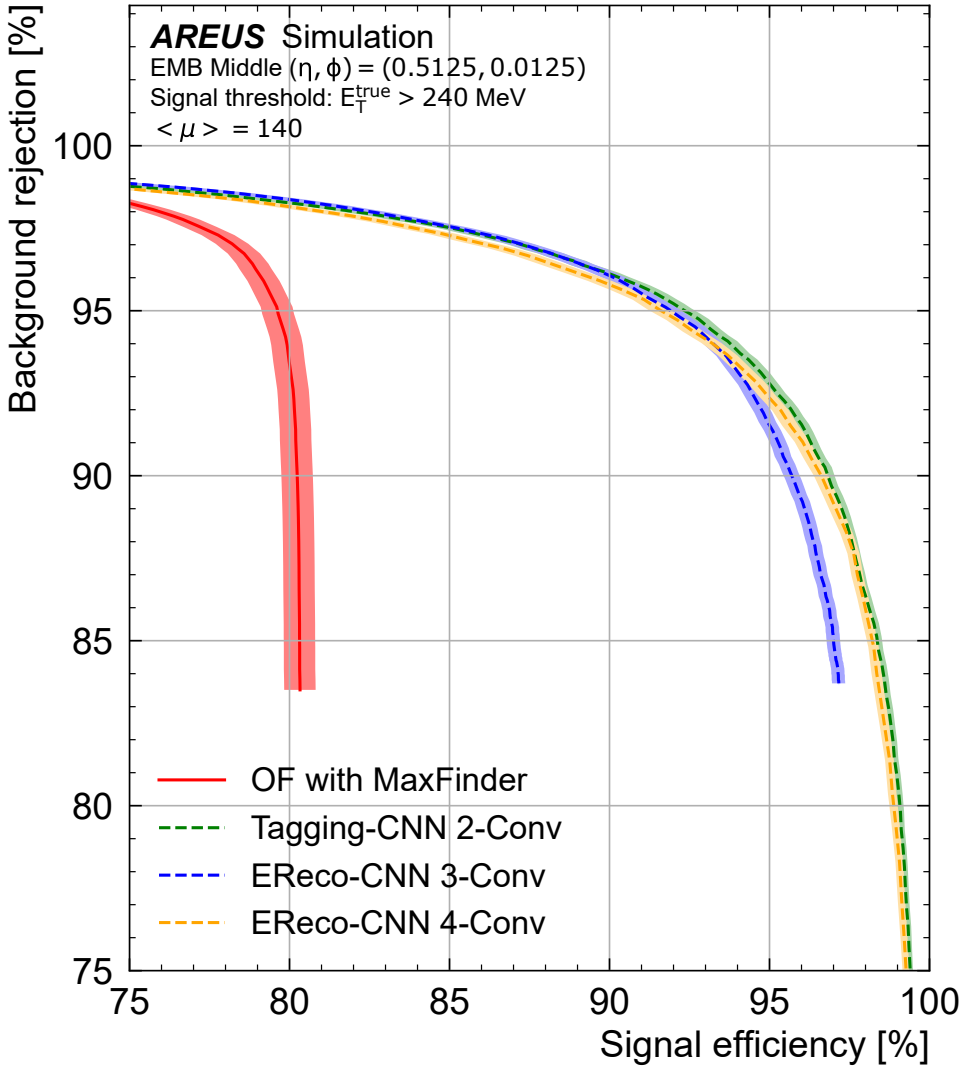

Figure 2.2: ROC curves for OFMax, the tagging sub-ANN, 3Conv and 4Conv. The ROC-curves are showing the background rejection over the signal effiency. Curves that are closer to the upper right corner at $(100\,\%, 100\,\%)$ perform better which means that the CNNs outperform the OFMax. [27]

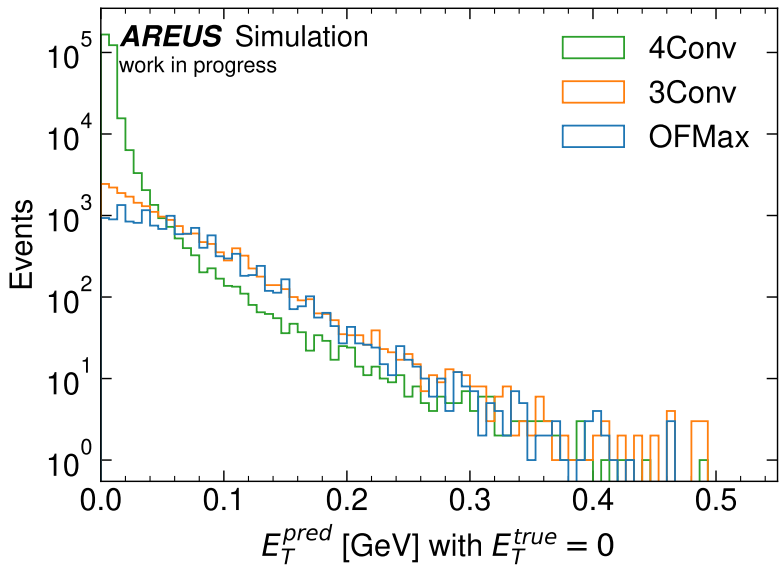

Figure 2.3: Histogram of fake energies for OFMax, 3Conv and 4Conv ANN. While OFMax and the 3Conv network have a similar distribution of fake energies, the 4Conv produces a lot of fake energies with $E_T^{\text{true}} < 0.03\,\text{GeV}$.

for the 3Conv network as shown in figure 2.4. The OF tends to underestimate energies which is caused by the undershoot of the bipolar pulses. This can also be seen in figure 2.5.

It is clearly visible that the CNNs have less underestimated energies when the gap to the previous pulse is smaller than 20 BC, which corresponds to the length of the pulse's undershoot. The 4Conv network seems to struggle with small gaps but the performance loss is smaller than for the OFMax. The 3Conv handles those small gaps very well until the gap is smaller than 4 BC, where the peaks of both pulses are overlapping. At this point the ANN is not able to distinguish the signals.

All in all, the CNNs outperform the Optimal Filter for $\mu = 140$. However, there are still cases which have to be tested. As a part of this master thesis, some of the open questions will be studied in more detail. These questions will be presented in the next section. Since the 3Conv network seems to perform slightly better than the 4Conv network, the analysis will focus on this CNN type.

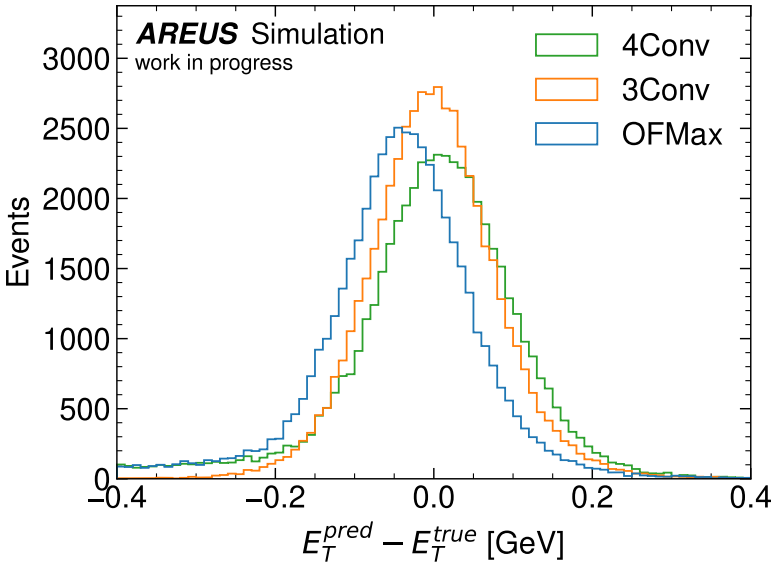

Figure 2.4: Histogram of difference between predicted and actual energies for OFMax, 3Conv and 4Conv ANN. The 4Conv network have a broader energy difference distribution than the OFMax but the 3Conv network outperforms the OFMax.

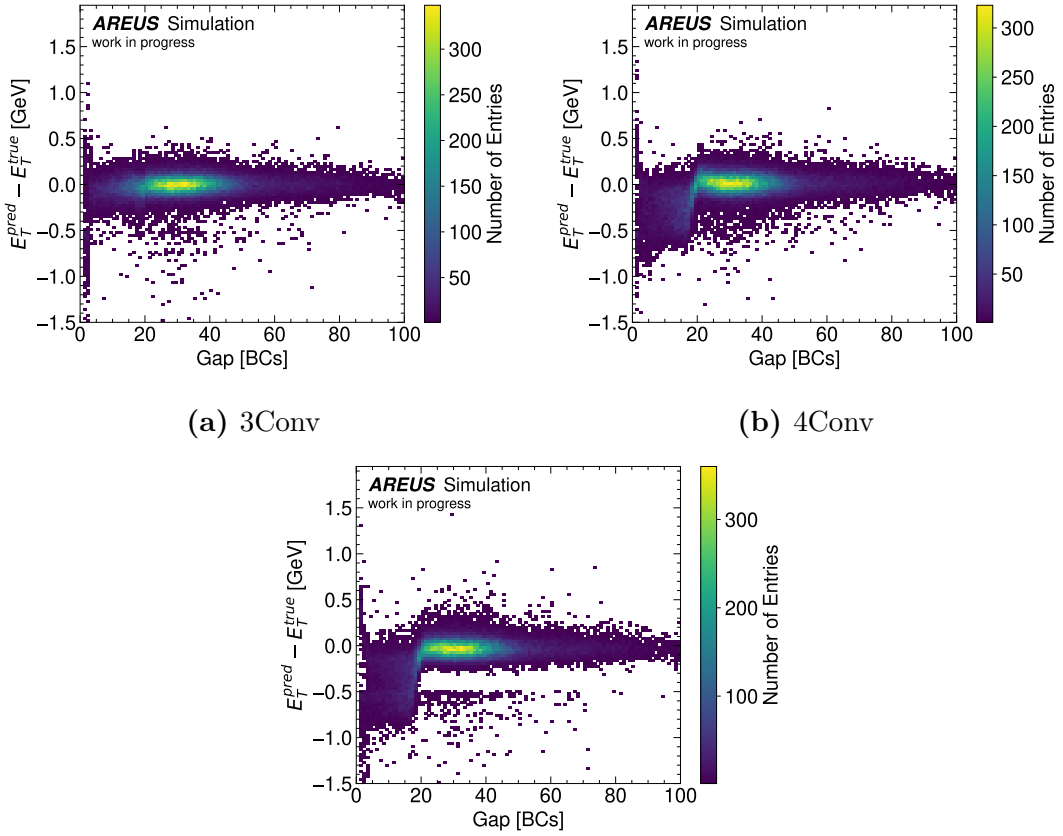

(a) 3Conv

(b) 4Conv

(c) OFMax

Figure 2.5: 2D Histogram of difference between predicted and actual energies over the gap to the previous pulse with an energy above 0.5 GeV for OFMax, 3Conv and 4Conv ANN. The CNNs clearly outperform the OFMax for small gaps < 20 BC.

2.3 Open Difficulties and Problems

2.3.1 Overall Performance and Reproducibility

As described in section 1.10.2, the training of ANNs is a statistical process since the initial parameters are chosen randomly. The performance of the same ANN architecture may vary strongly when the network is trained multiple times, depending on how the initial values are chosen.

Even if the performance of 3Conv and 4Conv network described here is better than the OFMax, this is not the case for most of the trainings. To check the reproducibility, the 3Conv ANN was trained 100 times on a training data set with pileup which is realistic for $\mu = 140$ and artificially inserted hits with uniformly distributed energies up to 5 GeV for half of the data and 30 GeV for the other half. For the data set with energies up to 5 GeV, the temporal distance between two of these hits is normal distributed with a mean distance of 30 BC and a standard deviation of 10 BC. The 30 GeV data set contains hit with a constant gap of 45 BC. The CNNs are evaluated on another data set where the temporal distance between two artificially inserted hits up to 5 GeV is normal distributed with a mean distance of 30 BC and a standard deviation of 10 BC. The distribution of the difference between predicted and actual energies for deposits above 1 GeV were analyzed and evaluated in terms of the mean and standard deviation of the energy resolution. Additionally the number of fake energies in different energy regions was studied.

Not a single training resulted in such a good performance as the 3Conv network from [27]. Also just 6 trainings had a performance which is comparable with or slightly better than the OF. All other trainings performed worse, some of them even significantly.

This points to two issues. Criteria are needed to decide whether to use a training or continue to find a better result. Since the detector is recalibrated from time to time and the ANNs may need to get retrained, a more efficient training concept needs to be developed in order to save CPU or GPU time. This shows that improvements of the training structure or CNN architecture are desirable.

2.3.2 Specialization of the CNNs

The 3Conv and 4Conv networks from [27] were trained on two data sets generated with AREUS. Both sets have a pileup spectrum which is realistic for $\mu = 140$ and artificially inserted hits with uniformly distributed energies. One data set contains hits up to 5 GeV with a temporal distance which is normal distributed with a mean distance of 30 BC and a standard deviation of 10 BC. The second set has energies up to 30 GeV with an fixed gap of 45 BC. This was done to reduce effects of specialization on specific properties of the data. [personal communication, Anne-Sophie Berthold]
However it seems like this was not a sufficient generalization in order to reach performances that are not strongly influenced by the properties of the data used. Figure 2.6 shows that the CNNs struggle for short temporal distances for a data set with normal distributed hits with a mean distance of 30 BC and a standard deviation of 10 BC and energies up to 30 GeV. Even though the training included hits with such a small gap, the CNNs have not learned to correct the energies with short distance events properly at higher energies.
Another example for such a specialization can be seen if the CNNs are evaluated with energies which are higher than the maximal energy in the training data sets. As shown in figure 2.7 the energies reconstructed by the 4Conv network are underestimated for energies above 30 GeV even if the pulse height increases linearly with the energy. Additionally there are a lot of fake energies with very high values for both CNNs. A reason for this might be the non-linearity of the CNNs, especially caused by the sigmoid functions. The CNNs also seem to reconstruct a lot of high fake energies on this evaluation data set while the CNNs will not predict as many high fake energies on data sets with energies known from their training data.

2.3.3 Resources on the FPGA

The CNNs described in [27] have less than 100 parameters which is rather small for modern ANNs. This small amount of parameters is required because the energy reconstruction algorithm needs to run on the LASP FPGA which has limited resources on the one hand and it has to process data from 384 calorimeter cells on the other hand.

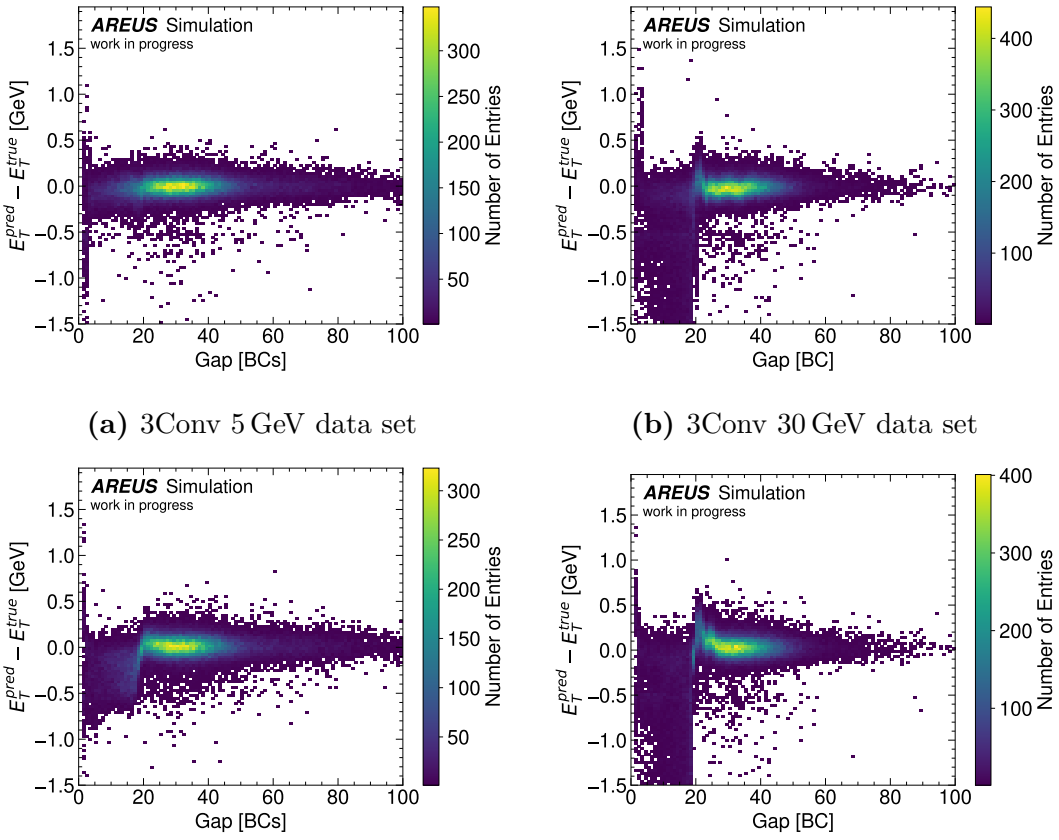

(a) 3Conv 5 GeV data set

(b) 3Conv 30 GeV data set

(c) 4Conv 5 GeV data set

(d) 4Conv 30 GeV data set

Figure 2.6: 2D Histogram of difference between predicted and actual energies over the gap to the previous pulse with an energy above 0.5 GeV for OFMax, 3Conv and 4Conv ANN. All evaluation data sets had normal distributed hits with a mean distance of 30 BC and a standard deviation of 10 BC. The performance of the CNNs drops for small temporal distances when the data contains transverse energies higher than 5 GeV. It seems that the network learned to correct the out-of-time pile-up only for hits below 5 GeV because hits with higher energies only had the constant gaps of 45 BC in the training data set and therefore did not produced out-of-time pileup.

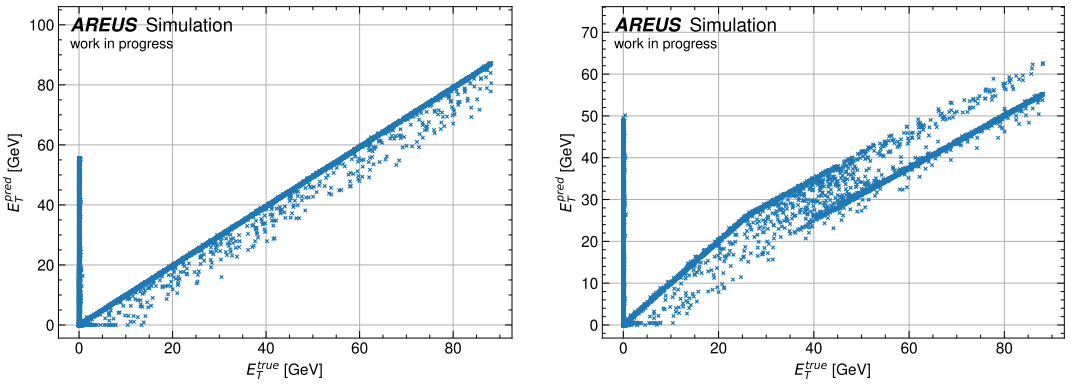

(a) 3Conv **(b)** 4Conv

Figure 2.7: Predicted energy over actual energies for 3Conv and 4Conv CNNs. Both networks were trained with data which included energies up to 30 GeV. A lot of high fake energies and a systematical underestimation of transverse energies > 30 GeV are observable.

A smart implementation of the CNNs on the FPGA can save resources but the possible saving here is limited. The CNNs themselves are either more resource efficient if they have fewer parameters or the calculations and operations are easier to handle for the FPGA.
The implementation of the CNNs on hardware on the FPGA is complicated. Resource-saving network architectures would help to make the implementation easier and less prone to errors.

2.3.4 Unknown Influence of varying Pulse Shapes

The specialization of the CNNs leads to the question how stable the networks perform if the pulse shapes vary due to different reasons. One reason is that the actual pulse shape caused by the shaping electronics may fluctuate due to small differences in the electronics and cell geometry. But also the ideal pulse shape varies in different detector regions. Additionally, the pileup in different η-regions will vary, which leads to different noise patterns.
While this variation is known in principle and the CNNs can be trained individually for every cell, there are other variations which are not predictable. One example is the influence of time shifts of the pulses relative to the sampling clock which is described in detail in section 4.1.

All expected and realistic shape variations as possible should be checked because it is important that the ANNs have a low rate of fake energies, efficiently detect the signals and reconstruct the peak of each pulse in the correct bunch crossing.

2.3.5 Trainings getting stuck in local Minima

Some trainings will minimize the loss in the way that it finds a local minimum which is very undesirable. An example is a network which sets all output values close to zero. Since most of the data points in the simulated sequences have no or very low energy entries, setting all predicted values close to zero results in a better loss than reconstructing fake energies too often.
Such a minimum is found quite often depending on hyper-parameters like the initializer or the learning rate. It is therefore desired that the training process is set up in a way that local minima are avoided for a majority of the network trainings.

3 Optimization of the CNN Architecture and Training Structure

In this work, new features of the CNNs, that are implemented to improve the energy reconstruction, were always chosen such that they maintain or even reduce the FPGA resource consumption of the CNNs. To get a starting point for the search for alternative architectures, resource-saving networks were analyzed and then their performance and reproducibility was compared to the 3Conv and 4Conv CNNs.
Another method to increase the performance and reproducibility of the CNNs is to test different loss functions. Loss functions highly influence the results of a training but they do not affect the architecture and resource consumption in the hardware implementation. The impact of customized loss functions on the performance and reproducibility is evaluated.

3.1 Usage of Callbacks

During a training, the Python framework Keras allows checking properties of the current parameters. An automatic reduction of the learning rate at a loss plateau are already implemented in Keras and used to train the CNNs.
Additional callbacks can help to reduce the number of trainings which end in unwanted local minima. During the work for this thesis, a callback was implemented which resets the parameters with normal distributed values if an adjustable loss limit was not reached after a specific number of steps.
Using this callback, not a single training resulted in the case where for all bunch

crossings energies close to 0 were reconstructed.

3.2 An Alternative Activation Function: COReLU

One property of the current CNNs that consumes many resources on the FPGA is the sigmoid activation function. Since FPGAs can only perform basic calculations, the division and exponential function in the definition of the sigmoid is too complex for a direct calculation. Therefore the sigmoid gets approximated on the FPGA by using a specific number of linear segments or by using a look-up table. The better the approximation should be, the more segments and thus resources on the FPGA are needed.
Replacing the sigmoid function with simpler activation functions, which fit to the tagging problem, could improve the resource consumption. Therefore, two conditions should be met. At first, the function should be simple, in the best case segmentally linear and additionally it should only return values between 0 and 1. One of the simplest functions that meets these two conditions is a function which is defined as:

$$\alpha(x) = \begin{cases} 0 & \text{if } x < 0 \\ x & \text{if } 0 < x < 1 \\ 1 & \text{otherwise} \end{cases} \tag{3.1}$$

This function is basically a ReLU function that is cut off for values above 1, which is why this activation will be called Cut Off ReLU (COReLU) here.
The COReLU activation was tested with the 3Conv CNN that was modified in the following way. The sigmoid activation in the first layer of the tagging part was replaced by a ReLU function and in the second layer it was replaced by the COReLU function. Additionally, all initializers were replaced by the He Normal function [20]. This initializer produces normal distributed weights with a mean of 0 and a standard deviation of $\sigma = \sqrt{\frac{2}{n_l}}$ where n_l is the number of parameters in the layer. The number of weights reduces the standard deviation and therefore keeps the expected value of the sum of the products of the weights in this layer nearly to 1. Hence this distribution prevents a strong amplification or reduction of the input when many parameters are used to calculated the output of the layer with ReLU activation functions. This should ensure a nearly linear calculation

which is desirable in the case studied here.
To check if this simplification has a negative influence on the performance of the 3Conv CNN, the 3Conv network with the COReLU function was also trained 100 times the same way as in [27]. Just like the self-trained 3Conv network, the 3Conv network with a COReLU activation produced no result which is as good as the 3Conv network from [27] and only 5 trainings performed better or at least as well as the Optimal Filter regarding the energy resolution. For the self trained 3Conv network 6 of these 100 trainings performed that well.
In figure 3.1 and 3.2 the best performing self trained 3Conv network and 3Conv network with a COReLU activation are compared. The histogram of energy differences in figure 3.1 and also the 2D histograms in figure 3.2 depending on the gap between two pulses are analyzed. For both performance indicators, the CNNs perform very similar.
Another observation is that more trainings resulted in much broader energy difference distributions compared to the normal 3Conv network trainings. Those trainings with broader energy resolutions than the OF will be thrown away anyway. Therefore, how broad the energy difference distributions of these trainings is, is not that important. Still the higher fluctuation of the performance should be kept in mind. A reason for this could be the vanishing gradient problem [30, Chapter 8] since the gradient of the COReLU function is 0 for most x. This may increase the chance for very badly performing trainings.
All in all the COReLU activation has no significant negative influence on the performance of the 3Conv network when well working trainings are compared despite simplifying the activation significantly. Also the number of well performing trainings does not seem to be reduced. Still 95 % of the trainings of the 3Conv network with the COReLU and 94 % of the trainings of the 3Conv network with sigmoid activation had a worse energy resolution than the OFMax. The reproducibility of well performing trainings must be increased. It should be mentioned that this activation has not been tested yet on the FPGA but only in Python software and in the next step it should be tested on hardware to validate how much this function really improves the FPGA resource consumption.

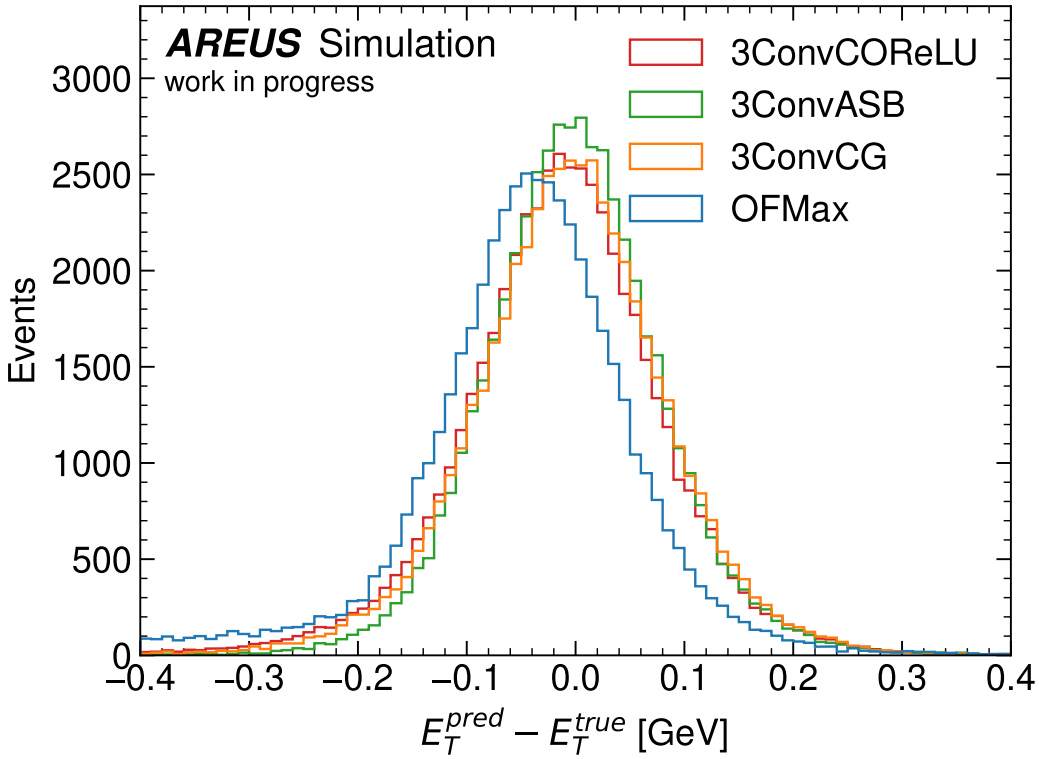

Figure 3.1: Comparison of the difference between predicted and actual energies for different networks. 3ConvCG is the 3Conv network trained during this work, 3ConvASB is the 3Conv network from [27]. Since these two CNNs have the same architecture and were trained the same way, in principle they should perform the same way if the same minimum was found during the training. Only energy deposits above 1 GeV are included. The 3Conv network with a COReLU activation and the 3Conv network which was trained for this work have a comparable performance. Both outperform the OFMax but do not reach the performance of the 3Conv from [27]. For the self-trained 3Conv network, this means no training of the 100 exectutes trainings ended in the same minimum as the 3Conv network from [27].

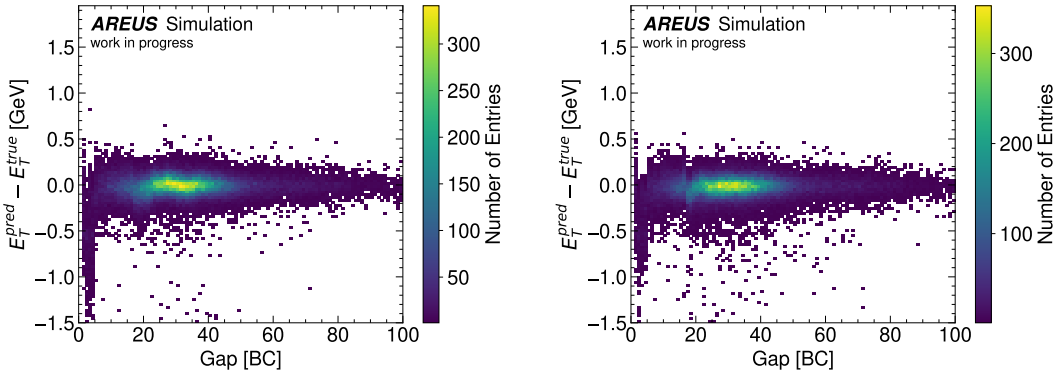

(a) 3Conv (self trained) **(b)** 3Conv COReLU

Figure 3.2: 2D-Histogram of the difference between predicted and actual energies on the y-axis and the gap between two energy deposits above 0.5 GeV for a self trained 3Conv ANN and the 3Conv with a COReLU activation. Both distributions are very similar which indicates that the simplifying COReLU function does not negatively influence the performance of the 3Conv ANN.

3.3 Alternative Loss Functions

Using other loss functions could improve the results of the training. So far the mean absolute error and mean squared error were studied. The comparison of these two loss functions shows that the MSE produces broader energy difference distributions compared to the MAE.

The reason for this effect could be explained by the geometry of the functions. Outliers influence the value of the MSE much more than data points where the difference is already small. Optimizing the weights of the CNN in that way that outliers are reconstructed slightly better will reduce the loss more than optimizing data points where the difference is already small. To get more narrow distributions of the energy deviation, a reversed geometry could be desirable: a function which has a higher gradient for small energy difference than for bigger ones.

A first idea that fulfills this attribute would be a mean root absolute error (MRAE):

$$MRAE = \frac{1}{N}\sum_{i=0}^{N}\sqrt{|y_{\text{true},i} - y_{\text{pred},i}|}. \tag{3.2}$$

This function would be a rather simple loss function but has a divergent gradient if $y_{\text{true},i} - y_{\text{pred},i} \to 0$. This is a massive disadvantage because the training step

size will diverge too, leading to problems while searching for minima.

A more fitting albeit more complex loss function would be a mean hyperbolic tangent linear loss (THL):

$$THL = \frac{1}{N}\sum_{i=0}^{N} \left|\tanh\left(y_{\text{true},i} - y_{\text{pred},i}\right) + y_{\text{true},i} - y_{\text{pred},i}\right|, \tag{3.3}$$

which is nearly linear for greater energy deviations with a slope of ± 1 for a single data point and a maximal slope of ± 2 if the energy difference is nearly 0.

To test the influence of this loss on the training performance again 100 3Conv and 3Conv COReLU networks were trained using the THL as the loss function for the energy reconstruction training. Again the energy resolution for hits with energies higher than 1 GeV were analyzed. For the 3Conv CNN trained with THL only 3 trainings performed at least as well as the OFMax while for the 3Conv COReLU CNN 7 performed similar or better than the OFMax. One training even performed similar to the 3Conv network from [27]. The respective best trainings are shown in figure 3.3 and 3.4.

While single performances do not allow a general and statistically significant conclusion on which architectures and training methods work better and produce well performing trainings more often, the number of these well performing trainings shows a trend. The best training performance from all self trained CNNs is the 3Conv COReLU network with THL loss. This might be coincidence but this architecture also produced the largest number of trainings with a better energy resolution than the OF. Still this result should be checked.

To verify this assumption the performance was tested the same way with a simplified setup where only one data set was used to train the model. The data contains hits up to 30 GeV and gaussian distributed gaps with $\mu = 30\,\text{BC}$ and $\sigma = 10\,\text{BC}$. The CNNs were evaluated on another data set with the same properties. The 3Conv network performance dropped significantly. Not a single of the 100 trained CNNs performed comparable with the OFMax in terms of the energy resolution. Also THL loss function did not improve the performance significantly. While the mean performance for the 3Conv network with a COReLU function was slightly better, also none of the trainings outperformed the OFMax. For this CNN architecture, the trainings using the THL seem to increase the performance since

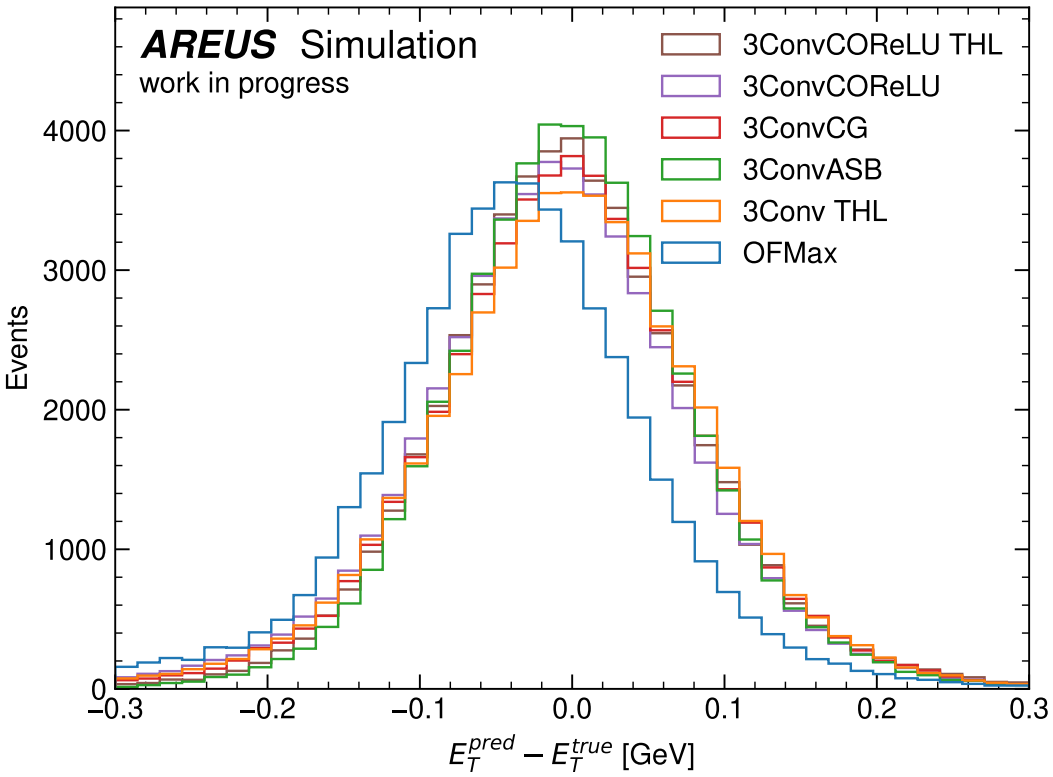

Figure 3.3: Comparison of the difference between predicted and actual energies for different networks. 3ConvCG is the 3Conv network trained during this work, 3ConvASB is the 3Conv network from [27]. The two CNNs have the same architecture and training structure and should therefore lead to the same results if the same minimum was found during the training. The additional label THL indicates if the THL loss function was used. No extra label means that the CNN was trained with MAE Only energy deposits above 1 GeV are included. Still the 3Conv network from [27] has the best energy resolution but the 3Conv COReLU network trained with THL outperforms all other algorithms.

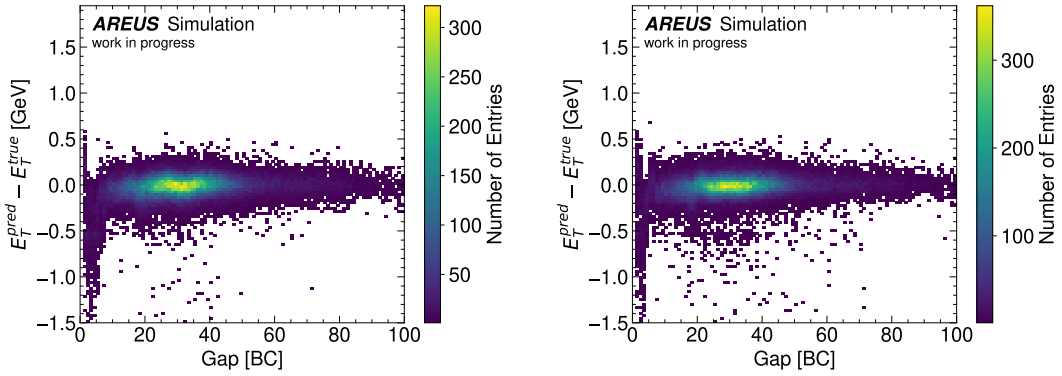

(a) 3Conv THL **(b)** 3Conv COReLU THL

Figure 3.4: 2D-Histogram of the difference between predicted and actual energies on the y-axis and the gap between two energy deposits above 0.5 GeV for a self trained 3Conv ANN and the 3Conv network with a COReLU activation with the THL loss function. The THL could not improve the resolution for the 3Conv network with a sigmoid activation but for the network containing the COReLU, the results were improved.

2 trainings produced results comparable with the OFMax. Figure 3.5 shows the best trainings for this setup.

In both setups the THL could not increase the performance for the trainings of the 3Conv network but the 3Conv COReLU network was influenced positively by this loss function. For the second setup the THL seems to reduce the performance of the 3Conv network with sigmoid activation functions.

Also some other loss functions were tested. For example the Huber loss [29] or a MAE where every data point is weighted with weights defined by the temporal distance to its preceding high energy pulse. However, these loss function did not show an increased performance.

All in all it can be seen that the choice of the loss function is important for the reproducibility of the performance of ANNs. Since the THL seems to help the 3Conv network with the COReLU activation but not the 3Conv network with sigmoid, different loss function should be tested if the CNN architecture is changed.

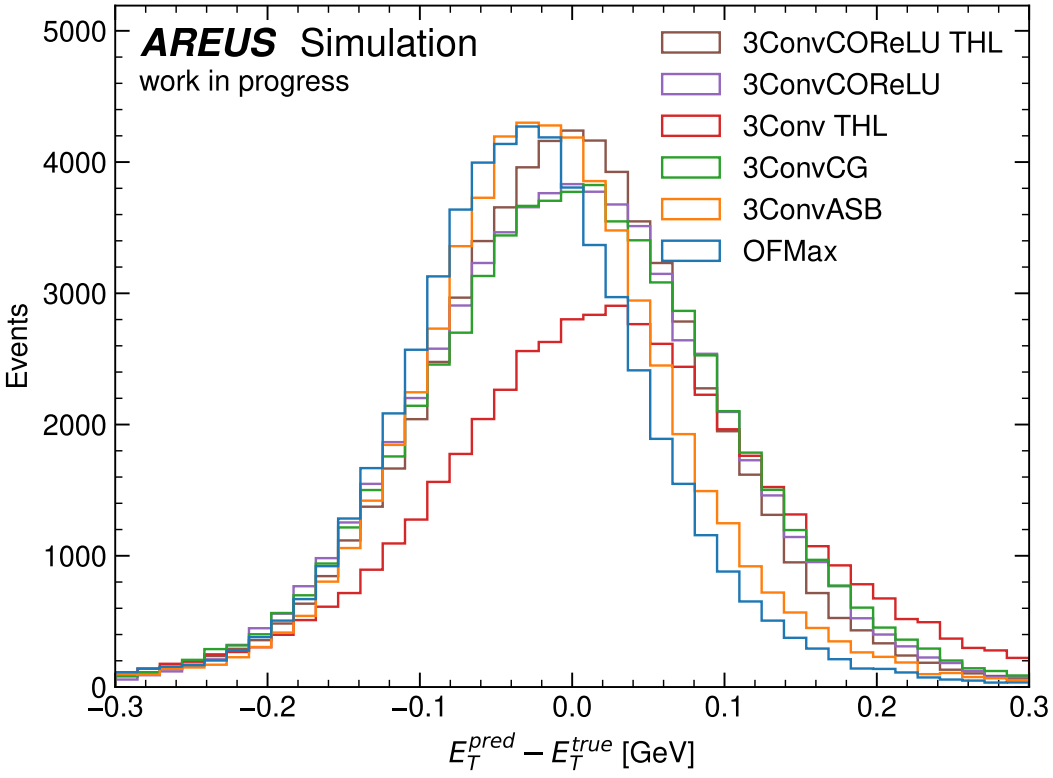

Figure 3.5: Comparison of the difference between predicted and actual energies for different networks evaluated on a 30 GeV data set. 3ConvCG is the 3Conv network trained on a 30 GeV data set, 3ConvASB is the 3Conv network from [27]. The additional label THL indicates if the THL loss function was used. No extra label means that the CNN was trained with MAE. Only energy deposits above 1 GeV are included. Again the best working algorithm is the legacy 3Conv network but like in the previous setup, the combination of COReLU and THL performs better than all other algorithms.

3.4 CNNs without Tagging

Even more resource-saving than simple replacements for the sigmoid would be a CNN without the tagging layers, where all layers use ReLU functions as activation. This should also be optimal for the energy reconstruction since the ReLU function is the natural candidate for this task because it is nearly linear and does not allow the reconstruction of negative energies.

Methods to train CNNs without the tagging sub-network were studied during this work. This might allow to check if the fake energy reconstruction and non-linear hit energy reconstruction, which was observed when the evaluation data contained greater energies than the maximal energy of the training data, can be solved if no highly non-linear sigmoid functions is used. Therefore a CNN with 3 layers was created. The first layer has 5 filters and a kernel size of 3, the second layer got 2 filters and also a kernel size of 3. The last layer has 1 filter and a kernel size of 21. These parameters are mainly taken over from the legacy 3Conv network architecture. The only differences are, that 2 filters instead of 1 were used in the second layer, the concatenation layer is discarded and the kernel size of the second layer was reduced to 3 to match the number of parameters. This results in a total parameter number of 95 which is just 1 more than the 3Conv network from [27]. Since all layers have ReLU functions as their activation, this CNN should be much more resource-saving than the 3Conv network. A scheme of this CNN is shown in figure 3.6.

For such a CNN the training structure must be modified because the pre-training with the tagging part is no longer needed. Since one open question is the required size of the training data, more data sequences were used to improve the training. While the previously used training data contained 400 sequences with 10 000 BC each, the new training data set contained 12.5 times more sequences and the data had more variation. The following sequences contained 10 000 BC each:

1. 2000 sequences with hits up to 30 GeV and 45 BC between two hits with realistic time shifts

2. 2400 sequences with hits up to 30 GeV and a gaussian random gap with $\mu = 30$ BC and $\sigma = 10$ BC between two hits with realistic time shifts

3. 200 sequences with hits up to 30 GeV and a gaussian random gap with $\mu = 30\,\mathrm{BC}$ and $\sigma = 10\,\mathrm{BC}$ between two hits with enlarged time shifts

4. 200 sequences with hits up to 5 GeV and a gaussian random gap with $\mu = 30\,\mathrm{BC}$ and $\sigma = 10\,\mathrm{BC}$ between two hits with realistic time shift

5. 200 sequences without artificially added hits with realistic time shift

The meaning of realistic and enlarged time shifts will be explained in the next chapter but is mentioned here for completeness. These data sets were chosen such that the data contain some variation but the exact composition of specific properties were randomly chosen. The only reason for this choice was the idea to use different maximal energies, temporal distances of hits and time shifts. There may be more optimal choices how often specific properties of the data should appear.
The CNN was trained with the mean absolute error. Other loss functions were tested briefly but did not lead to better results. Because of the larger number of data points one epoch needs much more time for this training setup but less epochs are needed to reach a loss plateau. Instead of 300 tagging training epochs and 300 epochs in the energy reconstruction training only 100 epochs were needed to reach good results.
To check the reproducibility, again multiple trainings were executed. Instead of 100 trainings, only 50 trainings were done. Again these networks were evaluated on the same data set as in the previously presented evaluations. 13 networks, 26 % of the trainings, achieved results comparable with or better than the OF and additional 6 trainings, correspondingly 12 %, performed comparable with the 3Conv network from [27]. Despite having only half of the trainings, more results with good and very good energy resolutions were achieved than for any other architecture. To check if this effect is only caused by the different training data set or by the architecture, the 3Conv network was also trained 50 times with the same training data. 5 of the trainings, so 10 %, performed similar or better than the OFMax, no training reached the performance of the 3Conv network from [27], which means that the percentage of these trainings is better than for the previous training method. Still, the performance of the 3Conv network without tagging

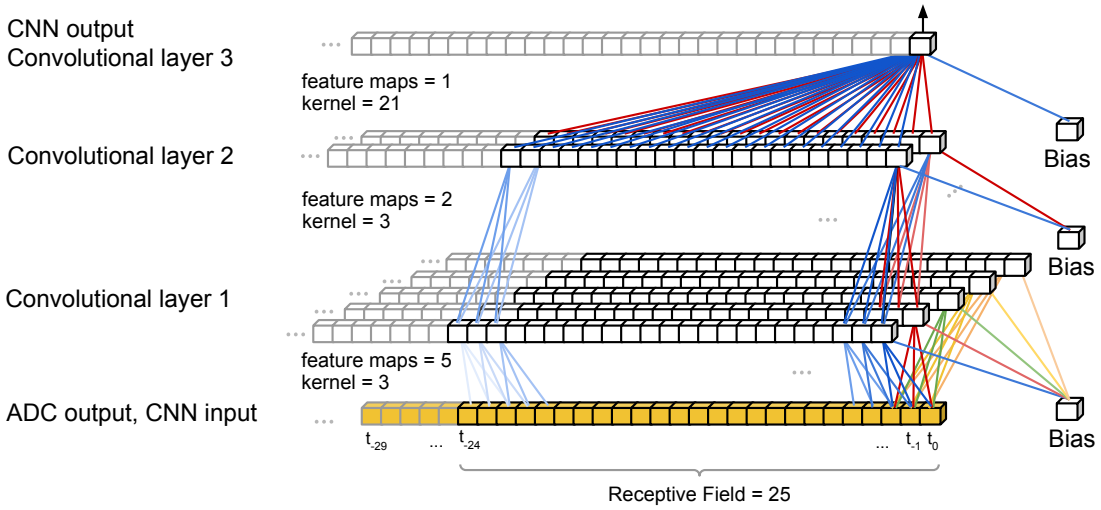

Figure 3.6: Scheme of the 3Conv network without tagging part. The first layer has 5 filters and a kernel size of 3, the second layer got 2 filters and also a kernel size of 3. The last layer has 1 filter and a kernel size of 21. Every layer has a ReLU function as its activation function. This results in a total parameter number of 95 and a receptive field of 25 bunch crossings.

layers seem to have a much better reproducibility. Since this CNN is a promising candidate, some more detailed evaluation will be provided here.

In figure 3.7 the difference between predicted and true energy is shown for different CNN types and the OFMax. One can see that the performance of the 3Conv network without tagging layers is very similar to the 3Conv network and outperforms the other algorithms. Also the best 3Conv network trained with the new training method, denoted with 3ConvNT, could not perform as well as the CNN without tagging layers and the 3Conv network from [27]. Figure 3.8 shows gaussian fits of the peaks in the range where the bins have at least 25 % of the height of the peak. The standard deviation of these fits shows that the 3Conv network without tagging has a better energy resolution than the 3Conv network with tagging but the mean deviates slightly more. The energy resolution of the 3Conv network without tagging is 3 % better than the resolution of the OFMax and 2 % better than the energy resolution of the 3Conv network.

Also the reconstruction of fake energies is similar to the other algorithms as shown in figure 3.9. Especially for small values the OFMax and also the 3Conv network produce less fake energies. In the data set used for evaluation, 353274 of the two

million bunch crossings had a true energy of 0. The OFMax reconstructed fake energies in 4 % of these bunch crossings. The 3Conv network reconstructed energies in 6 % and the 3Conv network without tagging in 8 % of the bunch crossings where the true energy is 0. The maximal fake energy reconstructed by the OFMax has a transverse energy of 4.9 GeV and the maximal fake energy the 3Conv network reconstructed is 3.4 GeV. The maximal fake energy of the 3Conv network without tagging layers is much smaller with 0.8 GeV. These maximal fake energies of the OFMax and the 3Conv network are likely outliers and maybe just actual energy deposits assigned to a neighboring bunch crossing. To cut these outliers, energy intervals that contain 95 % of the fake energies were analyzed. For the 3Conv CNN without tagging layers, 95 % of the fake energies were smaller than 0.14 GeV while for the 3Conv network this is the case for 0.15 GeV. For the OFMax, 95 % of the fake energies were smaller than 0.16 GeV. This shows that most of the fake energies are rather small. The 3Conv network without tagging reconstructed twice as many fake energies than the OFMax in total but only 1.14 times more fake energies larger than 0.1 GeV. The numbers of fake energies for the different algorithms are given in table 3.1.
Figure 3.10 shows the performance of the 3Conv network without tagging depending on the temporal distance between two pulses. While the distribution is narrower and more centered around the horizontal zero line compared to the 3Conv network, there are more entries for gaps below 5 BC. Still this CNN clearly outperforms the OFMax.

Algorithm	$N_{\text{fake energies}}$	$N_{\text{fake energies}}$ $E_T^{\text{pred}} < 0.01\,\text{GeV}$	$N_{\text{fake energies}}$ $E_T^{\text{pred}} > 0.1\,\text{GeV}$
OFMax	13998	1387	2398
3Conv network	19828	3549	2683
3Conv no tagging	28168	5969	2744

Table 3.1: Number of fake energies for the OFMax, the 3Conv network and the 3Conv network without tagging. The data set contains 2000000 bunch crossings and 353274 of these bunch crossing had no energy deposit. the 3Conv network without tagging produces more than twice as many fake energies than the OFMax and more than 40 % more fake energies than the 3Conv network with tagging. Most of these fake energies have rather small values.

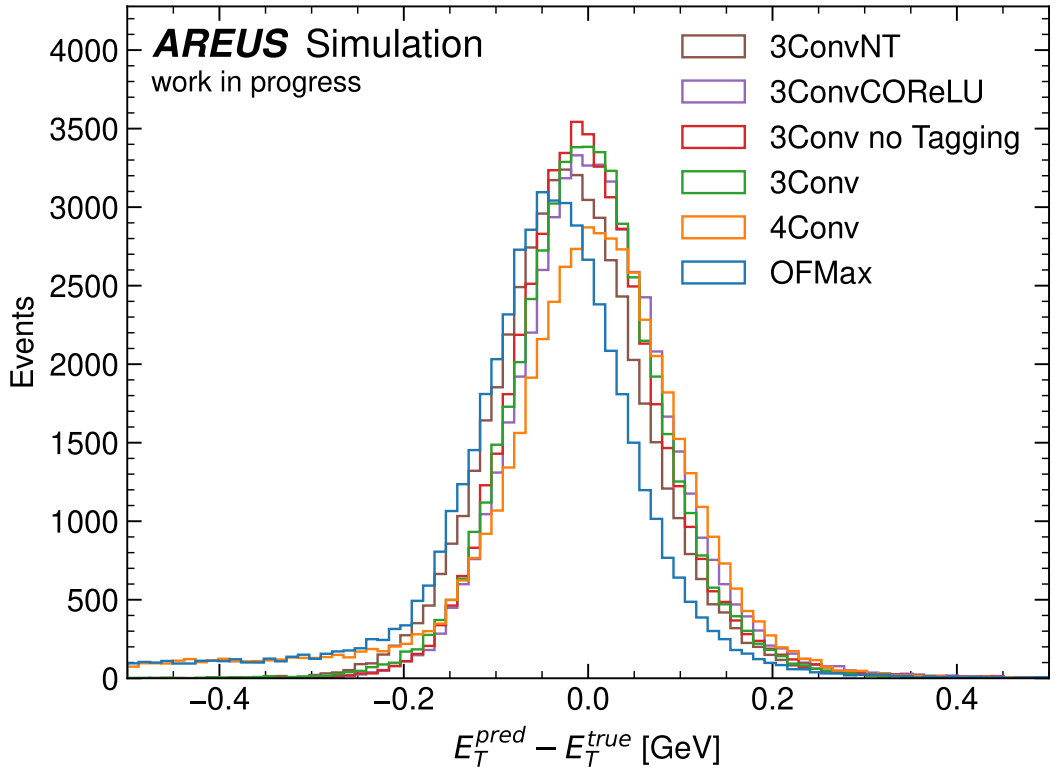

Figure 3.7: Histogram of the energy differences between predicted and true energies for different CNNs and the OFMax. Only Pulses with a transverse energy above 1 GeV are included. The energy difference distribution of the 3Conv network without tagging layers is more narrow than for all other algorithms and therefore outperforms them in this category.

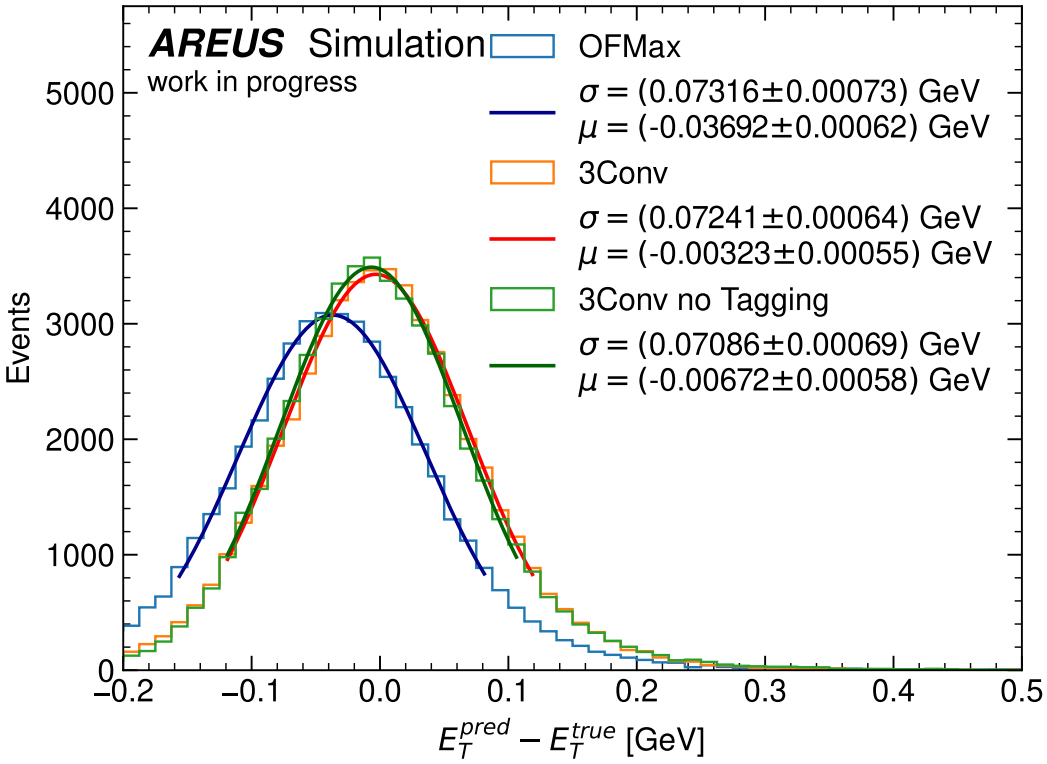

Figure 3.8: Histogram of the energy differences between predicted and true energies for different CNNs and the OFMax. Only Pulses with a transverse energy above 1 GeV are included. The energy difference distribution of the 3Conv network without tagging layers is more narrow than for the 3Conv network and OFMax. The fits include those bins which are filled with at least 25 % of the entries at its peak. The standard deviation of the 3Conv network without tagging is the smallest one but the mean deviates slightly more than for the 3Conv network.

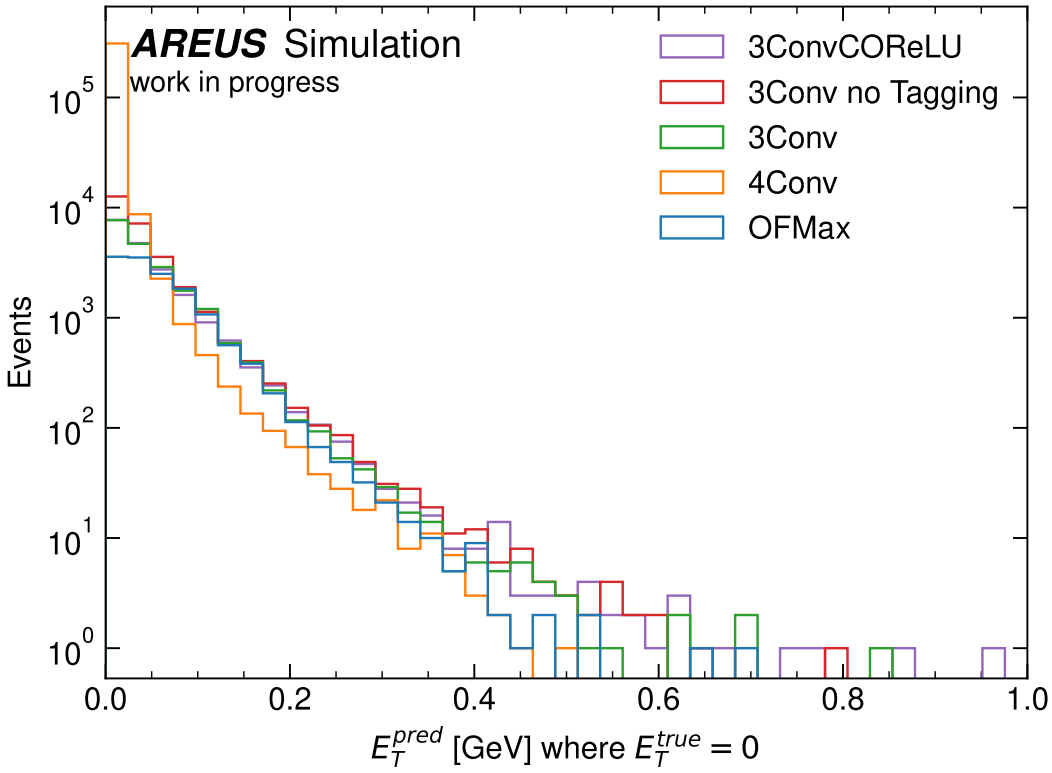

Figure 3.9: Histogram of the reconstructed fake energies for different CNNs and the OFMax. No big differences between the algorithms besides the 4Conv network are visible.

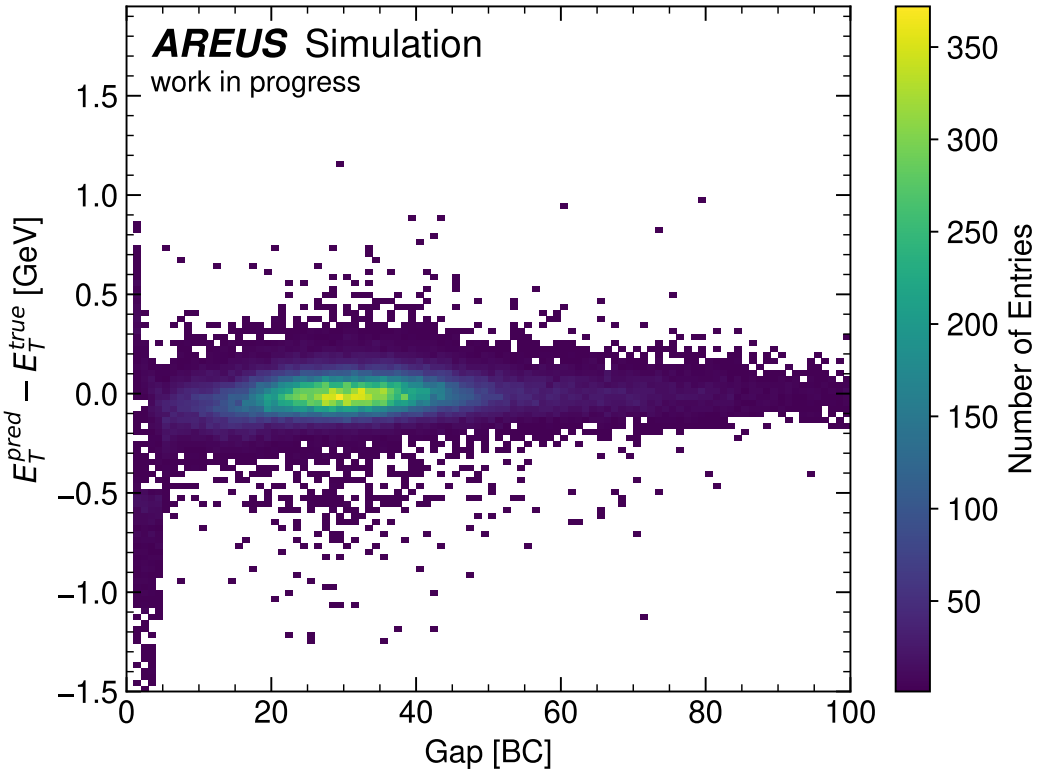

Figure 3.10: 2D-Histogram of the difference between predicted and actual energies on the y-axis and the gap between two energy deposits above 0.5 GeV for the 3Conv network without tagging layers. There are some more entries for gaps smaller than 5 BC compared to the legacy 3Conv network but it cleary outperforms the OFMax.

Since the fake energies shown in figure 3.9 only indicate how well the background rejection works, a way to evaluate the signal detection is needed. Analyzing data points with $E_T^{\text{true}} > 0\,\text{GeV}$ and $E_T^{\text{pred}} = 0$ would not lead to useful results because reconstructing a 1 GeV energy deposit with 0.01 GeV can be handled as a signal rejection but could not be seen in such an evaluation. A better way is to look at the relative deviation of the reconstructed energy for different energy ranges. An relative deviation of -1 occurs if no energy was reconstructed, relative deviations near that value can be interpreted as signal rejection. Figure 3.11 shows the mean and median of the relative deviation and the ranges where 68 % and 95 % of the relative deviations are included for different energy regions for the OFMax, 3Conv network, 4Conv network and 3Conv network without the tagging part. The 4Conv network has some interesting effects for small energies which was already observed at the fake energy reconstruction. It seems to reconstruct very few bunch crossings with 0 energy. For higher energies the relative deviation is higher than it is for the 3Conv network with and without tagging layers and comparable to the OF. The 3Conv network and 3Conv network without tagging layers have very similar median and mean values. A difference is visible for the lower range of the 95 % interval, where the 3Conv network without tagging seem to reject more signals above 0.7 GeV. Still both CNNs outperform the OFMax.

One assumption which was made is that the non-linearity of the sigmoid function leads to problems when the energy of a pulse is greater than the highest energy of the training data. To verify this, the 3Conv network without tagging layer and a 3Conv network with tagging trained using the new training method are evaluated on a data set containing higher energies up to 90 GeV. The predicted energy over the true energy is shown in figure 3.12. The energy resolution of the best 3Conv network trained with the new data set is not as good as the 3Conv network from [27] and the 3Conv without tagging part, so their comparison is biased. Still, it is visible that the 3Conv CNN trained on the new data set reconstructs a large amount of fake energies such as the legacy 3Conv network does. The 3Conv network without tagging does not have this problem.

During the evaluation of the performance of this CNN, some deviations in the training data were found. The ideal pulse shape and the noise distribution vary slightly for different data sets. Further information will be provided in section 4.2. However, the results of the 3Conv without tagging are not less good because of

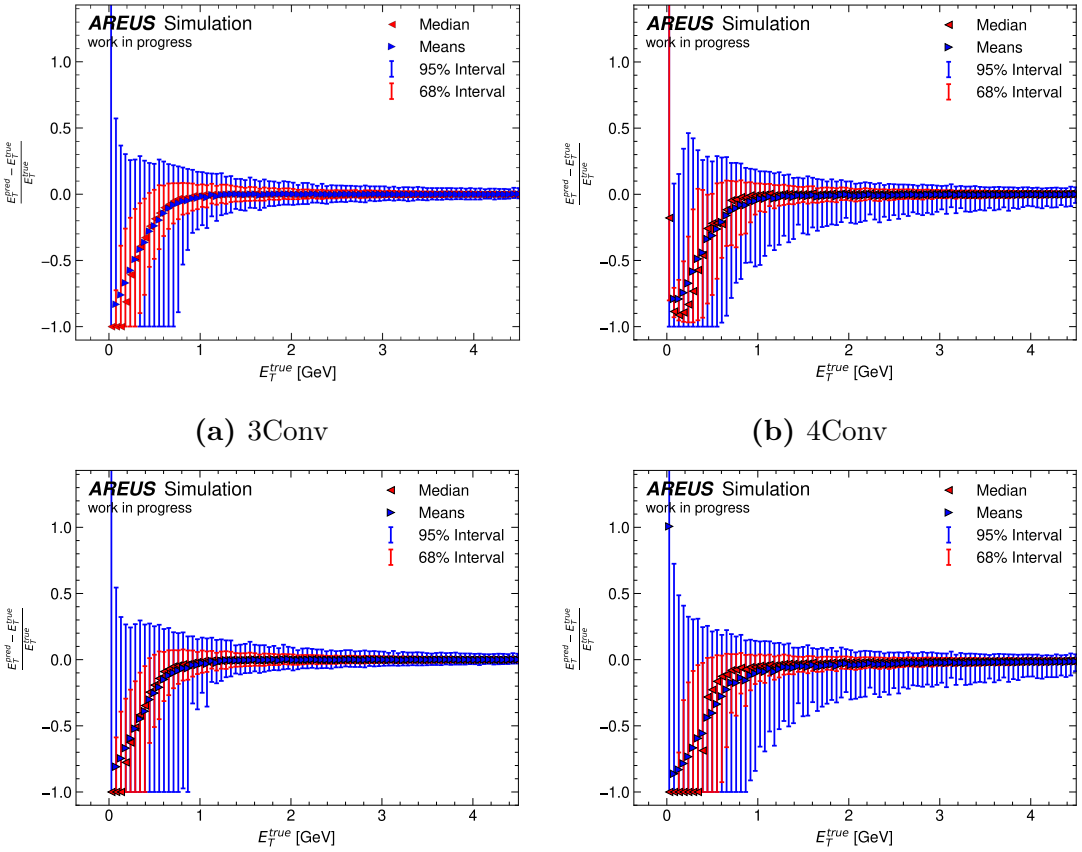

(a) 3Conv

(b) 4Conv

(c) 3Conv without Tagging

(d) OFMax

Figure 3.11: Plot of the mean and median of the relative deviation as well as the ranges where 68 % and 95 % of the relative deviations are included for different energy regions. The intervals reaching to an relative deviation of -1 indicate that the algorithms reject signals. The 3Conv network without tagging seem to reject some more signals than the legacy 3Conv but less than the OFMax.

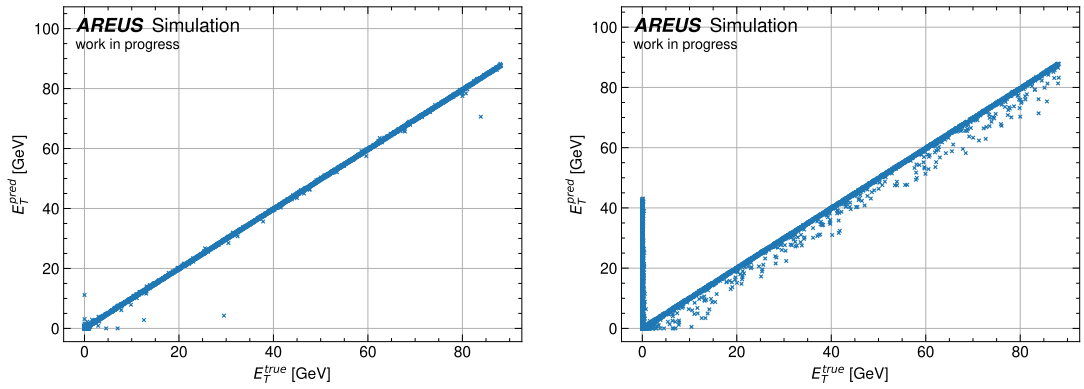

(a) 3Conv without tagging **(b)** 3ConvNT

Figure 3.12: Predicted energy over true energies for 3Conv network without tagging and the 3Conv network with tagging, which was trained on the large data set and is denoted here as 3ConvNT. Both networks were trained with data which included energies up to 30 GeV. While the 3Conv without tagging layer handles energies higher than 30 GeV well the 3Conv with tagging layers produce a lot of high fake energies even with the new training method.

these variations in the data. Since the CNN without tagging performs better on the data containing the previous noise pattern and pulse shapes as well as on the new data with variations, this indicates that the CNN is more robust against small variation in the data, especially the exact pulse shape. Still, the training should be repeated with data sets containing the correct pulse shapes and its robustness should be proved afterwards.

A 4Conv CNN without tagging layer was not tested mainly because of two reasons. On the one hand, the 4Conv with tagging layer performed worse than the 3Conv, so the focus was to develop optimizations of the 3Conv CNN. On the other hand, the 3 layer structure has another motivation. The first layer splits into many feature maps to allow the CNN to filtering different features of the data. If every feature map would be evaluated with the output layer with a kernel size of 21, many parameters would be needed. Therefore the second layer decreases the number of filters and so the number of parameters for the last layer.

4 The Influence of varying Pulse Shapes

4.1 Sources of Time Shifts of Pulses

Ideally, every particle would hit the calorimeter cell in a way that the maximum of the pulse's peak is synchronized with the sampling rate of the ADC, which is in turn with the bunch crossings of the LHC. Due to different times of flight and collision vertex variation, the hit can happen later or earlier than the exact bunch crossing when both bunches overlap completely.

The first source for time shifted pulses is the interaction with the detector material. These hit times are already included in AREUS assuming that every collision happens at the exact IP at the nominal time of a bunch crossing and the resulting particles will reach the detector cell with the speed of light. Since interactions with the detector material can only slow down these particles, this effect results in positive time shifts . Here, positive means that the hit is delayed to later times. While measuring hits at ATLAS these shifts are unknown but relatively small. A simulated test sequence for a cell in the middle layer of the EMB including just these time shifts has a mean time shift of $\bar{\tau} = 0.125\,\text{ns}$, so just $0.5\,\%$ of a bunch crossing time interval, and a maximum of $\tau_{\text{max}} = 0.42\,\text{ns}$ or correspondingly $1.7\,\%$ of a bunch crossing time interval.

The geometry of the bunches causes two more types of time shifts. If the bunches were just point-like, every proton-proton-collision would occur at $z = 0$ and at the exact bunch crossing time. The time of flight of the particle to the cell causes shifts which can be partially corrected before sampling. Then only the random shifts described in the previous paragraph would occur significantly.

In reality the protons in a bunch at the LHC and HL-LHC are gaussian distributed

in every space direction. The radial distribution is negligible small in the order of μm, while the length in z-direction is in the order cm and actually influences the time shifts noticeably. This z-distribution has a standard deviation σ_z and a mean μ_z which changes over time. The exact value of the standard deviation which is given in literature varies but values between $\sigma_z = 1\,\text{cm}$ and $\sigma_z = 7.5\,\text{cm}$ are commonly used [36]. Here, data with $\sigma_z = 5\,\text{cm}$ [36] and $\sigma_z = 3.8\,\text{cm}$ [22] was used for evaluation.

The sources of time shifts caused by the bunch geometry is shown in figure 4.2. The first pp-collision can take place before the nominal bunch crossing time. Since the density of protons is smaller in outer regions of the bunch, collisions happen less often there than for times, where the overlap of both bunches is larger. The time shifts caused by this effect are also modelled as gaussian distributed random times with:

$$\mu_{\tau,\text{collision time}} = 0 \qquad \text{and} \qquad \sigma_{\tau,\text{collision time}} = 2\frac{\sigma_z}{c}, \tag{4.1}$$

where c is the speed of light, which is approximately the speed of the protons at the LHC. The resulting distribution is a combination of two independent gaussians and will have an enlarged standard deviation. The factor 2 is an upper limit for this enlargement. This upper limit was chosen such that the training of the CNNs include every possible time shift.

Additionally, an unknown time shift due to different time of flights caused by different z-positions of the collision influences the total time shift. This hit time component is also random but not gaussian distributed for every cell position. For example cells at $\eta = 0$ only have positive time shifts, while for $\eta = \pm\infty$ the times are gaussian distributed. The randomness is caused by the gaussian distributed z-position of the collision with:

$$\mu_{z,\text{collision}} = 0 \qquad \text{and} \qquad \sigma_{z,\text{collision}} = \sqrt{2}\sigma_z \tag{4.2}$$

The factor $\sqrt{2}$ in the standard deviation is caused by the convolution of the two gaussian distributed bunches [4]. The time shift can then be calculated geometrically:

$$\tau_{\text{time of flight}} = \frac{\sqrt{r^2 + z^2_{\text{collision}} + 2rz_{\text{collision}}\cos\Theta} - r}{c} \tag{4.3}$$

where $z_{\text{collision}}$ is the random z-coordinate of the collision, r is the distance between IP and cell and $\Theta = 2\arctan(e^{-\eta})$ is the angle between beam pipe and the calorimeter cell around the interaction point. A scheme of this geometrical consideration is shown in figure 4.1

In reality these two distributions are not independent. Large values for $|z_{\text{collision}}|$ are less likely for high $|t_{\text{collision}}|$. Correct dependent distributions would result in a narrower distribution. Assuming independent distributions, for $\sigma_z = 5\,\text{cm}$, time shifts up to $\tau = \pm 1\,\text{ns}$ are common values.

Other effects can influence the time shifts of pulses further. Some theories beyond the standard model postulate the possibility of unknown long living particles (LLP) which could cause much greater time shifts than those caused by the bunch geometry and particle interaction with the detector. Such particles are currently searched for at ATLAS [14] where lifetimes up to 30 ns are investigated, which would dominate the expected time shifts.

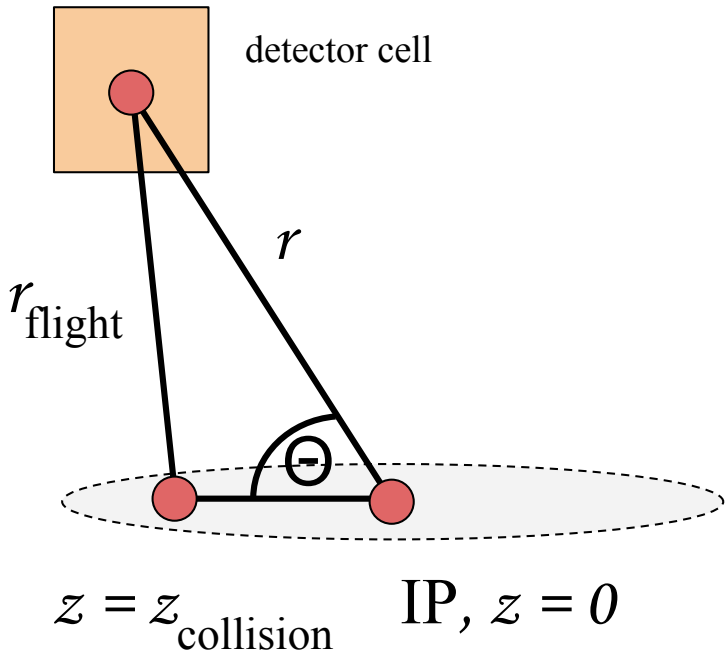

Figure 4.1: Scheme of the geometrical consideration leading to equation 4.3. To calculate the additional hit time, the difference between the flight distance r_{flight} and the distance r between the interaction point and the detector cell is used. r_{flight} can be calculated using the law of cosine if r, $z_{\text{collision}}$ and Θ is known. The hit time is than calculated by subtracting r_{flight} and r and dividing by the velocity of the particle, here approximated with the speed of light c. The scheme is not drawn in scale.

.

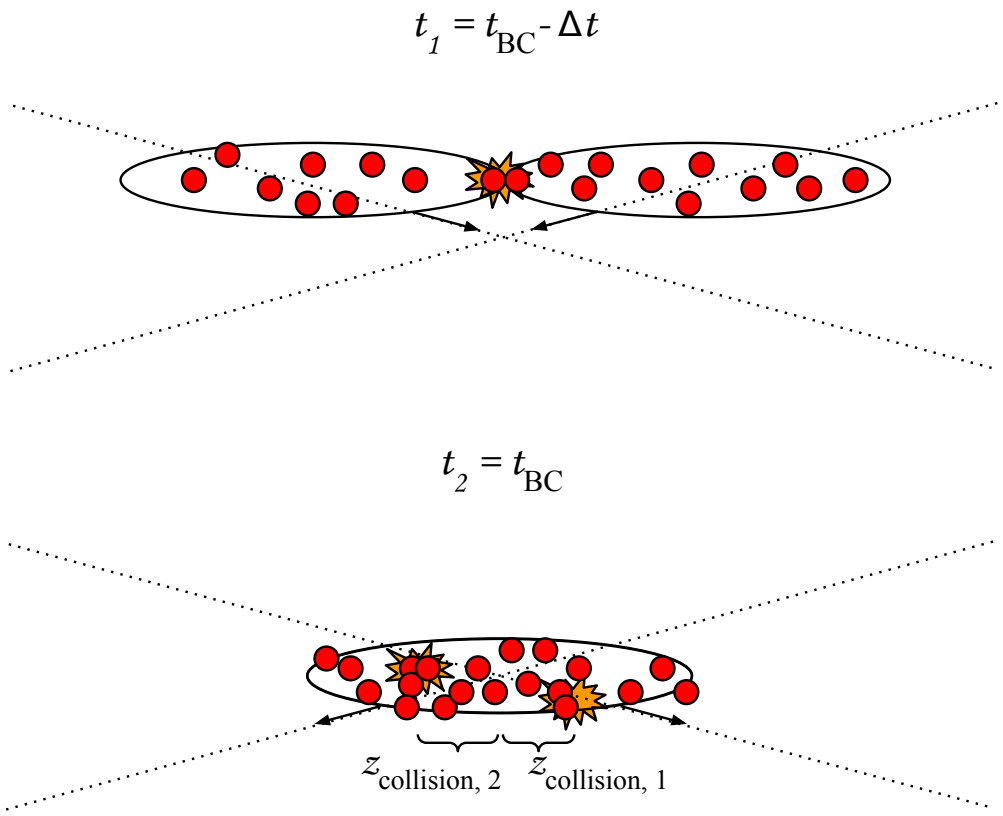

Figure 4.2: Schematic visualization of the crossing of a two bunches. The collision at t_1 shows the first collision of two protons of these bunches happening before the exact bunch crossing at time t_2 when both bunches overlap exactly and their mean is at $z = 0$. At the time t_2 two collisions happen at different z-coordinates.

4.2 Implementation of Time Shifts in AREUS

Since hit times in general are implemented in AREUS, the addition of realistic hit times caused by the bunch geometry is rather simple. For every hit a random z-position and $t_{\text{collision}}$ is generated using gaussian distributed random numbers as defined in the last section and the described calculations are performed to get time shifts. The hits from one bunch crossing are causing single pulses which are shifted individually before sampling. For the output of the hit time sequence, AREUS adds all hit times of the hits from one bunch crossing and weights them by the hit energy.

After implementing these time shifts the generated sequences were analyzed. A Python script was used to check if the AREUS implementation works like expected, which is shown in figure 4.3. For this Python simulation 140 *pp*-collisions were simulated where every collision has a defined probability to hit the cell. This probability was chosen so that the hits-per-BC distribution is the same as in AREUS. Also, the energy distribution of these hits is the same as in AREUS, so the weighted sum of all hits is comparable. It can be seen that under these conditions the hit time distributions of AREUS and the Python model agree sufficiently well. That shows that the implementation works as expected.

While checking the data it was also observed that the time shifts of the pulses are discrete with 0.5 ns steps as shown in figure 4.4. For a better analysis of the influence of small time shifts and the reconstruction of time shifts, a higher temporal resolution of the pulses is needed. This resolution is expressed by more data points of the unsampled pulse curve. In AREUS this number of points is defined by the time between two points of the pulse curve before sampling. This time is determined by a constant, which is set to 0.5 ns. A non-zero hit time will shift the pulse before sampling. Therefore this constant defines the lower limit of the resolvable shifts. It was redefined as 0.005 ns because at this point, no discrete effects were visible in the analysis anymore. To ensure that the pulse shapes are sufficiently well known for small shifts, also the number of data points of the unshaped pulse curves was increased to 10000 sampling points per BC. Since the pulse shapes loaded from the database contain less data points per BC, these pulse shapes are interpolated. The interpolation technique which is applied before shaping was changed from linear to PChip [26] to ensure a better approximation.

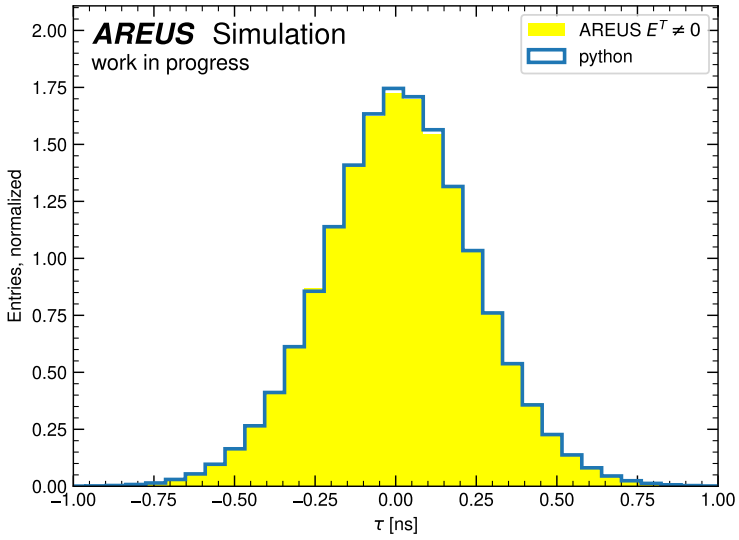

Figure 4.3: Distribution of the hit time in AREUS and the simulated hit times from a Python script. The times are distributed nearly identically which validates the AREUS simulation.

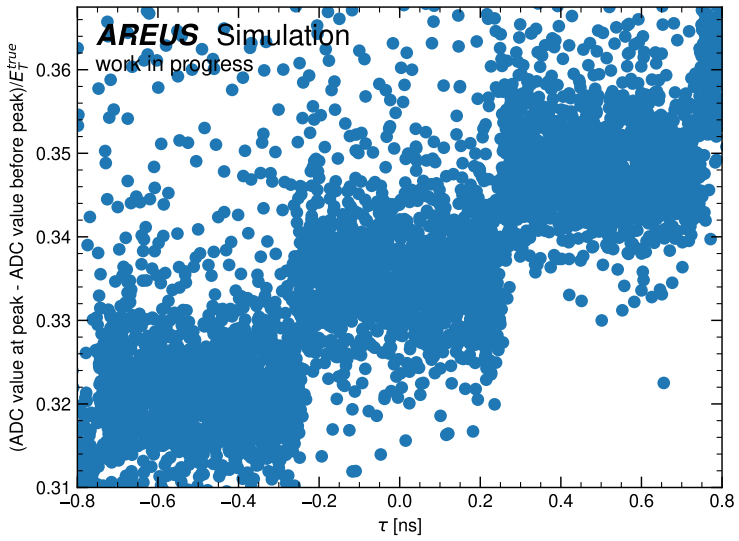

Figure 4.4: Difference between ADC value at peak and value before peak divided by the true energy over the hit time τ. Discrete steps of 0.5 ns can be seen which means that the pulses are not shifted properly because of a too small number of points on the pulse curve.

After changing these two resolution parameters, the pulse shapes and noise distribution of the generated samples changed. The deviation of the electronic noise could be caused by the Volt to MeV converter which depends on the ideal pulse shapes. The pulse shapes loaded by AREUS had their maximum not located exactly at a nominal bunch crossing time. Since the peaks of the pulses are not sampled then by the ADC, this leads to different pulse shapes with a relative amplitude smaller than 1. To solve this issue, the loaded pulse shapes are shifted so that their maximum is located at a bunch crossing. This solution leads to more consistent pulses, since the relative amplitude is 1 again at the sampled peak, but the exact shape is still different. These differences are caused by the different distances between two sampling points of the unshaped pulses because the shaping algorithm depends on this sample distance. Using more data points to describe the unshaped pulses results in a more realistic shaping. The pulse shapes of the previous data sets, those with an increased number of data points of the unshaped and unsampled pulses and the pulses corrected by shifts are shown in figure 4.5. Also the interpolation technique was changed from linear to PChip to ensure a better approximation. However, this can not be the reason for the differences of the shapes, because those also appear with the linear interpolation. Actually, the differences caused by better interpolation are relatively small and differences caused by the choice of the sampling distance dominate.
Also the possibility to simulate LLPs is not implemented yet. Unrealistic large time shifts can be simulated by using unnaturally high $\sigma_z > 20\,\text{cm}$ but this will also cause high negative time shifts that would not occur for LLPs. Since LLPs are hypothetical particles with unknown life times and production cross-section, there is no way to implement a realistic distribution of LLP hit times. It might be handy to implement another uniformly distributed hit time with an adjustable maximal τ. Another problem with these LLP time shifts can occur due to the periodicity of the bunch structure. There is no difference between a pulse with a hit time τ or $\tau + m \cdot 25\,\text{ns}, m \in \mathbb{Z}$. A LLP with a hit time $\tau_{\text{true}} = 23\,\text{ns}$ will likely be reconstructed with $\tau_{\text{pred}} = -2\,\text{ns}$. Reconstructing time shifts larger than $\pm 0.5\,\text{BC}$ is only reliably possible with advanced offline analysis techniques as shown in reference [14] for example.

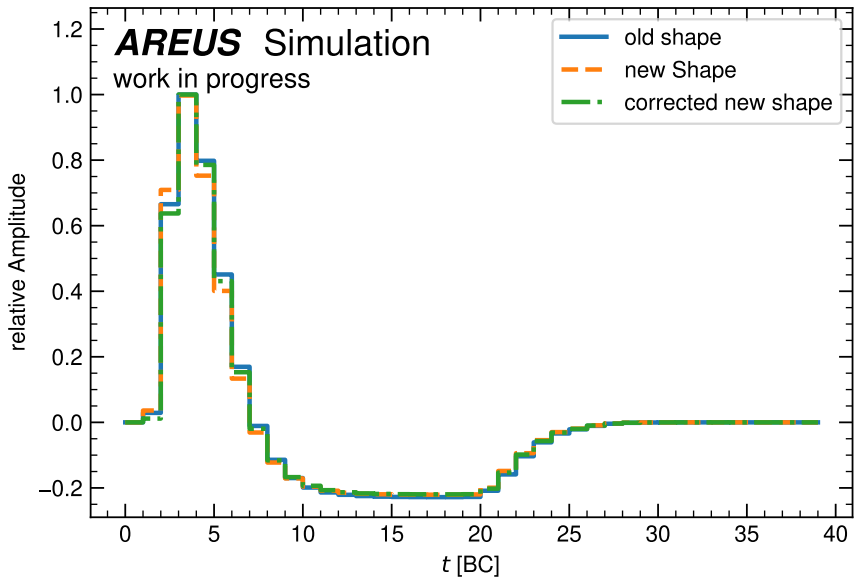

Figure 4.5: Sampled, ideal pulse shapes. The pulses of previous data sets as used in [27] are assumed to be correct. The new shape resulted from the increased number of data points of the unshaped and unsampled pulses. Since this shape has a relative amplitude smaller than 1 at the peak, a shift is performed before sampling to correct this effect. Also, the corrected shape differs from the original one because the number of data points of the pulse curve was increased, which influences the shaping algorithm.

4.3 Influence of Time Shifts to the Pulse Shape

The ADC will sample the signal exactly every 25 ns, synchronized to the bunch crossings. If the peak of a pulse is in time to the bunch crossing, the actual value at the peak is sampled. If the peak is shifted, the ADC samples a value in the neighborhood of the peak and the ADC output is therefore smaller than the actual energy. Figure 4.6 shows how the product of transverse energy E_T and hit time τ influences the difference between the peak value of the sampled pulse and the value before this peak depending on the pulses energy.
It can be seen that, if noise is neglected, the energy and the difference of the values define the product of transverse energy and hit time. This effect can be used to determine the hit time in algorithms like the OF_τ. The noise and pileup leads to data points which do not fit to the trend. To correct these, advanced filter techniques are needed.
It also shows that the hit time could affect the performance of the energy reconstruction since the OF and the ANNs use the values of the data points of a peak to reconstruct the energy. If the height of the sampled peak and the difference to the neighboring sampling points differ, the algorithms may have a significant performance decrease. This effect will be larger for high energetic pulses. For the OF_τ, in reference [6] a linear correction is suggested, which is also used in ATLAS offline reconstruction.

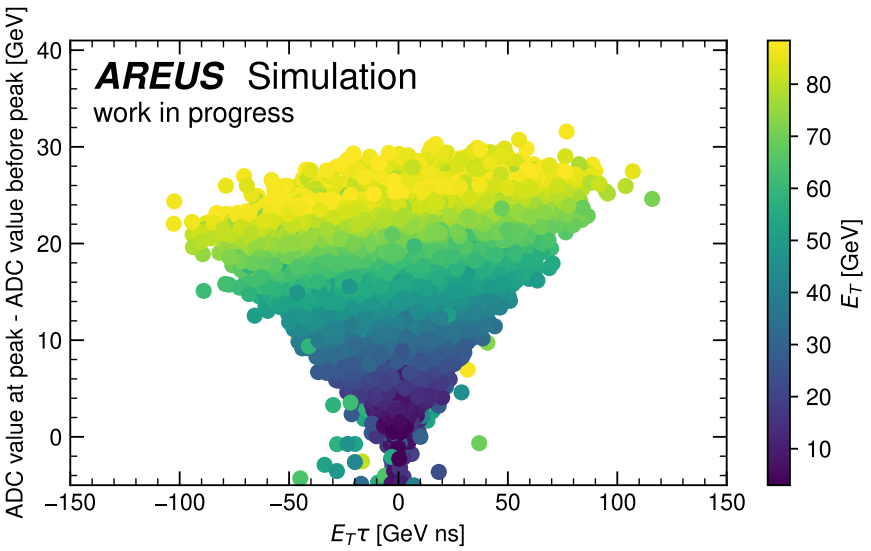

Figure 4.6: The difference between the value of the peak of the sampled pulse and the value before this peak depending on the product of transverse energy E_T and hit time τ on the x-axis and the transverse energy indicated by the color of the marker. Only hits with transverse energies above 3 GeV are included. The slopes in the color gradient indicate that the shifts have an noticeable influence on the pulse shape. This can influence the performance of the energy reconstruction but it could also be used to reconstruct the hit time.

4.4 The Influence of Time Shifts to CNNs and the Optimal Filter

To check how these time shifts influence the energy reconstruction algorithms, the CNNs and the OFMax were tested with two time shift distributions, one with realistic shifts as expected with $\sigma_z = 5\,\text{cm}$ and one with artificially enlarged hit times which are generated using $\sigma_z = 50\,\text{cm}$. These enlarged shifts are used to analyze additional effects as LLP shifts, even if they also include high negative shifts.

Analyzing the difference between the predicted and actual energy in figure 4.7, 4.8 and 4.9, it can be seen that the CNNs and the OF are influenced by the time shifts. The influence is relatively small for realistic time shifts and small energies while it is clearly visible for enlarged shifts and higher energies.

It is important to note, that the pulse shapes of the data differ from the previous data used to train the 3Conv and 4Conv CNN due to the increased number of points to describe the pulse shape. This causes performance decreases of the legacy CNNs which are not caused by the time shifts itself but the simulated data. Unfortunately these effects make it more difficult to compare the performance of the ANNs and the OF. A technical solution to prevent this has not yet been found at the time of this thesis.

Compared to the OF, the better performance of the CNNs for the 5 GeV random gap data set with realistic shifts is likely caused by the better handling of pileup. Especially for the 5 GeV random gap data set with enlarged shifts it is clearly visible that the CNNs struggle more with larger time shifts. The 30 GeV data sets with a constant gap show, that the CNNs also struggle for higher energies when the influence of time shifts increases.

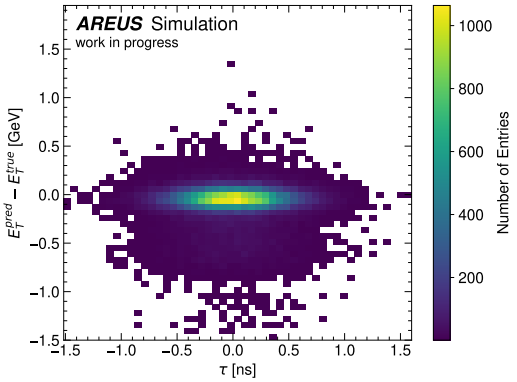

(a) OFMax. Data set contains hits with energies up to 5 GeV and realistic shifts. Gaps are normallly distributed with $\mu = 30$ BC and $\sigma = 10$ BC.

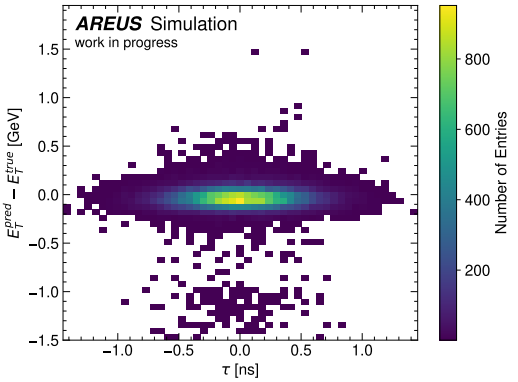

(b) OFMax. Data set contains hits with energies up to 30 GeV and realistic shifts. Gaps are constantly distanced 45 BC.

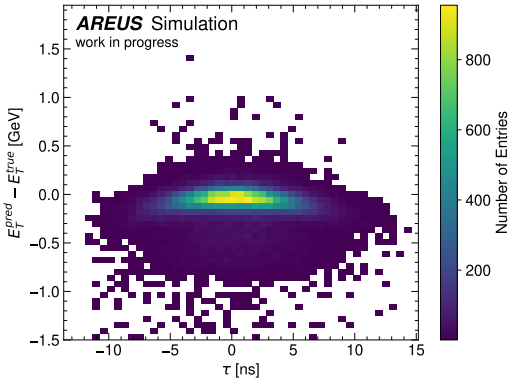

(c) OFMax. Data set contains hits with energies up to 5 GeV and enlarged shifts. Gaps are normallly distributed with $\mu = 30$ BC and $\sigma = 10$ BC.

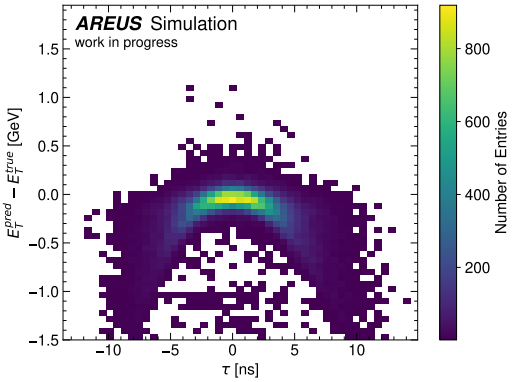

(d) OFMax. Data set contains hits with energies up to 30 GeV and enlarged shifts. Gaps are constantly distanced 45 BC.

Figure 4.7: 2D-Histogram of the difference between predicted and actual energies on the y-axis and the hit time on the x-axis for energies above 1 GeV for the OFMax. Different data sets were evaluated which show how the influence of time shifts depend on the energies of the pulses. Especially for large gaps and high energies the energy reconstruction of the OFMax is influenced negatively by the time shifts.

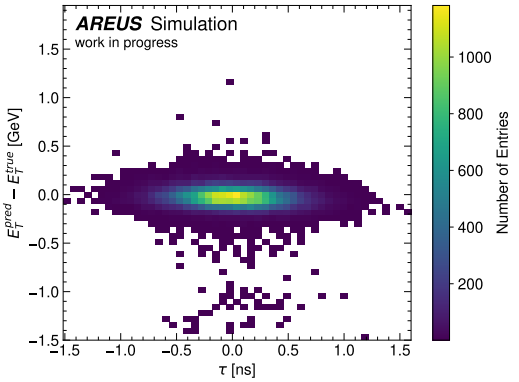

(a) 3Conv. Data set contains hits with energies up to 5 GeV and realistic shifts. Gaps are normallly distributed with $\mu = 30$ BC and $\sigma = 10$ BC.

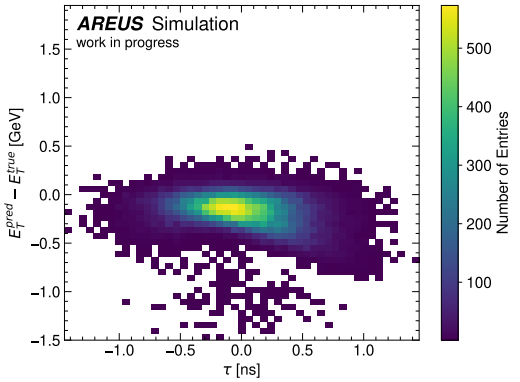

(b) 3Conv. Data set contains hits with energies up to 30 GeV and realistic shifts. Gaps are constantly distanced 45 BC.

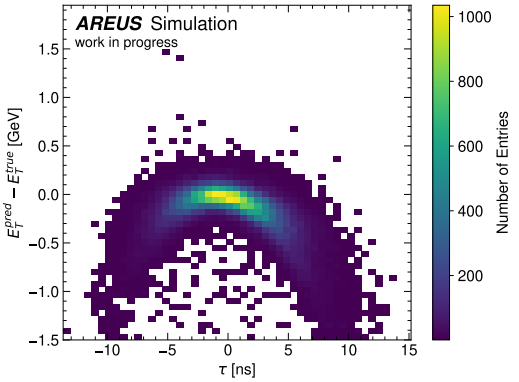

(c) 3Conv. Data set contains hits with energies up to 5 GeV and enlarged shifts. Gaps are normallly distributed with $\mu = 30$ BC and $\sigma = 10$ BC.

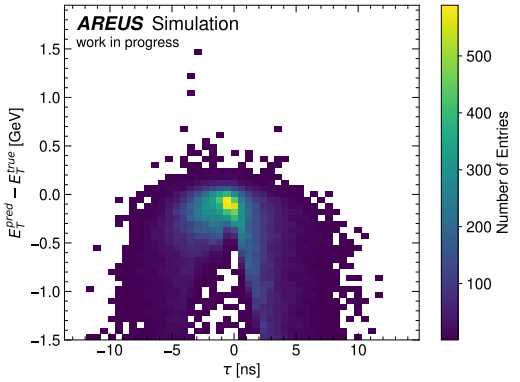

(d) 3Conv. Data set contains hits with energies up to 30 GeV and enlarged shifts. Gaps are constantly distanced 45 BC.

Figure 4.8: 2D-Histogram of the difference between predicted and actual energies on the y-axis and the hit time on the x-axis for energies above 1 GeV for the 3Conv. Different data sets were evaluated which show how the influence of time shifts depend on the energies of the pulses. Especially for large gaps and high energies the energy reconstruction of the 3Conv is influenced negatively by the time shifts. These effects are higher than for the OFMax.

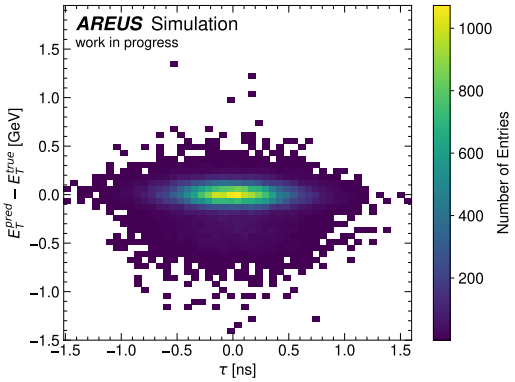

(a) 4Conv. Data set contains hits with energies up to 5 GeV and realistic shifts. Gaps are normallly distributed with $\mu = 30$ BC and $\sigma = 10$ BC.

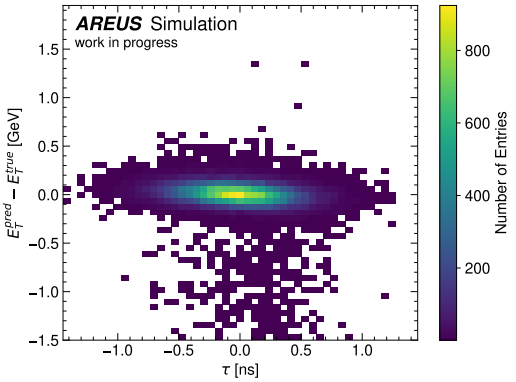

(b) 4Conv. Data set contains hits with energies up to 30 GeV and realistic shifts. Gaps are constantly distanced 45 BC.

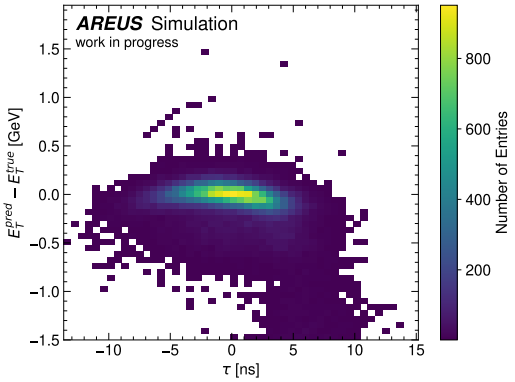

(c) 4Conv. Data set contains hits with energies up to 5 GeV and enlarged shifts. Gaps are normallly distributed with $\mu = 30$ BC and $\sigma = 10$ BC.

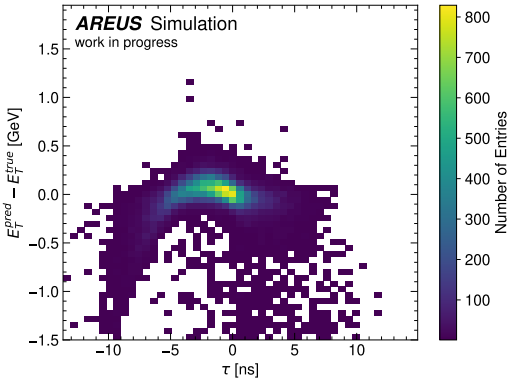

(d) 4Conv. Data set contains hits with energies up to 30 GeV and enlarged shifts. Gaps are constantly distanced 45 BC.

Figure 4.9: 2D-Histogram of the difference between predicted and actual energies on the y-axis and the hit time on the x-axis for energies above 1 GeV for the 4Conv. Different data sets were evaluated which show how the influence of time shifts depend on the energies of the pulses. Especially for large gaps and high energies the energy reconstruction of the 4Conv is influenced negatively by the time shifts. These effects are higher than for the OFMax.

Besides the influence of time shifts to the energy reconstruction quality, another effect, which should be checked, is the reconstruction of energies in wrong bunch crossings. Since the information of the energy deposit is used for the trigger system, it is important that the trigger starts the data readout for the correct bunch crossings. To check how often such effects occur, data points were evaluated, where:

$$\begin{aligned} & E_T^{\text{true}}(\text{BC}_i) < 0.1\,\text{GeV} \\ \wedge & \left(E_T^{\text{true}}(\text{BC}_{i+1}) > 0.5\,\text{GeV} \veebar E_T^{\text{true}}(\text{BC}_{i-1}) > 0.5\,\text{GeV}\right) \\ \wedge & E_T^{\text{pred}}(\text{BC}_i) > 0.5\,\text{GeV} \\ \wedge & \left(E_T^{\text{pred}}(\text{BC}_{i+1}) < 0.1\,\text{GeV} \veebar E_T^{\text{pred}}(\text{BC}_{i-1}) < 0.1\,\text{GeV}\right), \end{aligned} \tag{4.4}$$

where $\veebar$ is a symbol for *xor*. Figure 4.10 shows how the hit time influences the number of energy reconstructions assigned to the wrong bunch crossing. The frequencies are normalized to the number of total hit times in the corresponding bin.

The CNNs seem to assign less energy entries to a neighboring bunch crossing than the OF. In general the total number is quite small for the CNNs and the OF. Only 0.14 % of the data points were wrongly assigned by the OF, for the 4Conv 0.04 % and for the 3Conv 0.03 % of the energies were assigned to neighboring bunch crossings. For all energy reconstruction algorithms, the chance of assigning an energy to the wrong bunch crossing is higher for large positive or negative time shifts. For large time shifts with $|\tau| > 9\,\text{ns}$, no algorithm detected an energy in the wrong bunch crossing, which is likely caused by the small amount of data points with such a large shift.

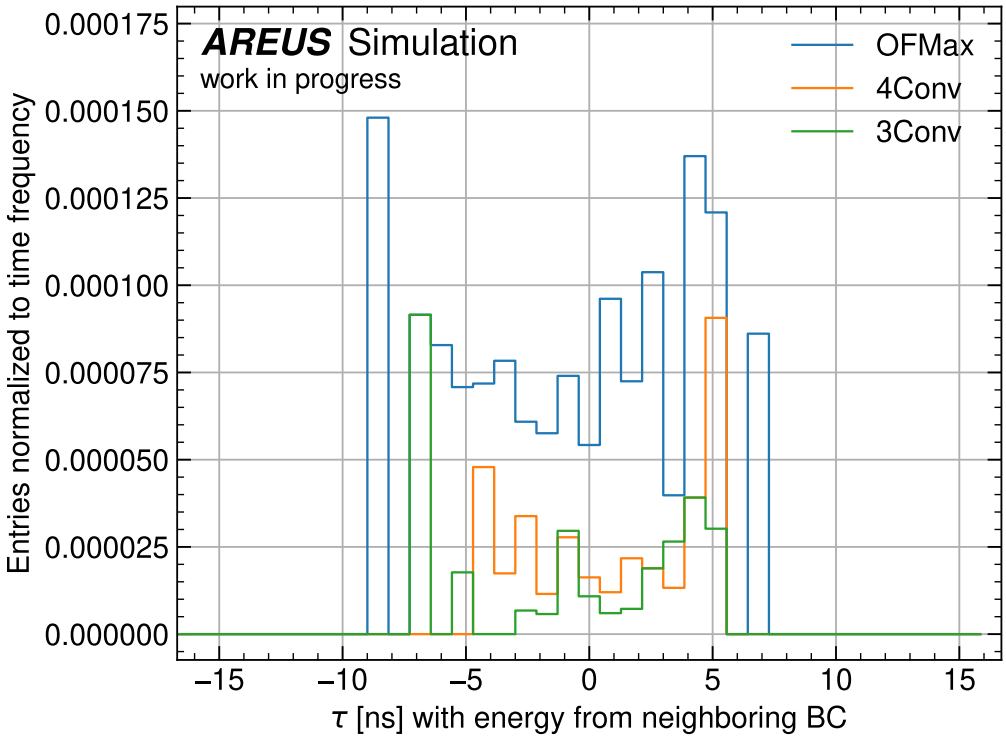

Figure 4.10: Histogram of energy reconstruction in wrongly assigned bunch crossings. The histogram contains data points which meet the condition 4.4 for a data set with energies up to 5 GeV, random gaps and enlarged time shifts. The OFMax produces more of these wrongly assigned energies than the CNNs. For all algorithms high time shifts increase the chance of assigning a energy deposit to the false bunch crossing.

4.5 Minimization of Performance decrease due to Time Shifts

To reduce the negative influence of time shifts on the energy reconstruction the first idea for a solution is to use data containing time shifts for the training of the network. Since the training data set described in section 3.4 led to very good results for the energy reconstruction, this data set is also used here to compare the 3Conv network without tagging to the OFMax and the 3Conv and 4Conv networks. Also, a 3Conv network with COReLU activation is analyzed at here which was trained on 1000 data sequences containing energies up to 5 GeV and 30 GeV and data without artificially inserted hits. The data with artificially inserted hits were used with realistic and artificially enlarged time shifts, the data set without these hits only contained realistic hit times.
In figure 4.11 and 4.12 the results for the 3Conv network without tagging and the 3Conv network with a COReLU function are shown. Both CNNs perform better than the legacy CNNs and the OFMax, which is especially visible for the data set with enlarged time shifts. Looking at the difference between predicted and true energy in the histogram in figure 4.13 one can see that both CNNs outperform the OF as well as the 3Conv and 4Conv networks which were not trained on data containing time shifts.
Looking at the energy deposits assigned to wrong bunch crossings in figure 4.14, it can be seen that both CNNs produce some more entries than the 3Conv but still fewer entries than the OFMax. For the 3Conv without Tagging 0.04 % and for the 3Conv with the COReLU activation 0.03 % of the energies were assigned to neighboring bunch crossings. All in all there are no big differences between the CNNs and the effects are small in general.

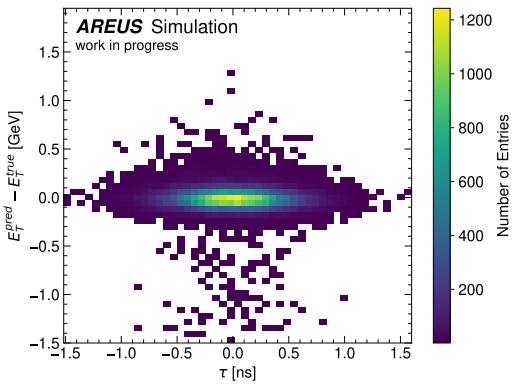

(a) 3Conv without Tagging layer. Data set contains hits with energies up to 5 GeV and realistic shifts. Gaps are normallly distributed with $\mu = 30$ BC and $\sigma = 10$ BC.

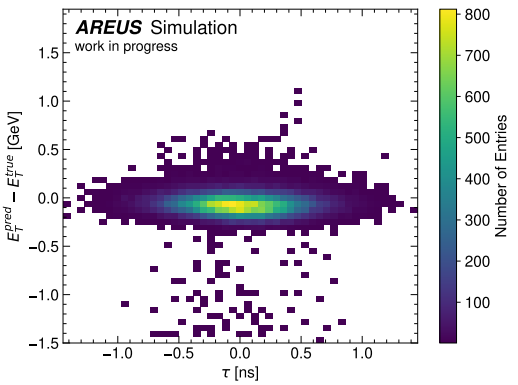

(b) 3Conv without Tagging layer. Data set contains hits with energies up to 30 GeV and realistic shifts. Gaps are constantly distanced 45 BC.

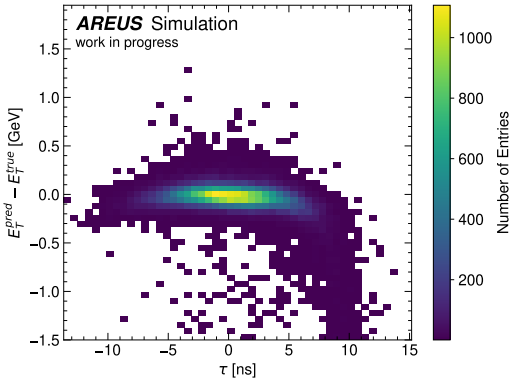

(c) 3Conv without Tagging layer. Data set contains hits with energies up to 5 GeV and enlarged shifts. Gaps are normallly distributed with $\mu = 30$ BC and $\sigma = 10$ BC.

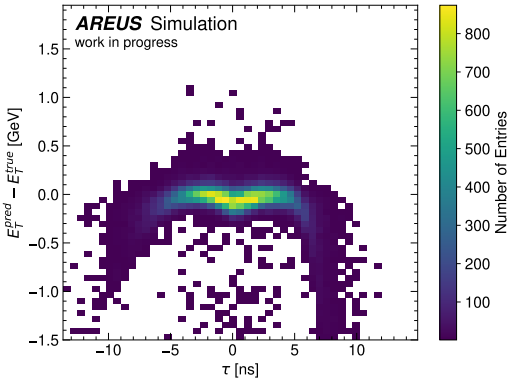

(d) 3Conv without Tagging layer. Data set contains hits with energies up to 30 GeV and enlarged shifts. Gaps are constantly distanced 45 BC.

Figure 4.11: 2D-Histogram of the difference between predicted and actual energies on the y-axis and the hit time on the x-axis for energies above 1 GeV for the 3Conv without Tagging. Different data sets were evaluated which show how the influence of time shifts depend on the energies of the pulses. The influence of time shifts is still cleary visible but there are less entries with high energy differences than for the OFMax.

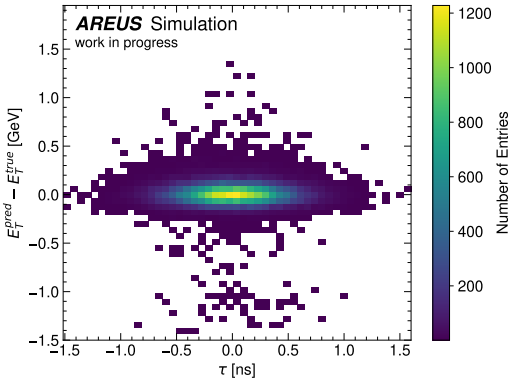

(a) 3Conv with COReLU. Data set contains hits with energies up to 5 GeV and realistic shifts. Gaps are normallly distributed with $\mu = 30$ BC and $\sigma = 10$ BC.

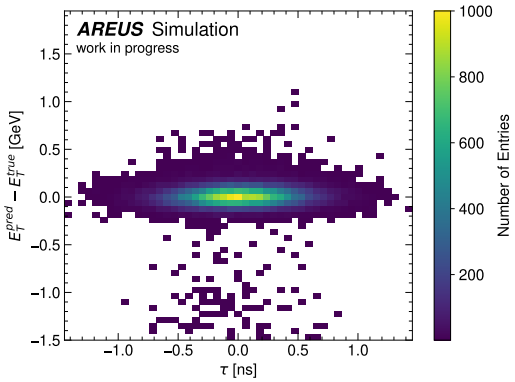

(b) 3Conv with COReLU. Data set contains hits with energies up to 30 GeV and realistic shifts. Gaps are constantly distanced 45 BC.

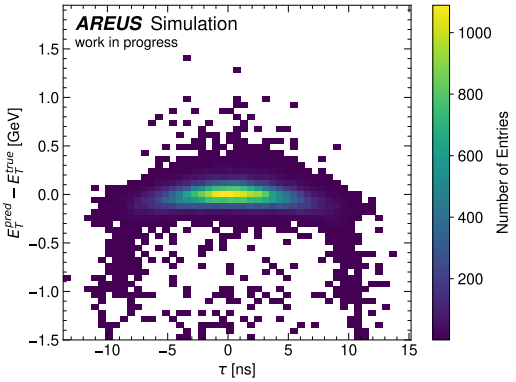

(c) 3Conv with COReLU. Data set contains hits with energies up to 5 GeV and enlarged shifts. Gaps are normallly distributed with $\mu = 30$ BC and $\sigma = 10$ BC.

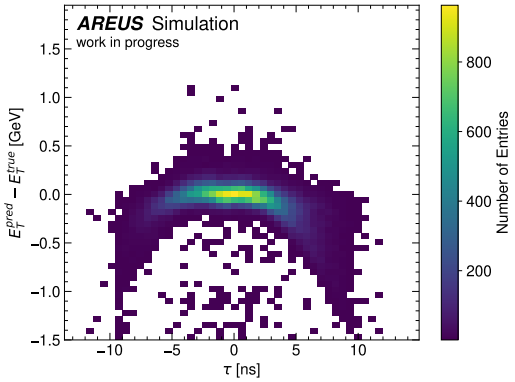

(d) 3Conv with COReLU. Data set contains hits with energies up to 30 GeV and enlarged shifts. Gap are constantly distanced 45 BC.

Figure 4.12: 2D-Histogram of the difference between predicted and actual energies on the y-axis and the hit time on the x-axis for energies above 1 GeV for the 3Conv with COReLU. Different data sets were evaluated which show how the influence of time shifts depend on the energies of the pulses. The influence of time shifts is still cleary visible but there are less entries with high energy differences than for the OFMax

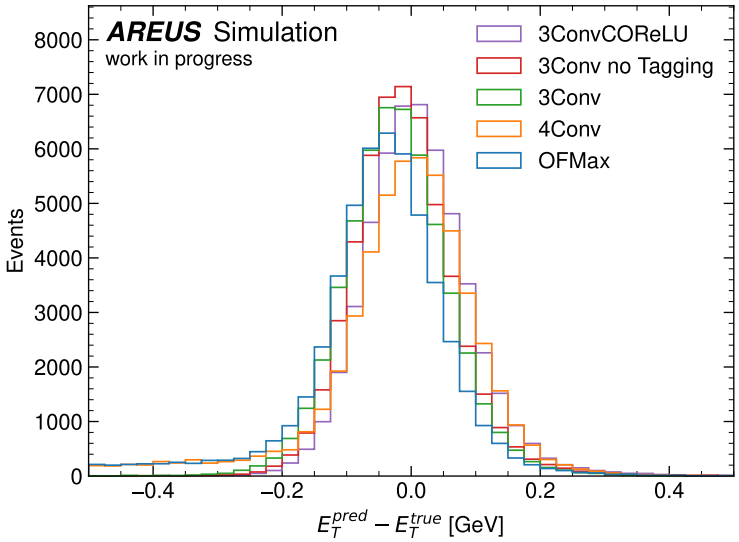

(a) Hits with energies up to 5 GeV. Realistic shifts. Gaps are normallly distributed with $\mu = 30$ BC and $\sigma = 10$ BC.

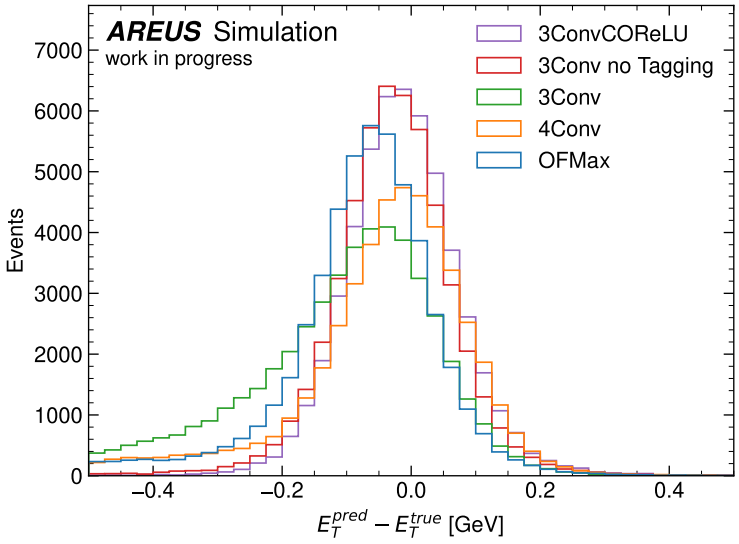

(b) Hits with energies up to 5 GeV. Enlarged shifts. Gaps are normallly distributed with $\mu = 30$ BC and $\sigma = 10$ BC.

Figure 4.13: Histograms of the difference between predicted and true energy for realistic and enlarged time shifts. The CNNs trained with data containing time shifts, the 3Conv not Tagging and 3ConvCOReLU, clearly outperform the other algorithms.

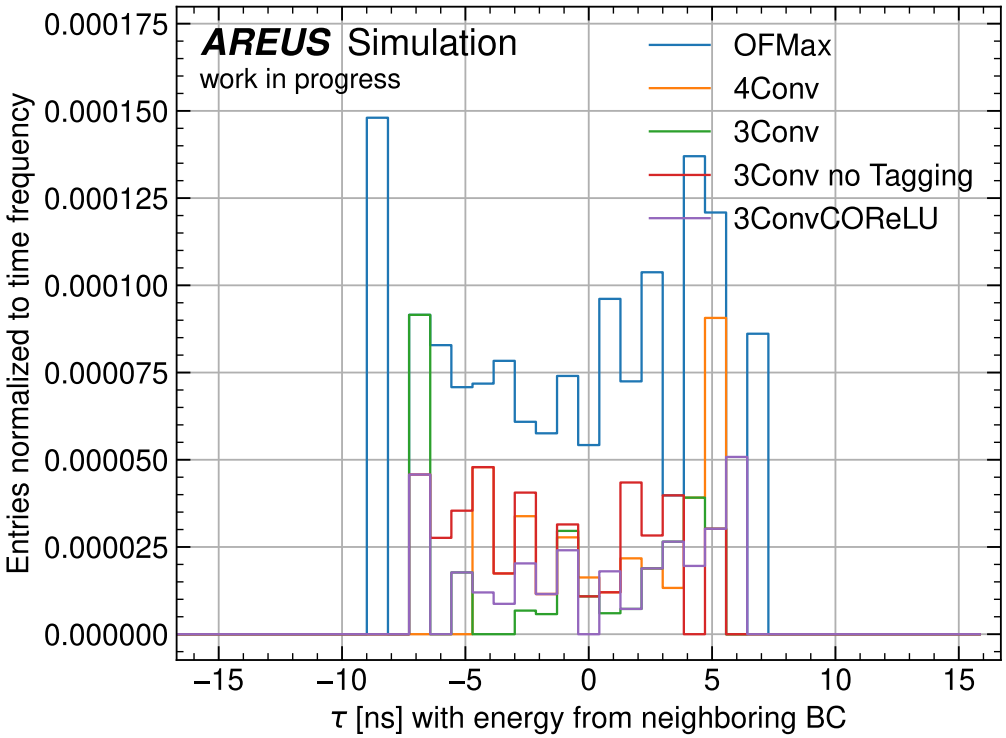

Figure 4.14: Histogram of energy reconstruction in wrongly assigned bunch crossings. The histogram contains data points which meet the condition 4.4 for a data set with energies up to 5 GeV, random gaps and enlarged time shifts. The CNNs trained with data containing time shifts produce more falsely assigned energy deposits.

4.6 Advanced Techniques to analyze Time Shifts

It may be desirable to not only reconstruct the energies but also reconstruct the product of energy and hit time as the OF_τ does. In perspective this could help with trigger decisions or it could be used to correct the energy reconstruction. Therefore different CNNs were tested and their $E\tau$ reconstruction performance was evaluated. It must be mentioned that in the current setup of LASP timing reconstruction shall be implemented but the trigger system is planned to not use the hit time information. The reconstruction of hit times should be as resource saving as possible.

The training used different data sets containing samples with realistic time shifts and artificially enlarged ones. The best results were found, when a data point only influences the loss, if the energy reconstruction network reconstructed and energy above 3 GeV at this bunch crossing. Different loss functions were tested briefly but more extensive studies should verify the ideal loss function. The loss function used here was the mean absolute error which gave good results in the tests. Since the performance of different trainings for the same CNN was mostly similar, they were not trained 100 times. Here, 10 trainings were executed.

Before results for the CNNs will be presented, some performance plots for the OF_τ are shown. The following plots contain data with hits up to 30 GeV for $\mu = 140$ and realistic or artificially enlarged time shifts. Only data points for which the transverse energy is greater than 3 GeV are included in the following plots. Since the CNNs presented in this section have been trained on the uncorrected data sets described in section 4.2, these data sets are also used here for evaluation. The evaluation could be repeated with the corrected data sets but this should not lead to much differing results.

In figure 4.15 it is clearly visible that the OF struggles with the reconstruction of hit times for small gaps between two pulses with high energy deposits. The performance decreases for distance up to 10 BC and between 15 BC and 25 BC. In these regions the previous pulse rises or falls. Since the difference between ADC values is an indicator for the hit time, a change of this difference influences the OF_τ more than the constant offset of the undershoot.

Figure 4.16 shows the difference between predicted and actual hit time for different energy ranges. Especially for the realistic hit times, the reconstruction works quite

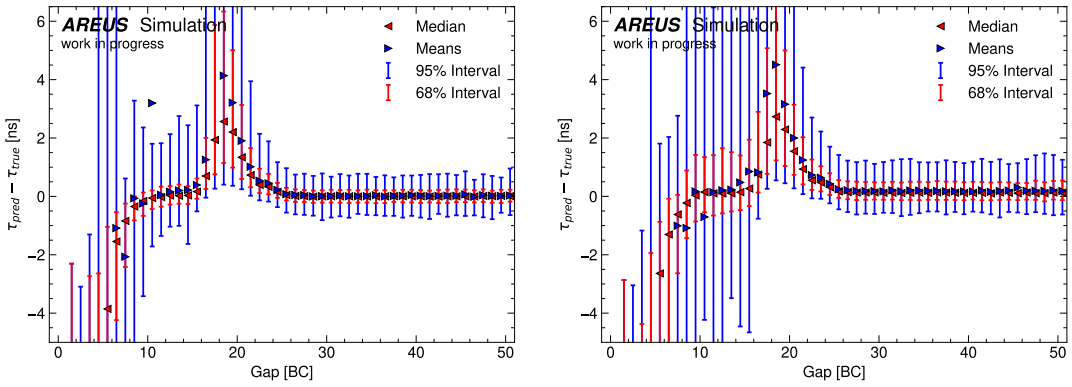

(a) realistic shifts **(b)** enlarged shifts

Figure 4.15: Plot of the mean and median of the difference between predicted and actual hit time as well as the ranges where 68 % and 95 % of the hit time differences are included depending of the gap between two pulses with energies above 3 GeV for the OF_τ. There are high performance decreases for gaps up to 10 BC and between 15 BC and 25 BC.

unreliable for transverse energies below about 10 GeV considering the hit times are mostly smaller than ± 1 ns.

Figure 4.17 shows the difference between predicted and actual hit time depending on τ_{true}. While for realistic hit times the reconstruction is not affected much for different τ ranges, for enlarged shifts the reconstruction performance decreases. The strong differences between median and mean values in the plot containing realistic data indicates that there must be very large or small outliers which affect the mean massively but they are not included in the 95 % ranges.

All in all the performance of the OF_τ is not very satisfying so it might be interesting to investigate if CNNs can perform better with limited resources.

The CNNs used to reconstruct the time were trained to reconstruct the product of energy and hit time. For the evaluation, this output is divided by the CNN energy reconstruction output. Since the CNNs will not reconstruct an energy in every bunch crossing, the time is set to 0 manually if the reconstructed energy is 0. The CNNs were constructed so that they do not affect the energy reconstruction because the main focus is still to reconstruct the energy as well as possible. Schemes of all presented CNNs are schon in figure 4.27

At first a minimal solution will be presented. The following CNN consist of 1 layer with a kernel size of 5 and 1 filter. The input is a concatenated data of the

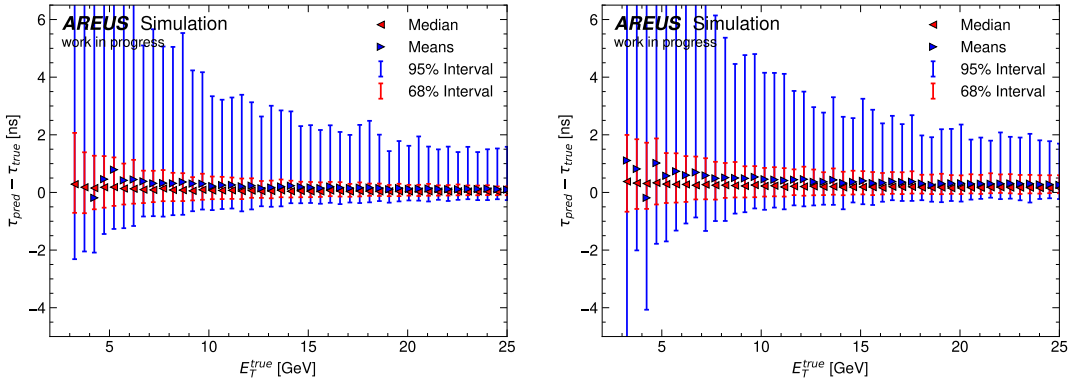

(a) realistic shifts **(b)** enlarged shifts

Figure 4.16: Plot of the mean and median of the difference between predicted and actual hit time as well as the ranges where 68 % and 95 % of the hit time differences are included depending of the transverse energy of the pulse for transverse energies above 3 GeV for the OF_τ.

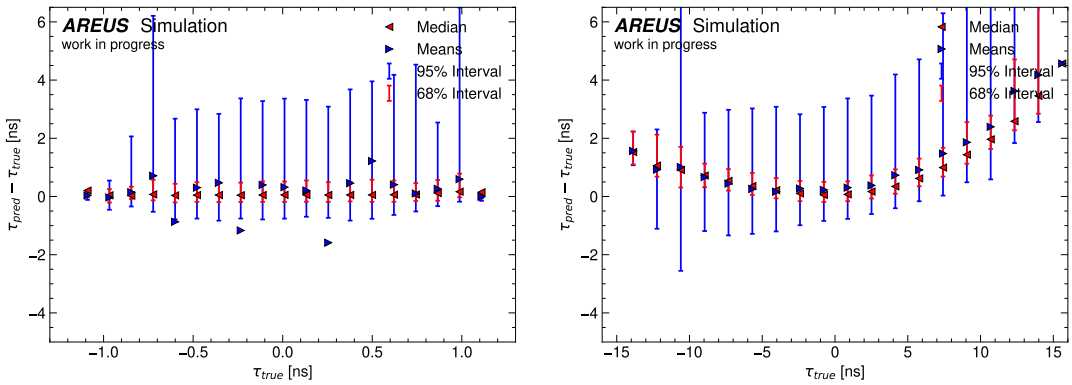

(a) realistic shifts **(b)** enlarged shifts

Figure 4.17: Plot of the mean and median of the difference between predicted and actual hit time as well as the ranges where 68 % and 95 % of the hit time differences are included depending of the true hit time of the pulse for transverse energies above 3 GeV for the OF_τ. There is a visible performance decrease for very large time shifts.

ADC output and the result of the energy reconstruction of the 3Conv network without tagging part from section 3.4. The knowledge of the already corrected energy should be an advantage over the OF_τ while adding only 11 parameters. A negative consequence is, that the energy reconstruction input causes a delay of the time output when implemented in FPGA.
Figure 4.18 again shows the difference between predicted and actual hit times depending on the gap between two pulses with transverse energies higher than 3 GeV. Compared to the OF_τ the 95 % and 68 % ranges got smaller in general and the large deviations between predicted and true hit times for gaps up to 10 BC and between 15 BC and 25 BC got smaller but they are still there.
In figure 4.19 it can be seen that the performance of this CNN is slightly better for all energy regions. Especially the 95 % intervals are smaller. Still the resolution of the time reconstruction is not satisfactory for $E_T^{\mathrm{true}} < 10\,\mathrm{GeV}$.
Figure 4.20 shows, that the time reconstruction for realistic hit times have fewer outliers since the median and mean are very close to each other in every bin. For the enlarged times the intervals again got smaller but the performance got worse for large negative and positive time shifts.
Because of the large deviations between predicted and true hit times for gaps between 15 BC and 25 BC in figure 4.18 a CNN with one layer with a kernel size of 25 is tested because then the pulses causing these deviations should be included in the receptive field of the CNN. This results in a CNN with 51 parameters. This CNN would consume potentially a lot of resources. But as figure 4.21 shows, this large receptive field actually leads to a really constant performance for different gaps.
Also, the time reconstruction resolution got much better for all observed energy ranges, which can be seen in figure 4.22. Again especially the 95 % ranges got reduced but also the 68 % ranges are visibly smaller.
Looking at the time differences depending on the hit time, the performance is much more constant for highly shifted pulses so this CNN outperforms the OF_τ and the smaller CNN even though for hits with $|\tau_{\mathrm{true}}| > 10\,\mathrm{ns}$ the differences are still very large.
To check whether the performance is increased only because of the larger kernel size or if the additional energy reconstruction input lead to the improved performance, another CNN was tested with a kernel size of 25. This CNN only has

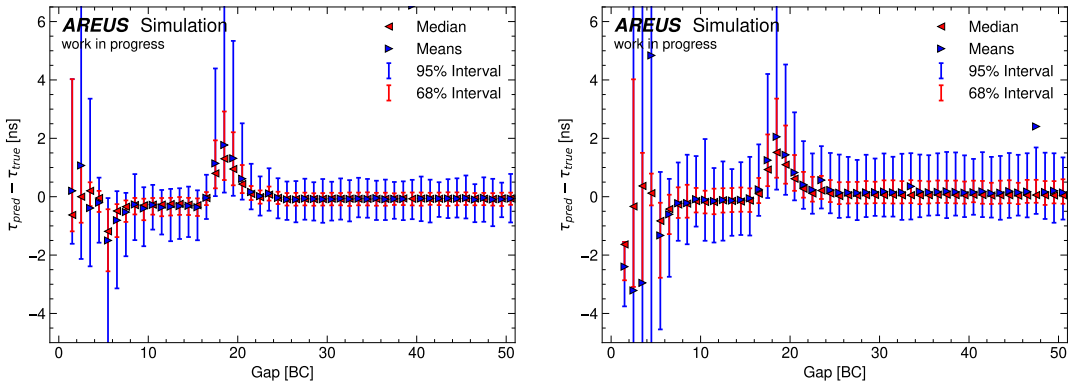

(a) realistic shifts **(b)** enlarged shifts

Figure 4.18: Plot of the mean and median of the difference between predicted and actual hit time as well as the ranges where 68 % and 95 % of the hit time differences are included depending of the gap between two pulses with energies above 3 GeV for 1-layer CNN with a kernel size of 5 and two inputs, the ADC and the energy reconstruction. There are still high performance decreases for gaps up to 10 BC and between 15 BC and 25 BC but these are smaller than for the OF_τ.

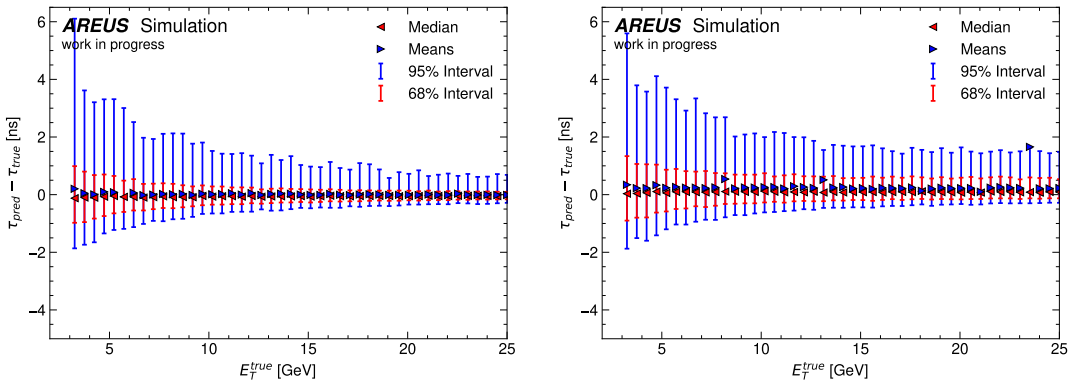

(a) realistic shifts **(b)** enlarged shifts

Figure 4.19: Plot of the mean and median of the difference between predicted and actual hit time as well as the ranges where 68 % and 95 % of the hit time differences are included depending of the transverse energy of the pulse for transverse energies above 3 GeV for 1-layer CNN with a kernel size of 5 and two inputs, the ADC and the energy reconstruction. Especially the upper ranges of the 95 % intervals got better than for the OF_τ.

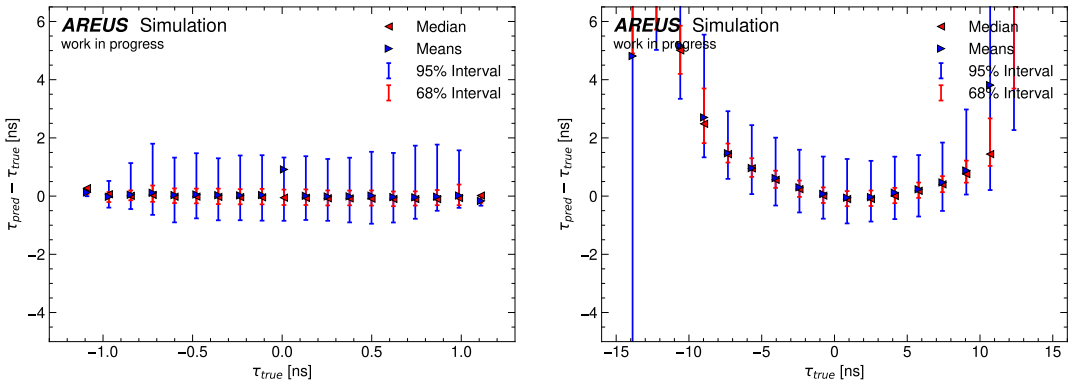

(a) realistic shifts **(b)** enlarged shifts

Figure 4.20: Plot of the mean and median of the difference between predicted and actual hit time as well as the ranges where 68 % and 95 % of the hit time differences are included depending of the true hit time of the pulse for transverse energies above 3 GeV for 1-layer CNN with a kernel size of 5 and two inputs, the ADC and the energy reconstruction. The performance for high time shifts decreased compared to the OF_τ.

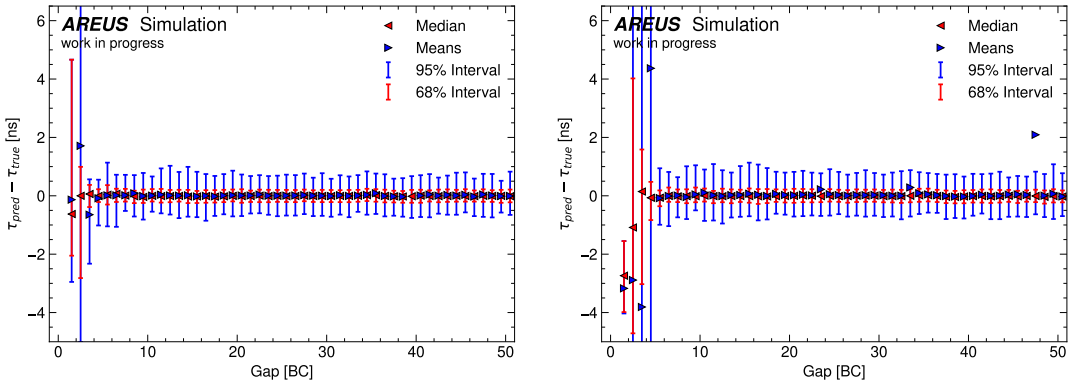

(a) realistic shifts **(b)** enlarged shifts

Figure 4.21: Plot of the mean and median of the difference between predicted and actual hit time as well as the ranges where 68 % and 95 % of the hit time differences are included depending of the gap between two pulses with energies above 3 GeV for 1-layer CNN with a kernel size of 25 and two inputs, the ADC and the energy reconstruction. There are no unwanted effects until gaps are smaller than 5 BC When both pulses overlay each other an the energy reconstruction output is probably heavily biased. This CNN clearly handles those short gaps better than the OF_τ.

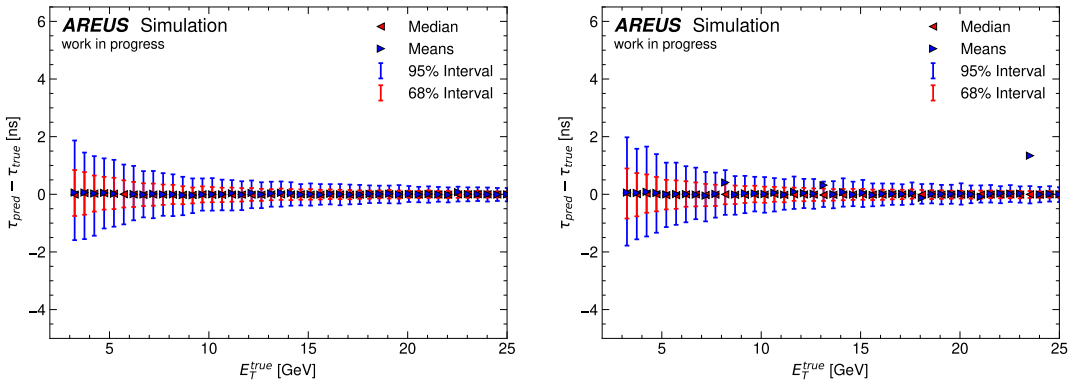

(a) realistic shifts **(b)** enlarged shifts

Figure 4.22: Plot of the mean and median of the difference between predicted and actual hit time as well as the ranges where 68 % and 95 % of the hit time differences are included depending of the transverse energy of the pulse for transverse energies above 3 GeV for 1-layer CNN with a kernel size of 25 and two inputs, the ADC samples and the reconstructed energies. The 95 % intervals are narrower than for the smaller CNN and the OF_τ.

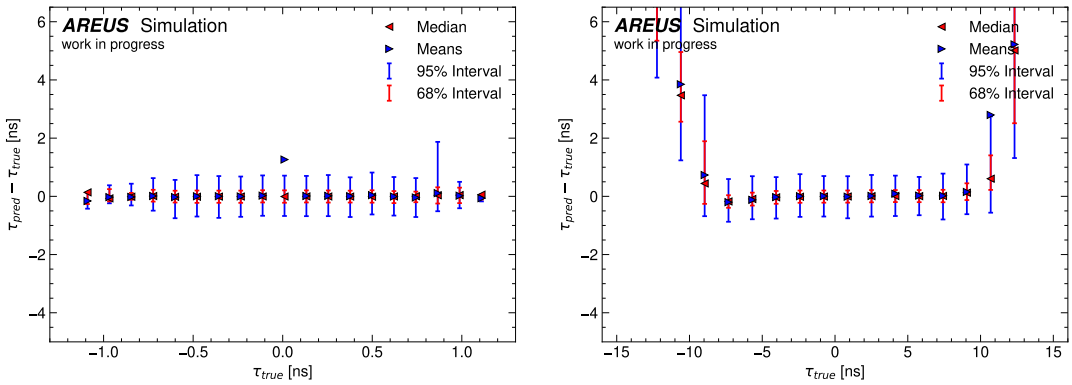

(a) realistic shifts **(b)** enlarged shifts

Figure 4.23: Plot of the mean and median of the difference between predicted and actual hit time as well as the ranges where 68 % and 95 % of the hit time differences are included depending of the true hit time of the pulse for transverse energies above 3 GeV for 1-layer CNN with a kernel size of 25 and two inputs, the ADC and the energy reconstruction. The difference between predicted and actual hit time is much more constant here compared to the smaller CNN and the OFMax.

the ADC as its input. Figure 4.24 shows, that this linear-filter-like CNN handles out-of-time pileup much better than the OF_τ with 5 weights and also better than the small CNN with an receptive field of 5 BC. Especially gaps up to 8 BC as well as gaps between 20 BC and 35 BC cause problems. The problems caused for higher gaps are interesting because the previous pulses should not influence the pulse shape for these distances. Since the temporal distance between two high pulses in this data set is gaussian distributed with $\mu = 30\,\text{BC}$ and $\sigma = 10\,\text{BC}$ this effect might be caused by these pulses with $E_T^{\text{true}} < 3\,\text{GeV}$.
Figure 4.25 shows that this CNN performs very similar to the larger CNN with a combined input. Visible deviations in terms of the time resolution can only be seen, when the plotted mean values in the figures with enlarged shifts are compared.
Also, figure 4.26 does not show any signs for real performance decreases compared to the larger CNN. Interestingly, this CNN is the only algorithm where the time differences over the actual hit time is not axial symmetrical.
All the CNNs outperformed the OF_τ. A large receptive field which includes the last 25 bunch crossings seem to be important for a constant performance. Whether the small performance increase, which is seen after adding the energy reconstruction output to this CNN's input, justifies 25 additional parameters, is a question of priorities.

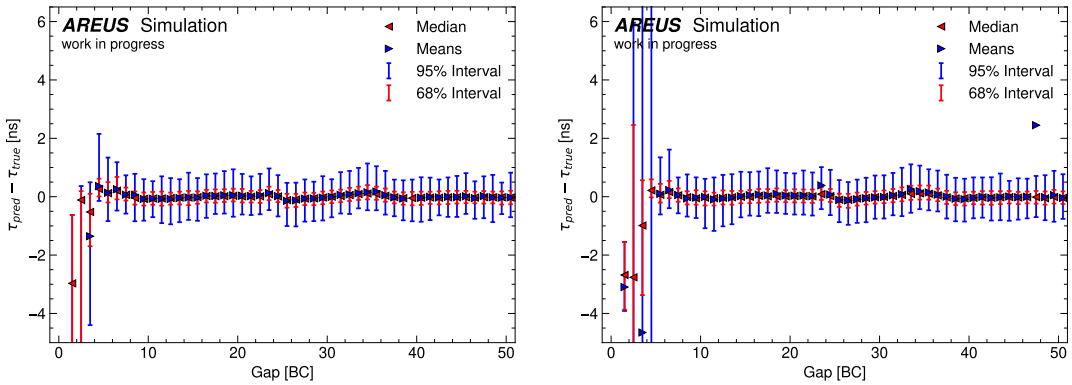

(a) realistic shifts **(b)** enlarged shifts

Figure 4.24: Plot of the mean and median of the difference between predicted and actual hit time as well as the ranges where 68 % and 95 % of the hit time differences are included depending of the gap between two pulses with energies above 3 GeV for 1-layer CNN with a kernel size of 25 and the ADC as input. There are are some unwanted effects so this CNN clearly handles those short gaps worse than the CNN with 51 parameters but still the deviations of the hit time reconstruction are much smaller than for the OF_τ.

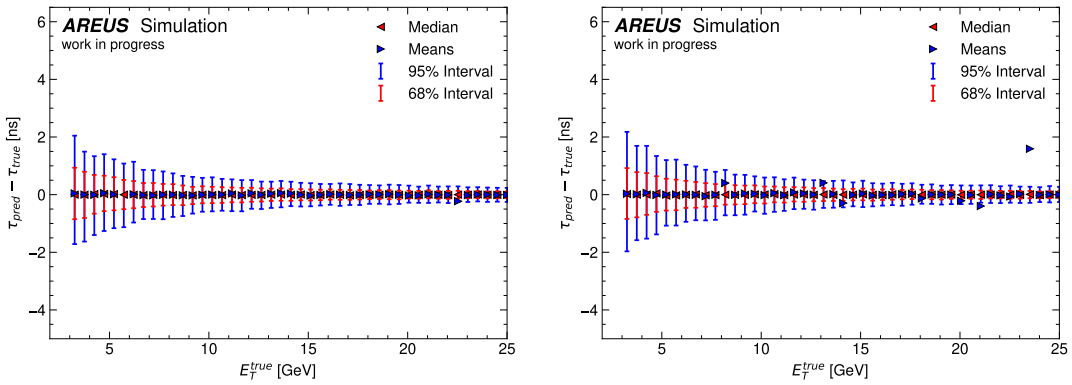

(a) realistic shifts **(b)** enlarged shifts

Figure 4.25: Plot of the mean and median of the difference between predicted and actual hit time as well as the ranges where 68 % and 95 % of the hit time differences are included depending of the transverse energy of the pulse for transverse energies above 3 GeV for 1-layer CNN with a kernel size of 25 and the ADC as input. The 95 % intervals are not visibly broader than for the CNN with 51 parameters.

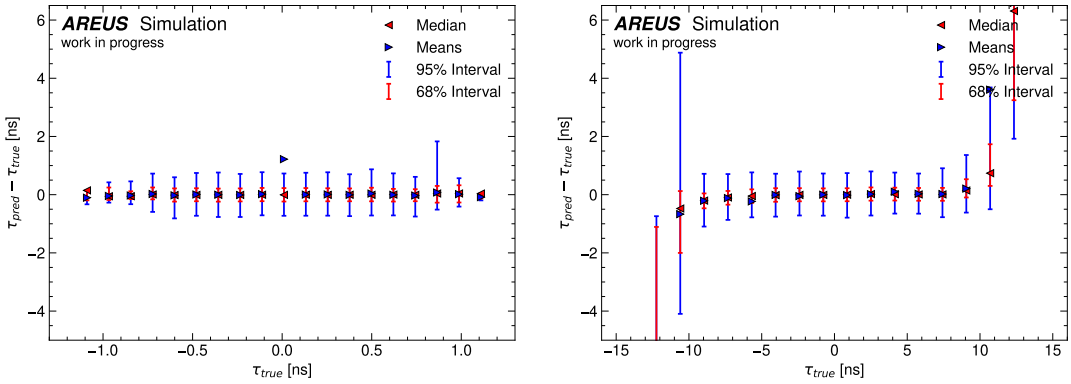

(a) realistic shifts **(b)** enlarged shifts

Figure 4.26: Plot of the mean and median of the difference between predicted and actual hit time as well as the ranges where 68 % and 95 % of the hit time differences are included depending of the true hit time of the pulse for transverse energies above 3 GeV for 1-layer CNN with a kernel size of 25 and the ADC as input. The difference between predicted and actual hit time is much more constant here compared to the smaller CNN and the OFMax. It is comparable constant to the large CNN but has a negative bias for large negative shifts.

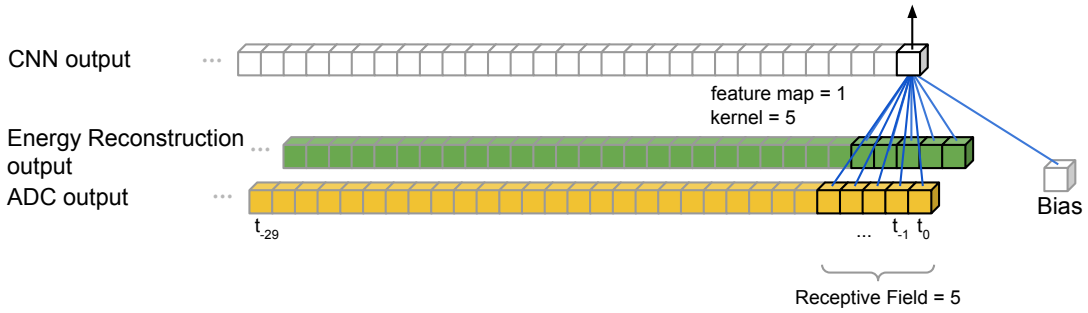

(a) 11-parameter time reconstruction CNN

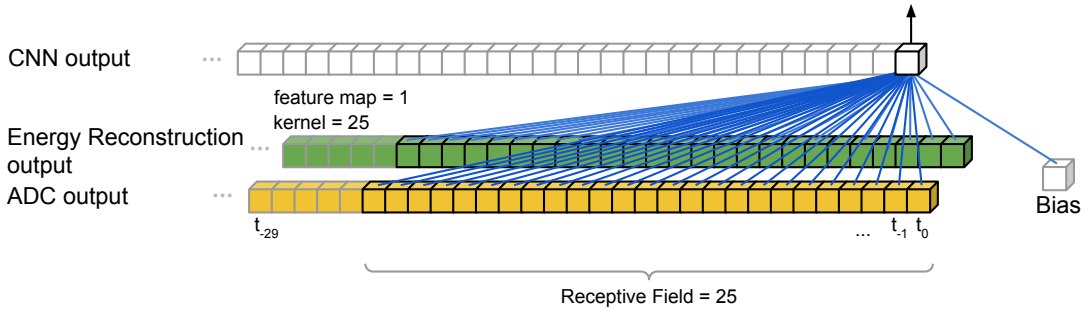

(b) 51-parameter time reconstruction CNN

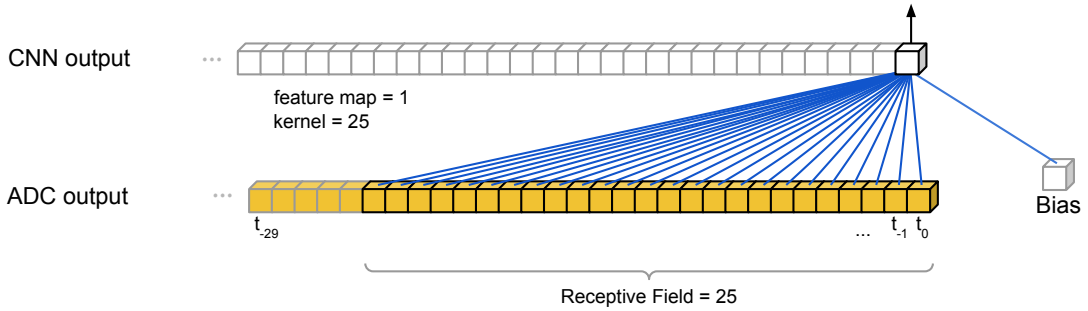

(c) 26-parameter time reconstruction CNN

Figure 4.27: Schemes of the presented CNNs for the reconstruction of the product of hit time and energy. All CNNs consist of 1 layer and have a linear activation. The smallest CNN with 11 parameters and the largest CNN with 51 parameters have 2 inputs: the ADC output and the energy reconstruction CNN output. The CNN with 26 parameters has only the ADC output as its input and therefore works like a linear filter.

5 Summary, Conclusions and Outlook

5.1 Summary and Conclusion

5.1.1 General Optimization

Different methods to solve some of the open problems of the CNNs for energy and time inference were investigated. Particulary interesting are those architectures and training methods which improve or maintain the performance and simultaneously decrease the resource consumption of the CNNs on FPGAs.
The simplification of the sigmoid function, namely the COReLU activation, is a promising way to reduce the resource consumption if the tagging subnetwork should be maintained. These CNNs reached similar performances as the legacy CNNs with sigmoid functions. No significant disadvantage was noticeable.
If CNNs without tagging layers perform at least as well as those CNNs with a tagging subnetwork, the tagging structure should get discarded to reduce the resource consumption. In section 3.4, a method to train such a CNN was described. The network, which was presented, consists of three convolutional layers with ReLU activation functions. While the energy resolution of the 3Conv network without tagging was better than for all other energy reconstruction algorithms, this network reconstructed more fake energy than the OFMax and the 3Conv network with tagging. The reproducibility of well performing trainings of the 3Conv network without tagging was better than for the legacy architecture, when it was trained with the same data sets and training method, which allowed to train CNNs without tagging layers. Ways to improve the signal detection and background rejection should be further investigated.
Also advanced loss functions were tested. The hyperbolic-tangent-linear loss in-

creased the performance of the 3Conv CNN with a COReLU activation but not for the normal 3Conv network. This effect was observed for two different training setups. It might be interesting to study further how architectures and loss functions affect each other.

5.1.2 The Influence of Time Shifts

To test the influence of shifted pulses caused by the variation of hit times, an additional function was implemented in AREUS. Some simplifications were used but the implementation produces time shifts in a realistic order of magnitude. For a better data quality, the number of data points describing the unshaped and unsampled pulse curves were changed. This lead to variation in the ideal pulse shapes compared to previously used data. These variation do not mean, that the newly produced samples are more unrealistic, but it makes it harder to analyze the performance of legacy CNNs using data with time shifts. It is necessary to ensure that the simulated data and especially the pulse shapes are actually realistic.
Time shifts influence the performance of CNNs and the OFMax. While for realistic pulse shifts, these effects are relatively small but noticeable, for enlarged hit times they are not tolerable. These effects can be handled unproblematically by including different hit times in the training data. Also using enlarged hits for the training might be good if non-regular signals, like from LLP paritcles, occur. Especially the 3Conv network without tagging layer handled time shifts really well and outperformed the CNNs from [27] and the OFMax. The ratio of realistic shifts and artificially enlarged shifts in the training data should be optimized. So, the performance of the CNNs can be optimized for a realistic scenario while still performing well on edge cases.

5.1.3 The Reconstruction of Time Shifts

Not only the performance of the OF but also of the OF_τ will be decreased with high luminosity and especially for increased out-of-time pileup. The time reconstruction of the OF_τ and the CNNs is not very reliable for small energies. Because of that, only hits with $E_T^{\mathrm{true}} > 3\,\mathrm{GeV}$ are evaluated here. Also for transverse energies up to 10 GeV the reconstruction is not very reliable and the relative errors

are large for many hits.
A reliable reconstruction of the hit time seems to need quite a lot of parameters. While small CNNs with 11 parameters can already outperform the OF_τ, 30, 50 or more parameters are needed to reach results which are not strongly influenced by the temporal distance to the previous pulse.
It must be decided by physics simulations if this additional consumption of resources is worth it. The output of the timing analysis could be used to indicate energy reconstructions asserted to false bunch crossings. While these are an actual problem for the trigger, they are quite rare and the influence of such an additional criterion must be checked in detail very carefully.

5.2 Outlook

The new CNN architectures should be tested on FPGAs to check their performance in a more realistic environment. Even if there are no indications that the COReLU activation and CNNs without tagging part are affected more by the hardware implementation than the legacy CNNs, it is necessary to check the influence of the hardware implementation. Also in theory these architectures should save resources but the exact effects are not completely known yet.
The training of the 3Conv network without tagging layer and the specialization of the 3Conv and 4Conv networks showed how important the choice of the properties of the training data sets is. The training data used for the 3Conv network without tagging part was chosen more or less randomly. A more reasoned choice of the frequency of specific properties might help to perform optimally on realistic data sets while still working well for edge cases.
Also the simulated data from AREUS should be further checked to verify if the pulse shapes and noise pattern is actually close to the actual pulses at the LAr calorimeter. Even if training methods are found to achieve a good robustness of the CNNs against shape fluctuation, this is very important to check.
The influence of time shifts shows that the training data should contain a broad variety of effects which occur at the real ADC output. Other influencing variations like the bunch train structure should all be contained in the training data to check if further variations of the ADC output is an additional problem for the CNNs.

Also higher energies than 30 GeV should be further studied. Especially for high energies the influence of shifted pulses will increase because the ADC value at the peak of a pulse becomes linearly smaller in absolute terms for higher energies. The reliable reconstruction of energies in a large range between 0.01 GeV to 1000 GeV will be an additional challenge.
Since the trigger system of ATLAS uses the information of multiple detector cells, it is interesting to check how the reconstruction of fake energies for example influences the trigger. Therefore the CNNs should be implemented in a simulation of the whole ATLAS detector. For this simulation, the CNNs should be further analyzed in different detector regions.

6 Bibliography

[1] High Luminosity LHC ls3 schedule change. https://hilumilhc.web.cern.ch/article/ls3-schedule-change. Accessed: August 04 2022.

[2] Keras documentation. https://keras.io/api/.

[3] Tensorflow documentation. https://www.tensorflow.org/api_docs/python/tf.

[4] P.A. Bromiley. Products and Convolutions of Gaussian Probability Density Functions. *Tina Memo No. 2003-003 Internal Report*, Aug 14 2014.

[5] C.J. Willmott et al. Statistics for the Evaluation and Comparison of Models. *Journal of Geophysical Research, VOL. 90, NO. C5*, pages 8995–9005, Sep 20 1985. doi:10.1029/JC090iC05p08995.

[6] W.E. Cleland and E.G. Stern. Signal processing considerations for liquid ionization calorimeters in a high rate environment. *Nuclear Instruments and Methods in Physics Research Section A: Accelerators, Spectrometers, Detectors and Associated Equipment*, 338(2):467–497, 1994. URL: https://www.sciencedirect.com/science/article/pii/0168900294913323, doi:https://doi.org/10.1016/0168-9002(94)91332-3.

[7] The ALICE Collaboration. *ALICE: Technical proposal for a Large Ion collider Experiment at the CERN LHC*. LHC technical proposal. CERN, Geneva, 1995. URL: https://cds.cern.ch/record/293391.

[8] The ATLAS Collaboration. *ATLAS liquid-argon calorimeter: Technical Design Report*. Technical design report. ATLAS. CERN, Geneva, 1996. URL: https://cds.cern.ch/record/331061, doi:10.17181/CERN.FWRW.FOOQ.

[9] The ATLAS Collaboration. The ATLAS experiment at the CERN large hadron collider. *JINST*, 3(08):S08003–S08003, Aug 2008. doi:10.1088/1748-0221/3/08/s08003.

[10] The ATLAS Collaboration. Observation of a new particle in the search for the standard model higgs boson with the ATLAS detector at the LHC. *Physics Letters B*, 716(1):1–29, sep 2012. URL: https://doi.org/10.1016%2Fj.physletb.2012.08.020, doi:10.1016/j.physletb.2012.08.020.

[11] The ATLAS Collaboration. ATLAS Liquid Argon Calorimeter Phase-I Upgrade: Technical Design Report. Sep 2013. CERN-LHCC-2013-017, ATLAS-TDR-022. URL: https://cds.cern.ch/record/1602230.

[12] The ATLAS Collaboration. ATLAS Liquid Argon Calorimeter Phase-II Upgrade: Technical Design Report. Sep 2017. CERN-LHCC-2017-018, ATLAS-TDR-027. URL: https://cds.cern.ch/record/2285582, doi:10.17181/CERN.6QIO.YGHO.

[13] The ATLAS Collaboration. Atlas data quality operations and performance for 2015–2018 data-taking. *JINST*, 15(04):P04003–P04003, Apr 2020. doi:10.1088/1748-0221/15/04/p04003.

[14] The ATLAS Collaboration. Search for neutral long-lived particles in *pp* collisions at $\sqrt{s} = 13$ TeV that decay into displaced hadronic jets in the ATLAS calorimeter. *JHEP*, 2206:005. 47 p, Mar 2022. URL: https://cds.cern.ch/record/2802865, arXiv:2203.01009, doi:10.1007/JHEP06(2022)005.

[15] The LHCb Collaboration. LHCb reoptimized detector design and performance: Technical Design Report. Technical report, CERN, Geneva, 2003. URL: http://cds.cern.ch/record/630827.

[16] W. N. Cottingham and D. A. Greenwood. *An Introduction to the Standard Model of Particle Physics*. Cambridge University Press, 2 edition, 2007. doi:10.1017/CBO9780511791406.

[17] Communications Education and Outreach Group. *LHC FAQ the guide*. CERN-Brochure-2017-002-Engs. CERN, Geneva, February 2017. URL: https://cds.cern.ch/record/2255762.

[18] Abdel-Hamid et al. Exploring convolutional neural network structures and optimization techniques for speech recognition. *Proc. Interspeech 2013*, pages 3366–3370, Aug 2013. doi:10.21437/Interspeech.2013-744.

[19] Chigozie Nwankpa et al. Activation functions: Comparison of trends in practice and research for deep learning., Nov 8 2018. URL: https://arxiv.org/abs/1811.03378, doi:10.48550/ARXIV.1811.03378.

[20] Kaiming He et al. Delving deep into rectifiers: Surpassing human-level performance on imagenet classification, 2015. URL: https://arxiv.org/abs/1502.01852, doi:10.48550/ARXIV.1502.01852.

[21] M. Della Negra et al. CMS: letter of intent by the CMS Collaboration for a general purpose detector at LHC. Technical report, CERN, Geneva, 1992. Open presentation to the LHCC 5 November 1992, M. Della Negra/CERN, CMS Spokesman. URL: https://cds.cern.ch/record/290808.

[22] O. Aberle et al. *High-Luminosity Large Hadron Collider (HL-LHC): Technical design report*. CERN Yellow Reports: Monographs. CERN, Geneva, 2020. URL: https://cds.cern.ch/record/2749422, doi:10.23731/CYRM-2020-0010.

[23] Y. LeCun et al. Handwritten digit recognition with a back-propagation network. In *Advances in Neural Information Processing Systems*, volume 2. Morgan-Kaufmann, 1989. AT&T Bell Laboratories, Holmdel, N. J. 0773. URL: https://proceedings.neurips.cc/paper/1989/file/53c3bce66e43be4f209556518c2fcb54-Paper.pdf.

[24] Lyndon Evans and Philip Bryant. *LHC Machine*, volume 3. IOP Publishing, Aug 2008. doi:10.1088/1748-0221/3/08/s08001.

[25] Tom Fawcett. Roc graphs: Notes and practical considerations for researchers. *Machine learning*, 31(1):1–38, 2004.

[26] F. N. Fritsch and R. E. Carlson. Monotone piecewise cubic interpolation. *SIAM Journal on Numerical Analysis*, 17(2):238–246, 1980. doi:10.1137/0717021.

[27] G. Aad, AS. Berthold, T. Calvet et al. Artificial Neural Networks on FPGAs for Real-Time Energy Reconstruction of the ATLAS LAr Calorimeters. *Computing and Software for Big Science*, 5:19, 2 October 2021. doi:10.1007/s41781-021-00066-y.

[28] Particle Data Group. Review of Particle Physics. *Progress of Theoretical and Experimental Physics*, 2022:083C01, Aug 8 2022. doi:10.1093/ptep/ptac097.

[29] Peter J. Huber. Robust Estimation of a Location Parameter. *The Annals of Mathematical Statistics*, 35(1):73 – 101, 1964. doi:10.1214/aoms/1177703732.

[30] A. Courville I. Goodfellow, Y. Bengio. *Deep Learning*. The MIT Press, Nov 18 2016. ISBN: 9780262035613.

[31] Kunihiko Fukushima. Cognitron: A Self-organizing Multilayered Neural Network. *Biol. Cybernetics, Springer*, 20:121–136, 1975. doi:10.1007/BF00342633.

[32] Nico Madysa. AREUS: A Software Framework for ATLAS Readout Electronics Upgrade Simulation. *EPJ Web Conf.*, 214:02006, 2019. doi:10.1051/epjconf/201921402006.

[33] Esma Mobs. The CERN accelerator complex - 2019. Complexe des accélérateurs du CERN - 2019. Jul 2019. General Photo. URL: https://cds.cern.ch/record/2684277.

[34] Joao Pequenao. Computer generated image of the whole ATLAS detector. 2008. URL: https://cds.cern.ch/record/1095924.

[35] Iva Raynova and Iva Maksimova Raynova. First tests of crab cavities promise a luminous future. Mar 2017. URL: http://cds.cern.ch/record/2257842.

[36] Burkhard Schmidt. The high-luminosity upgrade of the LHC: Physics and technology challenges for the accelerator and the experiments. *Journal of Physics: Conference Series*, 706:022002, apr 2016. doi:10.1088/1742-6596/706/2/022002.

[37] Martin S. Won. Intel® agilex™ fpgas deliver a game-changing combination of flexibility and agility for the data-centric world, intel® agilex™ fpga architecture white paper. https://www.intel.de/content/www/de/de/products/docs/programmable/agilex-data-centric-wp.html. Accessed: August 11 2022.

[38] X. Vidal et al. Beyond the Standard Model Physics at the HL-LHC and HE-LHC, 2018. URL: https://arxiv.org/abs/1812.07831, doi:{10.48550/ARXIV.1812.07831}.

Acknowledgements

I want to thank my supervisor Prof. Arno Straessner for giving me the chance to work on this fascinating topic in the context of an international scientific research group allowing me to gather experience in physics research. I am extremely grateful for the opportunities I got.
Also I want to thank the whole detector development working group at the IKTP for all the discussion, support and help I got in the year of working together. Special thanks go to Anne-Sophie Berthold, Nick Fritzsche, Rainer Hentges, Max Maerker, Johann Voigt and Philipp Welle who were always ready to answer me questions. But also Andreas Glatte and Wolfgang Mader were very supportive, especially for technical issues.
Last but not least I also want to thank my parents, my brother and my girlfriend for supporting me over the last years. The whole studies would have been much more challenging without the emotional and personal support I got from them.

Erklärung

Hiermit erkläre ich, dass ich diese Arbeit im Rahmen der Betreuung am Institut für Kern- und Teilchenphysik ohne unzulässige Hilfe Dritter verfasst und alle Quellen als solche gekennzeichnet habe.

Christian Gutsche
Dresden, Oktober 2022